Design and Calibration of the DUNE Liquid Argon Near Detector

by

Daniel Douglas

A dissertation submitted in partial fulfillment
of the requirements for the degree of
Doctor of Philosophy
(Physics)
in Michigan State University
2022

Doctoral Committee:

Professor Kendall Mahn, Chair
Professor Tyce DeYoung
Professor Wade Fisher
Professor Scott Pratt
Professor Laura Chomiuk

ACKNOWLEDGEMENTS

> ...Everywhere life is full of heroism. Be yourself. Especially do not feign affection. Neither be cynical about love; for in the face of all aridity and disenchantment, it is as perennial as the grass.
>
> Max Ehrman, *Desiderata*

With great thanks to all of the people I love and who have loved me. All that I may accomplish in my life is in equal share yours.

Especially, thank you to my family, who have always expressed a confidence in me that I have struggled to find in myself. To my parents, who have pushed me to challenge myself and allowed to me to pursue the things that interest me. You have helped me to see the value in hard work and the beauty and peace in rest, and fostered in me an inquisitiveness that has been a gift in everything I do.

To my grandparents, who have given me the foundational love of wisdom and care. Pop, who taught me awe at each launch of a rocket into the unknown. Grandma, who constantly reminds me that wonder is the basis of curiosity.

To the friends I have made inside and outside of the physics world. The friends and colleagues with whom I've shared an office – Mike, Erica, Luke, Jake, Andrew, Liz, and Joe. You remind me that physics is a product of love and friendship, and that a collaboration is not made of committees and procedures but passion, honesty,

and good times. To my kindred spirits at the Peanut Barrel – Bob, Ira, Jose, and the rest, thank you for always making room for me. I'll be back. Dean, Katie, Geiger, and my other friends on two wheels, you have kept me in line and helped me that sometimes *not* thinking is better. Dean, especially, you have been an incredible friend and coworker, and you've pushed me to jump in headfirst, eyes open. I owe you a beer.

To the team at SLAC, Hiro, Mark, Kazu, Ran, Francois, Yifan, and Zach, you have given me a home away from home within your group, allowed me to pursue research I never thought myself capable of. It has been an honor to work among you all, and I hope that I can continue to take occaisional refuge within your team.

To my advisors, Naoko and Kendall, who have encompassed my understanding of what it means to be a teacher, mentor, and partner in science. I admire your ability to lead and inspire, without sacrificing what makes you wonderful people. Naoko, you were my first real mentor in physics research. I will never forget the excitement of realizing that physics was not a thing written in a textbook, but something to be discovered and shared. Thank you for convincing me to stay. Kendall, I will never understand how you can accomplish so much so well, and maintain the positivity and encouraging spirit that keeps our group moving forward. You are a leader and a natural helper, and your love of science and teamwork is infectious. Thank you for believing in me.

TABLE OF CONTENTS

LIST OF FIGURES

Figure

ABSTRACT

Design and Calibration of DUNE Liquid Argon Near Detector

by

Daniel Douglas

Chair: Kendall Mahn

The Deep Underground Neutrino Experiment (DUNE) will push forward the frontiers of our understanding of the physics governing neutrino interactions and oscillations. The performance of this experiment relies heavily upon a functional and well-calibrated system of near detectors (ND), comprised of three independent detectors. Of these three detectors, the upstream Liquid Argon Time Projection Chamber (LArTPC) is considered to be the primary target due to its precision and similarity to the DUNE far detector units. The ND LArTPC detector will utilize novel detection techniques such as a highly-segmented drift volume with modularized charge and light readout systems, a pixelated charge readout system for unabmiguous 3D reconstruction of charge, and integrated field shaping devices. These technologies, in combination with the high-rate environment of the Long Baseline Neutrino Facility (LBNF) beam necessitate careful understanding of the drift field and electronics response over time.

This thesis describes the design of the integrated near detector program, including the Precision Reaction-Independent Spectrum Measurement (PRISM) system for high-precision measurement of the unoscillated neutrino flux at the beam source site.

This system allows for motion of the two upstream ND components in the direction transverse to the beam source, allowing for sampling of off-axis flux, granting access to the angular dependence of beam production parameters, and enabling interaction model independent measurement of neutrino oscillation parameters.

This thesis will also discuss a program for spatial calibration of the LArTPC component of the near detector system (ND-LAr, or ArgonCube) using both cosmic rays and a dedicated laser photoelectric charge injection system. Included is an example of this calibration scheme in the Module-0 and Module-1 prototype detectors and an analysis of the findings of these measurements.

CHAPTER I

Introduction

The Deep Underground Neutrino Experiment (DUNE) represents the next generation of long-baseline neutrino oscillation experiments, and one of the largest scientific endeavors in recent history. This international effort is centered around the largest liquid argon time projection chambers (LArTPCs) ever built, designed to measure the most intense neutrino beams ever produced, and will probe the elusive particles which frustrate our current understanding of matter and energy on the smallest scales.

Since the first description of the electron and the electromagnetic field as a quantum field theory, the Standard Model of particle physics has been iterated upon and improved, making increasingly accurate predictions of the behavior of the most fundamental particles known. The theoretical model has expanded to include the weak and strong nuclear interactions, which govern the forces which bind and tear apart the smallest structures in our universe. One of the latest and most spectacular successes of the Standard Model has been the prediction and subsequent observation of the Higgs boson by the ATLAS and CMS experiments using the Large Hadron Collider (LHC), for which the Nobel Prize was awarded in 2013, confirming our understanding of the mechanism by which quarks and leptons get their mass [*Wright* (2013)].

Despite the uncanny ability for this framework to make accurate predictions of the behavior of the universe at its most extreme scales, it remains incomplete. This model

still fails to incorporate the most familiar of the fundamental forces - gravitation - in a consistent way. It also highlights some of the glaring observations of our universe for which there is currently no explanation. Why is the universe seemingly dominated by matter and not antimatter, when the Standard Model is built upon the principles of symmetry between these types of particles? Why does the energy density of the universe seem to include matter which is missing from our observations of distant regions of space? What is the fundamental nature of mass, and how is the Higgs boson and its role related to the interactions which dominate on the scale of galaxies and beyond?

Neutrinos are an elusive type of particle which seem to be least tethered to our understanding of matter. They were first predicted as partners in weak nuclear reactions to the electron and its heavier cousins. Initially, they were assumed to have no mass, no electric charge, and no color charge, so that they were only coupled to the visible world through the weak force. In recent decades, it was discovered that not only do neutrinos have mass, but their mass is incredibly small, almost inconsistent with the mass of other particles within the Standard Model. Additionally, the mass of these particles appears to be misaligned or mixed in such a way that as they travel through space, their flavor will oscillate to an extent not demonstrated by other particles, a finding which was awarded a Nobel Prize of its own in 2015 [*Taroni* (2015)]. This mixing may even be capable of violating the symmetries which have been assumed to be fundamental to the Standard Model. These inconsistencies with the predictions of the Standard Model are tantalizing hints that deeper and more fundamental models of the universe exist, and may only be accessible via these ghostly particles.

The DUNE experiment is designed to measure the behavior of these particles with an unprecedented level of precision. It is carefully designed to answer some of the outstanding questions which have eluded its preceding experiments. It will measure the mechanics of how neutrinos interact with nuclear materials and help to

improve our models of the insides of nuclei. It will measure the details of neutrino oscillation and settle the outstanding question of whether and to what extent neutrino oscillation violates charge and parity symmetry and the role of the neutrino in the current asymmetry seen in our universe. It will measure the differences in the mass states of the neutrinos with improved precision and answer the question of ordering of neutrino masses, shedding light on the ultimate mechanism behind neutrino mass generation. Additionally, DUNE features a robust program for measurement of non-beam and non-neutrino sources, including astrophysical sources such as supernovae, rare predicted processes including proton-decay, and physics beyond the standard model including light dark matter and axion-like particles.

The DUNE experiment relies upon a high-intensity beam of neutrinos produced at Fermi National Accelerator Laboratory (FNAL), at the Long Baseline Neutrino Facility (LBNF). This flux of neutrinos, peaked in the 2-3 GeV region, will travel approximately 1500 km through the Earth to 3 10 kT of precision-instrumented cryogenic liquid argon detectors, where a small fraction of the neutrinos will interact, creating a complex system of electromagnetic and hadronic products. Through the careful reconstruction of these resulting particles, the energy and flavor composition of the beam can be deduced, and the underlying laws which govern the behavior of neutrinos can be measured with higher precision than ever before. DUNE will utilize a high-precision near detector (ND) system, within a very high-rate environment. The ND facility will demonstrate new technologies improving upon the traditional LArTPC design, including modularization, high-density pixelated charge readouts, and a transverse positioning system which will enable new avenues of investigation and measurement of oscillation parameters.

The DUNE collaboration is one of the largest scientific organizations on the planet, involving more than 1000 scientists and engineers from 31 countries. It represents the concerted efforts of many more individuals who have contributed to the technologies,

theoretical understanding, and logistical support needed to measure the most elusive signals on the very largest scales.

This thesis will describe the experiment at large, its questions and methods of inquiry. It will focus on the ND complex and in particular the LArTPC component (ND-LAr) of that system.

Included is a detailed description of the Precision Reaction-Independent Spectrum Measurement (PRISM) system which enables new analyses which side-step some of the largest sources of uncertainty in the measurement of oscillation parameters and studies which demonstrate its methodlogies and advantages over traditional long-baseline analyses.

This thesis will also demonstrate the performance of technologies that will be fundamental to the operation of the ND-LAr system and show methods of calibration and findings using those methods in the prototype systems of ND-LAr. It will discuss the 3D reconstruction of a pixelated charge readout system in a scale demonstrator of the ND-LAr TPC module and demonstrate the necessity of dedicated low-latency systems for measuring drift field shaping device performance.

CHAPTER II

Neutrinos and the Standard Model

2.1 The Standard Model

The Standard Model describes the properties of fundamental particles and their interactions. Its mathematical formulation arises from a quantum field theory and its interactions can be described as belonging to the local symmetry group:

$$\mathrm{SU}(3) \times \mathrm{SU_L}(2) \times \mathrm{U}(1) \tag{2.1}$$

where SU(3) describes the strong nuclear interactions, $\mathrm{SU_L}(2)$ describes the weak nuclear interaction, and U(1) describes the electromagnetic force. These are the three fundamental forces which are described by the standard model of particle physics. The nature of the role of gravitation, the remaining fundamental force, remains the subject of many open questions in physics.

This model includes two main types of particle: fermions and bosons, with the chief difference that fermions have half-integer spin, while bosons have integer-valued spin. Fermions are further comprised of quarks and leptons, and make up most of ordinary matter. Bosons are typically described as "force carriers" and mediate interactions between fermions.

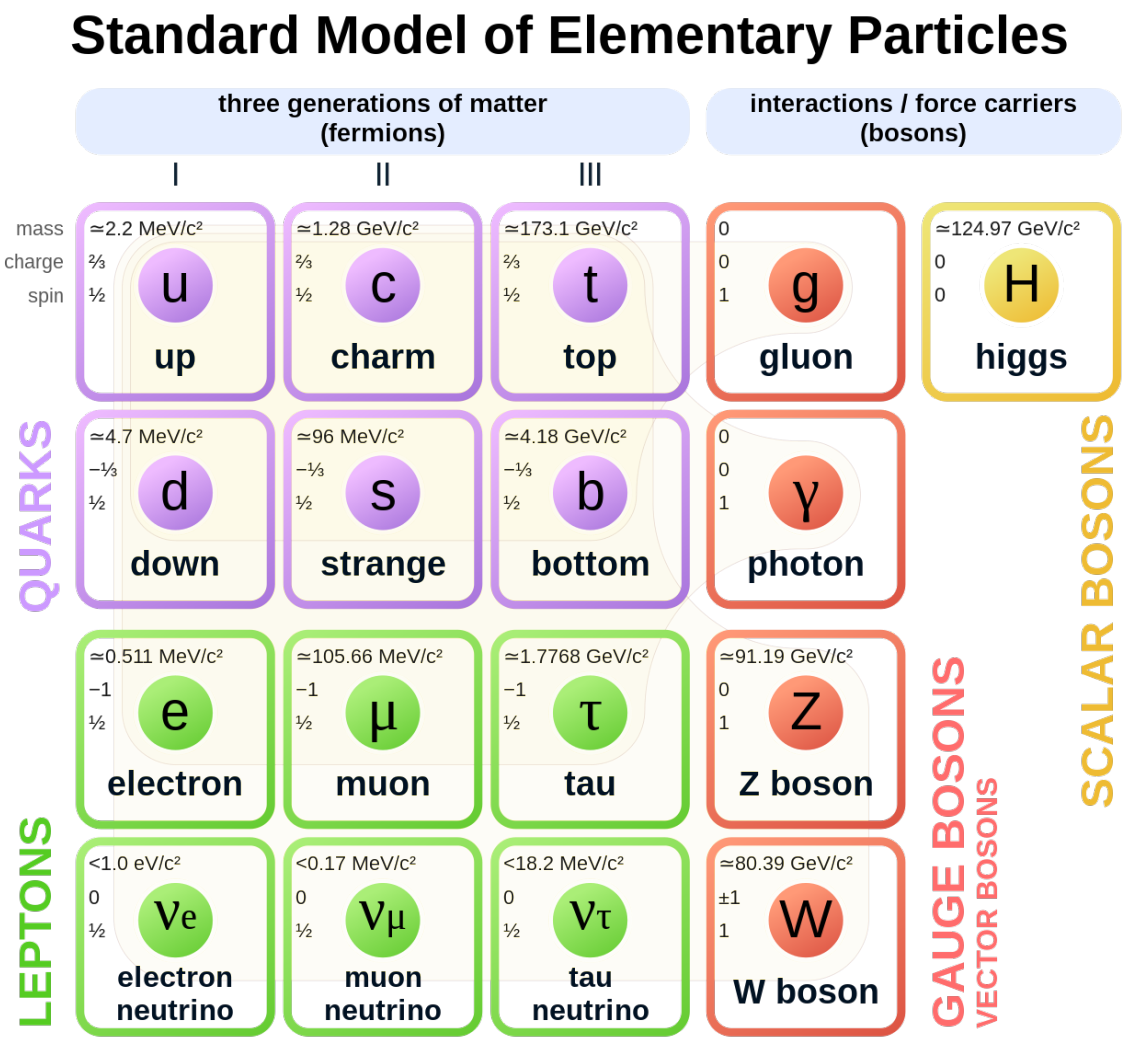

Figure 2.1: A diagrammatic representation of particles within the standard model. Fermions (left three columns) are grouped according to their generation (columns) and their type (row). Each particle type is similar in its quantum numbers, but each successive generation is more massive than the last. Each fermion also has its complementary anti-particle, which is not shown.

The bosons mediate the four fundamental forces:

- Electromagnetic force (photon, γ)
- Weak force (W^+, W^-, Z)
- Strong force (gluon, g)
- Gravity (graviton, not yet observed)

In quantum field theory, fermions are described as bispinors, vectors of four complex numbers which satisfy the *Dirac equation* [*Dirac and Fowler* (1928)], a generalization of Schrödinger's equation and Pauli's description of non-relativistic spin:

$$(i\partial\!\!\!/ - m)\psi(x) = 0 \tag{2.2}$$

Here, the slash notation indicates that a vector has been contracted with the *gamma matrices*,

$$A\!\!\!/ = A^\mu \gamma_\mu, \tag{2.3}$$

which in the Dirac representation, are defined as

$$\gamma^0 = \begin{pmatrix} I & 0 \\ 0 & -I \end{pmatrix} \qquad \gamma^i = \begin{pmatrix} 0 & \sigma^i \\ -\sigma^i & 0 \end{pmatrix} \tag{2.4}$$

$$\tag{2.5}$$

These form the elements of the algebra $\mathrm{Cl}_{1,3}(\mathbb{R})$ which satisfy the anti-commutation

relation $\{\gamma^\mu, \gamma^\nu\} = 2\eta^{\mu\nu} I_4$. In this way, they describe the relationship between the 4-dimensional Dirac space of bispinors and the 3+1-dimensional Minkowski spacetime.

Fermions can be broken down into two categories: quarks and leptons. Quarks make up the majority of normal matter, being the main components of protons (uud) and neutrons (udd). At normal energy scales, quarks are confined to bound states called hadrons because of the strength of the interactions mediated by gluons. The Yukawa potential created by this interaction is such that as a bound state is pulled apart, the creation of a quark-antiquark pair is energetically favorable, resulting in a new set of bound states. This phenomenon is known as quark confinement.

The leptons are composed of the charged leptons (electrons, muons, and taus), which interact with the photons and weak bosons, and their partners, the neutrinos. Neutrinos have no electric charge, and therefore do not interact with the photon field, but are still coupled to the Z and W weak bosons. They are produced and destroyed through weak isospin transformations – interactions mediated by the charged W bosons, also called charged-current interactions. Additionally, they may scatter without charge exchange by neutral-current interactions, mediated by the neutral Z boson.

Fermions are further grouped into three generations or "flavors", with the "normal" matter particles (which include up and down quarks and electrons) in the first generation. Each successive generation contains particles similar in terms of their quantum numbers, but more massive with each generation. For example, the electron's heavier cousins are (in order of generation) the muon and the tau lepton. These three particles each have electrical charge of -1, spin $\frac{1}{2}$, weak isospin $(-\frac{1}{2}, 0)$ (LH, RH), and weak hypercharge $(-1, -2)$ (LH, RH), while the electron has mass 511 keV, the muon has mass 106 MeV, and the tau has mass 1.78 GeV. Furthermore, these higher-generation particles are unstable, presenting an energetically favorable interaction, typically through the weak force, by which they will decay to their lower-generational

counterpart.

2.2 The Weak Force and Symmetry

The weak force exhibits some strange properties that are not seen in other sectors of the standard model. Because of the close relationship between this force and neutrinos, these properties have puzzling implications for the neutrino.

Spinors can be decomposed into two chiral fields:

$$\psi_L = \tfrac{1}{2}(1 - \gamma_5)\psi \tag{2.6}$$

$$\psi_R = \tfrac{1}{2}(1 + \gamma_5)\psi \tag{2.7}$$

Where $\gamma^5 \equiv i\gamma^0\gamma^1\gamma^2\gamma^3$ is the purely anti-symmetric combination of the gamma matrices.

A seemingly reasonable assumption is that the universe behaves in an ambidextrous way. That is, that definitions of left- and right-handedness are simply a matter of convention, and have no impact on underlying physical processes, so that the universe would behave identically on the other side of a mirror as it does on our side. Mathematically, this mirror symmetry is expressed as a *parity operator*, $\hat{\mathcal{P}}$, and if this mirror symmetry holds, such a transformation commutes with other physical operators, such as the Hamiltonian:

$$\hat{\mathcal{P}} \begin{pmatrix} x \\ y \\ z \end{pmatrix} = \begin{pmatrix} -x \\ -y \\ -z \end{pmatrix} \tag{2.8}$$

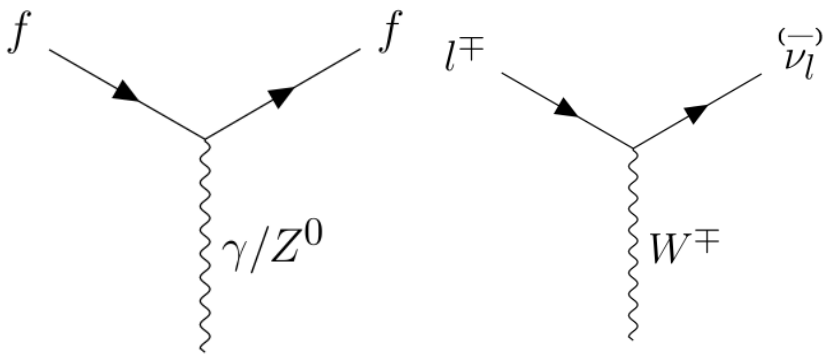

Figure 2.2: Elementary interaction vertices of the electroweak force. Neutral current interactions (left), mediated by Z or γ bosons exchange spin and momentum, while charged current interactions (right) are mediated by $W^{\pm}$ bosons and also exchange charge and flavor.

$$[\hat{\mathcal{P}}, \hat{\mathcal{H}}] = 0 \qquad \text{(for parity invariant systems)} \tag{2.9}$$

In the context of quantum field theory, this operator acts on the chiral spinors in an analogous way:

$$\hat{\mathcal{P}}\psi_L = \psi_R, \qquad \hat{\mathcal{P}}\psi_R = \psi_L \tag{2.10}$$

Another discrete symmetry one can perform on a field of quantum particles is *charge conjugation*, by which one may exchange each particle with its anti-particle, effectively negating the electrical charge of each particle. Taken with the parity operator, it is expected that systems are invariant under $\hat{C}\hat{P}$, that is, an anti-particle will behave as its mirror image for a given potential field.

Observations [*Wu et al.* (1957)] have shown that interactions mediated by W bosons strongly violate this assumption: they are purely left-handed. That is, the products of a charged-current interaction will prefer one chiral state over another. Fermions produced by these interactions will exhibit left handedness, while anti-fermions produced this way will be right-handed.

Many suppose that this indicates that all neutrinos are left handed, while others stipulate that only the left-handed component of the neutrino field can be observed. Modern theories describe neutrinos as either Dirac fermions, which requires a right-handed neutrino field which is only weakly coupled to the Higgs field, or as Majorana fermions, which requires a particular coupling of the left- and right-handed neutrino fields. This second hypothesis has some peculiar implications which are discussed in Section 2.3.4.

2.3 Neutrinos

2.3.1 Properties of the Neutrino

As mentioned in Section 2.2, neutrinos are coupled to other standard model particles only through electroweak interactions. Therefore, their production is only possible through the left-handed charged current and only left-handed neutrinos can be observed through scattering experiments.

Because they are not coupled to the γ field directly, neutrinos are electrically neutral. They do have non-zero weak hyperspin, and can scatter quasi-elastically through neutral current interactions as other fermions, shown in Figure 2.2.

Neutrinos were long thought to be massless, like the photon. The observation of oscillation between neutrino flavors (discussed in Section 2.3.2) has since shown that neutrinos have a non-zero mass, but constraints on that mass require them to have very small value, $< 1eV$. This measurement is reinforced by direct measurement of β decay products, such as the KATRIN experiment, though very accurate measurements of the mass states remains elusive. The drastic difference in the masses of these particles when compared to the bare masses of other fermions presents an open question about the nature of mass beyond the Higgs mechanism. Several alternative mechanisms have been proposed to answer this question, discussed further in Section

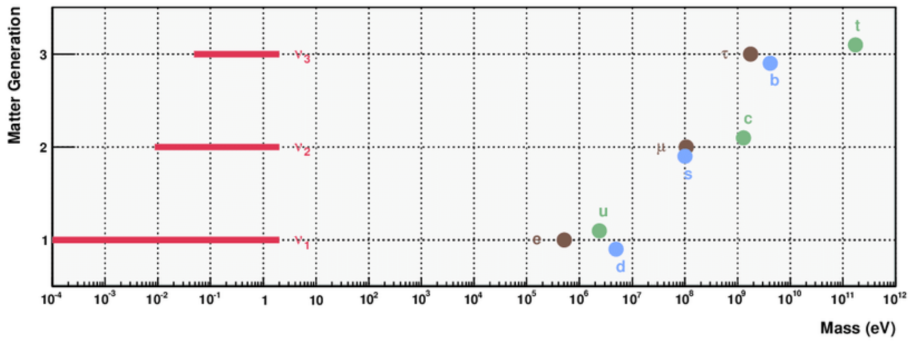

Figure 2.3: A demonstration of the hierarchy problem presented by the mass scale of neutrinos relative to other standard model particles. The horizontal axis indicates the bare mass of each particle in eV, while the vertical axis groups each particle by its generation, with the color of the point indicating each family of particle.

2.3.4.

Lastly, and most provocatively, neutrinos have been observed to oscillate from one flavor (defined as a state upon which the weak interaction operates) to another. This behavior is not unique to neutrinos, but the degree of this oscillation is much greater in neutrinos than in other sectors of the Standard Model.

2.3.2 Mixing

Interaction eigenstates can be mis-aligned to their mass eigenstates. This leads to oscillation because the time-evolution operator (Hamiltonian) acts upon each mass eigenstate according to its individual mass. The interference between the components of an admixture of mass states created as a given flavor state produces a flux whose flavor composition varies as a function of energy and distance from the source.

2.3.2.1 Mixing in the Quark Sector

Quarks are observed to undergo mixing as seen by the variance in strength of various quark decay channels. The charged-current-mediated decay of quarks forces a change of charge, so that, for instance, the strange quark may decay into an up

quark, but not a down quark. This mixing was first described by Nicola Cabibbo [*Cabibbo* (1963)] using a single angle to describe the relationship between the mass eigenstates and the weak eigenstates of the down and strange quarks. The up-type quarks can be defined to have a one-to-one correspondence between mass and weak eigenstates as a choice of basis. Thus, the 2×2 Cabibbo matrix can be expressed as a unitary matrix:

$$\begin{pmatrix} d' \\ s' \end{pmatrix} = \begin{pmatrix} V_{ud} & V_{us} \\ V_{cd} & V_{cs} \end{pmatrix} \begin{pmatrix} d \\ s \end{pmatrix} \tag{2.11}$$

or, using the *Cabibbo angle*, θ_{C},

$$\begin{pmatrix} d' \\ s' \end{pmatrix} = \begin{pmatrix} \cos\theta_{\mathrm{C}} & \sin\theta_{\mathrm{C}} \\ -\sin\theta_{\mathrm{C}} & \cos\theta_{\mathrm{C}} \end{pmatrix} \begin{pmatrix} d \\ s \end{pmatrix} \tag{2.12}$$

Here, d' and s' represent the weak eigenstates of the down-type quarks, while d and s represent the mass eigenstates.

The observation of CP-violation in the decay of kaons [*Christenson et al.* (1964)] requires a unitary matrix of order at least 3×3, which can be parameterized with 3 mixing angles and a single, CP-violating complex phase. This observation by Kobayashi and Maskawa [*Kobayashi and Maskawa* (1973)] prompted the prediction of a higher generation of quarks, and the extension of the Cabibbo mixing matrix into the 3×3 *CKM matrix*:

$$\begin{pmatrix} d' \\ s' \\ b' \end{pmatrix} = \begin{pmatrix} V_{ud} & V_{us} & V_{ub} \\ V_{cd} & V_{cs} & V_{cb} \\ V_{td} & V_{ts} & V_{tb} \end{pmatrix} \begin{pmatrix} d \\ s \\ b \end{pmatrix} \tag{2.13}$$

The current best measurements of these parameters is shown in Equation 2.14 [*Charles et al.* (2005)]. Note that the values shown here describe a highly-diagonal

matrix, with the notable exceptions of V_{us} and V_{cd}.

$$V_{\text{CKM}} = \begin{pmatrix} 0.97446 \pm 0.00010 & 0.22452 \pm 0.00044 & 0.00365 \pm 0.00012 \\ 0.22438 \pm 0.00044 & 0.97359^{+0.00010}_{-0.00011} & 0.04214 \pm 0.00076 \\ 0.00896^{+0.00024}_{-0.00023} & 0.04133 \pm 0.00074 & 0.999105 \pm 0.000032 \end{pmatrix} \tag{2.14}$$

2.3.2.2 Neutrino Mixing and the PMNS Matrix

Similarly to the phenomenon observed in the quark sector, while the mass states of the charged leptons can be defined in terms of their weak eigenstates, the correspondence of their partner neutrinos is allowed to differ as it does for the down-type quarks. Unlike the quarks, however, neutrinos are not subject to confinement, and can exist outside of any bound state. The result is the observation of *neutrino oscillation*, where a flux of neutrinos can change from flavor to flavor in its travel through free space.

The counterpart to the quarks' CKM matrix is known as the *Pontecorvo-Maki-Nakagawa-Sakata (PMNS) matrix* [*Maki et al.* (1962)]. This is a unitary 3×3 matrix, usually parameterized with 3 mixing angles and one CP-violating phase.

$$\begin{pmatrix} \nu_e \\ \nu_\mu \\ \nu_\tau \end{pmatrix} = \begin{pmatrix} U_{e1} & U_{e2} & U_{e3} \\ U_{\mu 1} & U_{\mu 2} & U_{\mu 3} \\ U_{\tau 1} & U_{\tau 2} & U_{\tau 3} \end{pmatrix} \begin{pmatrix} \nu_1 \\ \nu_2 \\ \nu_3 \end{pmatrix} \tag{2.15}$$

Here, as before, ν_e, ν_μ, and ν_τ represent the eigenstates of the neutrinos which couple to the charged leptons through the charged current interaction, while ν_1, ν_2, and ν_3 are the mass eigenstates. The normal parameterization uses the three angles θ_{12}, θ_{13}, and θ_{23}, as well as the complex phase δ_{CP}.

	Normal Ordering (Best Fit)		Inverted Ordering ($\Delta\chi^2 = 2.6$)	
	Best Fit $\pm 1\sigma$	3σ Range	Best Fit $\pm 1\sigma$	3σ Range
$\theta_{12}/^\circ$	$33.44^{+0.77}_{-0.74}$	$31.27 \to 35.86$	$33.45^{+0.77}_{-0.74}$	$31.27 \to 35.87$
$\theta_{23}/^\circ$	$49.2^{+1.0}_{-1.3}$	$39.5 \to 52.0$	$49.5^{+1.0}_{-1.2}$	$39.8 \to 52.1$
$\theta_{13}/^\circ$	$8.57^{+0.13}_{-0.12}$	$8.20 \to 8.97$	$8.60^{+0.12}_{-0.12}$	$8.24 \to 8.98$
$\delta_{CP}/^\circ$	194^{+52}_{-25}	$105 \to 405$	287^{+27}_{-32}	$192 \to 361$

Table 2.1: Current best-fit values and uncertainties on PMNS mixing parameters [*Gonzalez-Garcia et al.* (2021)].

$$\begin{pmatrix} 1 & 0 & 0 \\ 0 & c_{23} & s_{23} \\ 0 & -s_{23} & c_{23} \end{pmatrix} \begin{pmatrix} c_{13} & 0 & s_{13}e^{-i\delta_{CP}} \\ 0 & 1 & 0 \\ -s_{13}e^{i\delta_{CP}} & 0 & c_{13} \end{pmatrix} \begin{pmatrix} c_{23} & s_{23} & 0 \\ -s_{23} & c_{23} & 0 \\ 0 & 0 & 1 \end{pmatrix} \tag{2.16}$$

$$= \begin{pmatrix} c_{12}c_{13} & s_{12}c_{13} & s_{13}e^{-i\delta_{CP}} \\ -s_{12}c_{23} - c_{12}s_{23}s_{13}e^{i\delta_{CP}} & c_{12}c_{23} - s_{12}s_{23}s_{13}e^{i\delta_{CP}} & s_{23}c_{13} \\ s_{12}s_{23} - c_{12}c_{23}s_{13}e^{i\delta_{CP}} & -c_{12}s_{23} - s_{12}c_{23}s_{13}e^{i\delta_{CP}} & c_{23}c_{13} \end{pmatrix} \tag{2.17}$$

where the shorthand $c_{13} = \cos\theta_{13}$ is used. The current best-fit values of these parameters are shown in Table 2.3.2.2 [*Gonzalez-Garcia et al.* (2021)]

2.3.3 Neutrino Oscillation

The phenomenon of neutrino oscillation is a result of the non-diagonality of the PMNS matrix. Neutrinos are created in nuclear reactions and are initially in a well-defined flavor state. The subsequent time evolution of these states is governed by the Hamiltonian operator, which acts differently upon the mass states of the neutrino field, resulting in a flux whose flavor composition is a function of time and position relative to the source.

The earliest observation of this effect is the now-famous "solar neutrino problem", where Ray Davis and John Bahcall's Homestake Experiment, tuned to measure the flux of electron neutrinos originating from the p-p fusion processes within the core

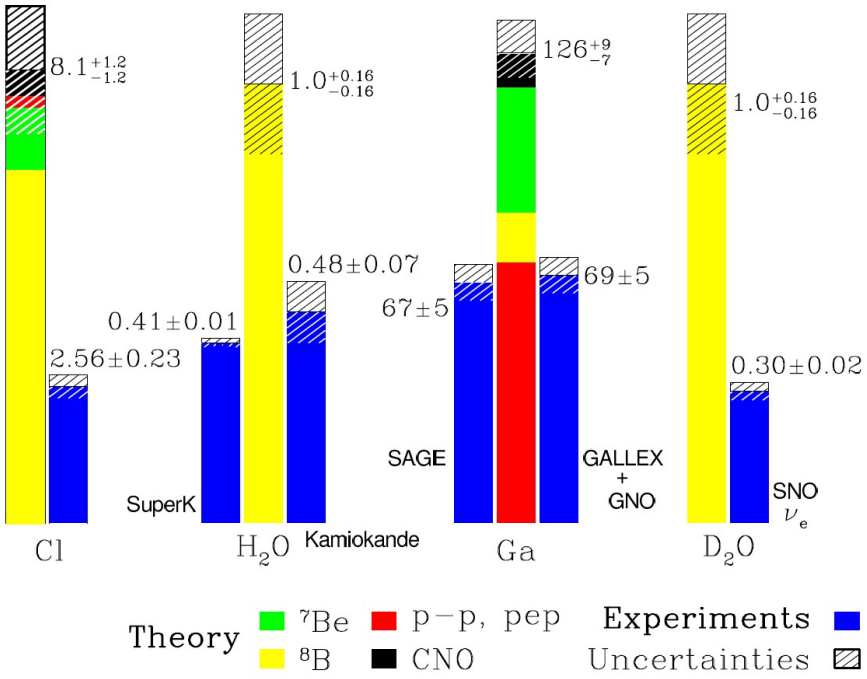

Figure 2.4: The experimentally observed neutrino interaction rate on various target materials compared to their theoretically predicted rate given a no-oscillation transport model. The Homestake experiment (left-most result) measured about 1/3 of the predicted interaction rate, while other subsequent experiments measured different fractions of the overall flux, due to detection methods which allowed for sensitivity to other flavors.

of the Sun, was only able to detect 1/3 of the theoretically predicted flux [*Bahcall and Davis* (1976)]. Subsequent measurements by the Kamioka Observatory and the Sudbury Neutrino Observatory (SNO) confirmed this deficit, with varying fractions of the predicted interaction rate being observed, shown in Figure 2.3.3. Improved neutrino interaction modeling and detection technology has allowed for better identification of individual flavors of neutrinos, leading to the resolution of this problem and the identification of the oscillation of neutrinos.

In a simple example, a weak nuclear process creates a flux of neutrinos with a specific energy and flavor state, $|\nu_\alpha(t=0)\rangle$. This flux of neutrinos can be expressed in the mass state basis by rotation through the PMNS matrix:

$$|\nu_i\rangle = \sum_{\alpha} U_{\alpha i}|\nu_i\rangle \tag{2.18}$$

In vacuum, these mass states propagate independently as a plane wave according to the Hamiltonian operator:

$$|\nu_i(t)\rangle = e^{-i(E_j t - \vec{p}_j \cdot \vec{x})}|\nu_i(0)\rangle \tag{2.19}$$

In the ultra-relativistic limit, which is typically applicable as the neutrino mass is small enough that $p_j >> m_j$ generally applies,

$$E_j = \sqrt{p_j^2 + m_j^2} \approx p_j + \frac{m_j^2}{2p_j} \approx E + \frac{m_j^2}{2E} \tag{2.20}$$

in natural units. With this approximation, Equation 2.19 simplifies to

$$|\nu_i\left(\tfrac{L}{E}\right)\rangle = e^{-i\left(\frac{m_j^2 L}{2E}\right)}|\nu_i(0)\rangle \tag{2.21}$$

The probability that a neutrino of this flux will be detected as a certain flavor at a distance L with energy E is then found by combining Equation 2.18 and Equation 2.19:

$$P_{\alpha\to\beta} = \left|\langle\nu_\beta\left(\tfrac{L}{E}\right)|\nu_\alpha\rangle\right|^2 = \left|\sum_j U_{\alpha j}^* U_{\beta j} e^{-i\frac{m_j^2 L}{2E}}\right|^2 \tag{2.22}$$

$$= \delta_{\alpha\beta} - 4\sum_{j>k} \Re\{U_{\alpha j}^* U_{\beta j} U_{\alpha k} U_{\beta k}^*\} \sin^2\left(\frac{\Delta m_{jk}^2 L}{4E}\right) \tag{2.23}$$

$$+ 2\sum_{j>k} \Im\left\{U_{\alpha j}^* U_{\beta j} U_{\alpha k} U_{\beta k}^*\right\} \sin\left(\frac{\Delta m_{jk}^2 L}{2E}\right) \tag{2.24}$$

where $\Delta m_{ij}^2 \equiv m_i^2 - m_j^2$. Thus, we add two free parameters to the list of oscillation parameters, called the *mass splittings*, with the third mass splitting being constrained

	Normal Ordering (Best Fit)		Inverted Ordering ($\Delta\chi^2 = 2.6$)	
	Best Fit $\pm 1\sigma$	3σ Range	Best Fit $\pm 1\sigma$	3σ Range
$\frac{\Delta m_{21}}{10^{-5} eV^2}$	$7.42^{+0.21}_{-0.20}$	$6.82 \rightarrow 8.04$	$7.42^{+0.21}_{-0.20}$	$6.82 \rightarrow 8.04$
$\frac{\Delta m_{3l}}{10^{-3} eV^2}$	$2.515^{+0.028}_{-0.028}$	$2.431 \rightarrow 2.599$	$-2.498^{+0.028}_{-0.029}$	$-2.584 \rightarrow -2.413$

Table 2.2: Current best-fit values and uncertainties on mass splitting parameters [*Gonzalez-Garcia et al.* (2021)]. Note that the definition of $\Delta m^2_{3l} = \Delta m^2_{31}$ in the case of normal ordering and $\Delta m^2_{3l} = \Delta m^2_{32}$ for inverted ordering

.

by the fact that $\sum_{i>j} \Delta m^2_{ij} = 0$. To complete the list in Table 2.3.2.2, the current best measurements of these parameters are shown in Table 2.3.3.

2.3.3.1 Mass Ordering

As shown in Equation 2.22, the oscillation probability between two flavors depends upon the mass splitting, but not upon the masses themselves. Note also from Table 2.3.3 that the two mass splitting values differ by two orders of magnitude (the "solar" mass splitting, $\Delta m^2_{12} = \Delta m^2_{\text{sol}} \approx 7.4 \times 10^-5$ eV^2 compared to the "atmospheric" mass splitting, $\Delta m^2_{3l} = \Delta m^2_{\text{atm}} \approx 2.5 \times 10^-3$ eV^2). The measurement of oscillation parameters *cannot* directly measure the value of the neutrino masses, only the mass splittings. Because of the relatively small mass splitting between the ν_1 and ν_2 states, there remains some mystery as to the absolute ordering of these mass states, with the two possible scenarios shown in Figure 2.3.3.1. This problem is known as the *neutrino mass hierarchy problem*, and is the target of the next generation of long-baseline (large $\frac{L}{E}$) neutrino oscillation experiments such as HyperK and DUNE. These experiments aim to improve upon the sensitivity of previous experiments to a degree that will resolve the difference between Δm^2_{32} and Δm^2_{13}.

2.3.3.2 The Two-Component Case

As a simplified example, it is helpful to imagine neutrino oscillation between just two flavors. Consider a simplified 2×2 PMNS matrix, which can be parameterized with a single angle:

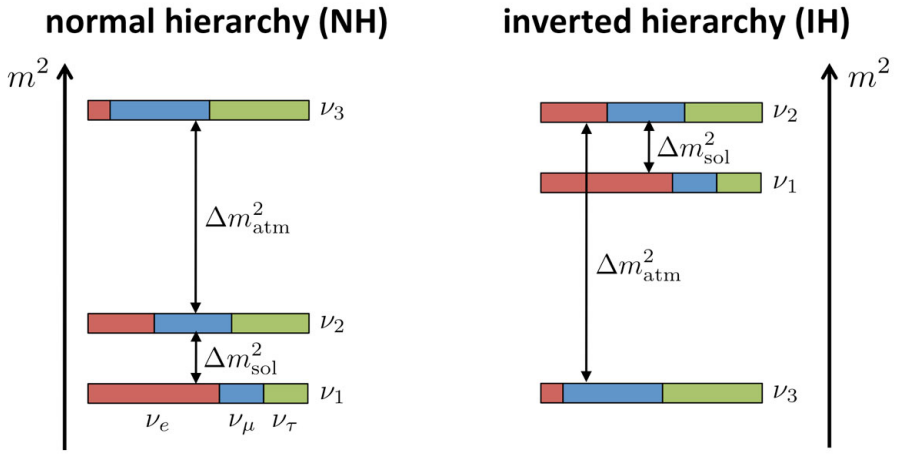

Figure 2.5: The two possible cases by which the neutrino mass states can be arranged, given the current parameter measurements, including the flavor admixture of each mass state. The "normal hierarchy" has the mass states arranged in the order which allows ν_1 to be "most ν_e-like" and so on, while the "inverted hierarchy" has the ν_1 and ν_2 components being significantly more massive than ν_3.

$$U = \begin{pmatrix} \cos\theta & \sin\theta \\ -\sin\theta & \cos\theta \end{pmatrix} \tag{2.25}$$

Then, following the derivation shown in the previous section, the oscillation probability between the two flavors will be

$$P_{\alpha\to\beta,\alpha\neq\beta} = \sin^2(2\theta)\sin^2\left(1.27\frac{\Delta m^2 L}{E}\frac{[\text{eV}^2][\text{km}]}{[\text{GeV}]}\right) \tag{2.26}$$

2.3.3.3 Matter Enhancement of Mixing

The previous sections have discussed the process of neutrino oscillation as it occurs in a vacuum. In matter, however, the Hamiltonian has a non-zero potential term, as there is possibility for coherent scattering of neutrinos with the surrounding matter. This effect is known as the *Mikheyev-Smirnov-Wolfenstein (MSW) effect* [*Mikheyev*

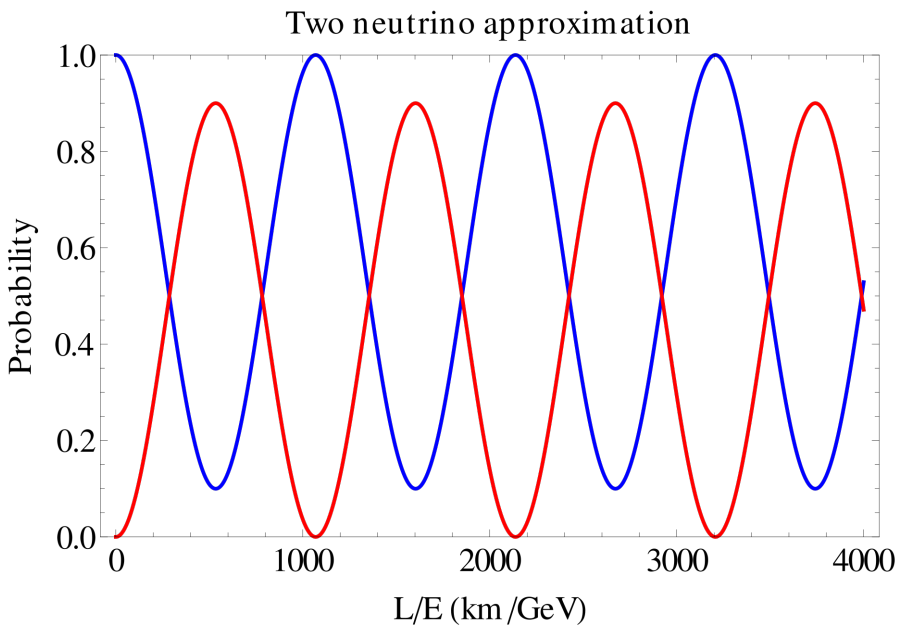

Figure 2.6: The evolution of the oscillation probability between two flavors (assuming parameters similar to atmospheric mixing of $\nu_m u$ to ν_τ) as a function of $\frac{L}{E}$, the baseline.

and Smirnov (1985)], and effectively shifts the mass eigenstates of the neutrino field, altering the interference behavior from its vacuum case.

The mechanism can be understood as the enhancement of oscillation by the coherent forward elastic scattering of electron neutrinos (but not for anti-electron neutrinos), due to the abundance of electrons (but not positrons) in ordinary matter. As this resonant behavior effects neutrinos and anti-neutrinos differently, depending upon the ordering of neutrino masses, this effect can be exploited to improve the sensitivity of an experiment to the true mass ordering. This is a strategy employed by DUNE and its contemporary experiments to help resolve the mass hierarchy problem. Further discussion of DUNE and its physics goals is given in Chapter IV.

2.3.4 Majorana Neutrinos

In 1937, Ettore Majorana proposed another mathematical model to describe spin-$\frac{1}{2}$ fermions as real-valued spinor fields. Such fields inherently obey the charge-conjugation relation:

$$\hat{\mathcal{C}}\bar{\psi}^T = \psi_{\mathcal{C}} = \psi \tag{2.27}$$

As in Equation 2.4, we can choose a basis for the gamma matrices (the *Majorana representation*), which still satisfies the anti-commutation relation but allows for real-valued solutions to the Klein-Gordon equation:

$$\tilde{\gamma}^0 = \begin{pmatrix} 0 & \sigma^2 \\ \sigma^2 & 0 \end{pmatrix} \qquad \tilde{\gamma}^1 = \begin{pmatrix} i\sigma^1 & 0 \\ 0 & i\sigma^2 \end{pmatrix} \qquad \tilde{\gamma}^2 = \begin{pmatrix} 0 & \sigma^2 \\ -\sigma^2 & 0 \end{pmatrix} \qquad \tilde{\gamma}^3 = \begin{pmatrix} i\sigma^3 & 0 \\ 0 & i\sigma^2 \end{pmatrix} \tag{2.28}$$

Where σ^i are the 2×2 Pauli spin matrices. In this basis, the Dirac equation is Hermitian, and purely real bispinor solutions can be found. These are known as *Majorana spinors*. These special spinors have a few unique properties.

Such fermions are eigenstates of the charge conjugation operator. This operator is conventionally understood to relate particles to their anti-particle partners, so this defines a class of massive fermions which are their own anti-particles. These particles would therefore have zero electric charge.

An expression of the Lagrangian in the chiral basis shows that the mass term has some diagonal terms which do not vanish as in the case of Dirac fermions:

$$\mathcal{L}_{\text{mass}} = m_D \bar{\psi}\psi = m_D(\bar{\psi}_L + \bar{\psi}_R)(\psi_L + \psi_R) = m_D(\bar{\psi}_L\psi_R + \bar{\psi}_R\psi_L) \tag{2.29}$$

while in the case of Majorana spinors, the mass term has the form

$$\mathcal{L}_{\text{mass}} = \begin{pmatrix} \bar{\psi}_L \\ \bar{\psi}_R \end{pmatrix} \begin{pmatrix} m_L & m_D \\ m_D & m_R \end{pmatrix} \begin{pmatrix} \psi_L & \psi_R \end{pmatrix} \tag{2.30}$$

These additional mass terms allow for a *seesaw mechanism*, by which such particles can be observed at most energies to behave according to their Dirac mass, while at higher energies, the m_L and m_R Majorana mass terms dominate.

Whether neutrinos can be described as Majorana fermions is still unclear, though some tests of this theory have been carried out. The primary mechanism for testing this hypothesis is the observation of neutrino-less double beta decay, where two beta decay processes can occur in rapid succession, releasing an electron neutrino each time. If neutrinos are Majorana, there is a probability that these two decay products will annihilate within the decay process, with all of the released energy carried away by the electrons and the recoil of the remaining nucleus.

To date, this process has not been observed, despite being the subject of experiments such as EXO-200 [*Anton et al.* (2019)], PandaX [*Ni et al.* (2019)], and CUORE [*and D. Q. Adams et al.* (2022)].

2.4 Outstanding Questions and Experimental Efforts

The above sections outline the current understanding of neutrinos and their unique phenomenology within (and sometimes outside of) the Standard Model. Each of these properties provides a window into the limitations of electroweak theory, mass

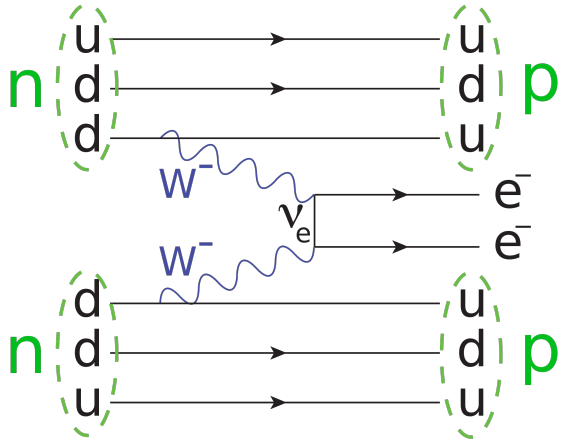

Figure 2.7: A diagram depicting the neutrino-less double beta decay process. In this process, the neutrinos produced by the two beta decays annihilate, leaving all energy to be carried away by the electrons and the remnant nucleus.

generation, and their implications of the evolution of the universe.

For each of these questions, there are several experiments seeking to improve measurements, or observe rare processes predicted by these hypotheses. This section will describe a few of the open questions and some prominent current and future experiments aimed at answering them.

2.4.1 Measurements of Neutrino Oscillation Parameters

Precision measurement of the various terms of the PMNS matrix is important to the development of a more fundamental model of particles. The drastic mis-alignment of mass and flavor eigenstates unique to the leptons may help to untangle the nature of mass beyond the Higgs mechanism. The possibility of CP-violation in neutrino mixing may also play a substantial role in the evolution of the early universe. Lastly, the possibility of the existence of exotic sterile neutrinos has profound implications in the search for a particle explanation of dark matter.

Measurements of these properties are carried out with neutrino oscillation experiments. Such experiments come in a few forms, but are typically categorized as *accel-*

erator, *reactor*, *atmospheric*, or *solar* oscillation experiments, named for the source of the neutrino flux they study. Each of these categories has particular strengths and weaknesses owing mainly to the distances and energies (more precisely, the L/E or *baseline*, as described in Equation 2.26).

Accelerator-based oscillation experiments utilize a particle accelerator and a neutrino production facility, usually centered around a target which produces pions which decay preferentially into μ and ν_μ. These experiments commonly include secondary, near detector systems which increase the precision of the main, far detector by constraining the flux at an earlier stage of the oscillation process. This category of experiment will be discussed in detail in Chapter IV. Prominent experiments of this kind include NOνA, T2K, MINOS, MiniBooNE, and MicroBooNE.

Reactor-based experiments utilize existing nuclear reactors or purpose-built experimental reactors to measure the flux of $\bar{\nu}_e$ produced by the decay of large nuclei. These reactors produce neutrinos of energies of a few MeV. Examples of reactor neutrino experiments include Double Chooz and the Daya Bay Reactor Neutrino Experiment. This baseline provides good resolution of the θ_{13} parameter.

Atmospheric oscillation experiments utilize the natural flux of neutrinos created by the decay of muons originating in cosmic ray air showers. These experiments can obtain very high levels of background rejection by targeting neutrinos which travel through the Earth, giving a baseline of 10,000 km and energies in the range of MeV-TeV. Super-KamiokaNDE, a water Cherenkov detector later utilized as the far detector of the T2K experiment, is an example of this type of experiment.

Solar neutrino oscillation experiments are among the oldest of the oscillation experiments, with the Homestake experiment being the earliest example. The fusion processes in the Sun produce fluxes of a few MeV which can also be studied in small-scale experiments on Earth, providing very precise Solar models. The Sun is also very dense, providing enhancement to normal oscillation through the MSW effect

described in Section 2.3.3.3. The Sudbury Neutrino Observatory and KamiokaNDE can both be considered solar neutrino observatories, though they are also well-suited to study atmospheric fluxes.

2.4.1.1 CP-violation in Neutrino Oscillation

Strong CP-violation is believed to be a necessary condition for baryogenesis, the formation of baryons in the early universe made possible by matter-antimatter asymmetry which is dominant in the universe today. Though maximal values of CP-violation in the neutrino oscillation process may not be sufficient to explain baryogenesis [*Canetti et al.* (2013)] [*Hamada et al.* (2018)], they may play an important role in the overall picture. The DUNE and Hyper-KamiokaNDE experiments will be the first experiments to measure δ_{CP} with enough precision to exclude CP-conserving oscillation (if that is the case).

2.4.1.2 Unitarity of the PMNS Matrix

The PMNS matrix was described as unitary in Section 2.3.2.2. This is a necessary condition for the conservation of neutrino flux within the 3-flavor, 3-mass-state paradigm. Though measurements of the Z boson decay width have shown very good constraints on the number of neutrino flavors which are coupled to the weak bosons, it is possible that more flavors exist which are totally uncoupled from these interactions. Particles such as these have been proposed as possible dark matter candidates, spurring great interest over the possibility of their existence.

Such flavors may only be coupled through the process of oscillation, so experiments are designed to probe specific regions of the phase space where the assertion of PMNS unitarity is least constrained.

Observations made by the LSND experiment of an excess of ν_e-like events (since dubbed the *short-baseline* anomaly) has led to a program of short-baseline experi-

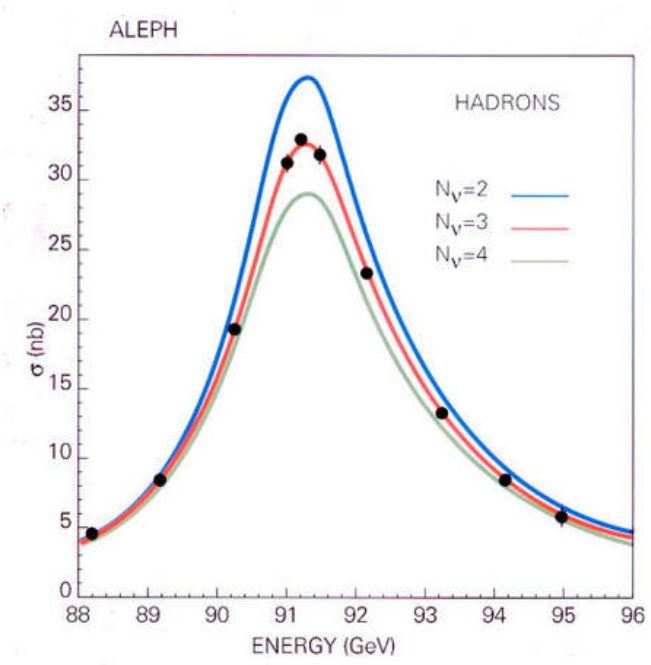

Figure 2.8: Measurements of the width of the Z boson decay by the ALEPH experiment have shown that the best-fit number of active neutrino flavors is 3.10 ± 0.10. This does not preclude the existence of sterile flavors which are coupled only through oscillation.

ments includinge the Booster Neutrino Experiment (BooNE) and its successors, MiniBooNE and MicroBooNE. The latest set of analyses from the MicroBooNE experiment [*Denton* (2022)] show no evidence to support one or more additional neutrino flavors.

2.4.1.3 Mass Hierarchy

Though the PMNS matrix is highly non-diagonal, one would expect that, in keeping with the other Standard Model particles, the heaviest of the mass states is composed in most prominently of the τ flavor state. Likewise, the second heaviest should be mostly μ-dominated, and the lightest should be primarily e-like (Figure 2.3.3.1). Because of the great disparity between the atmospheric and solar mass splittings and the difficulty of performing absolute measurements of mass states, resolving this hierarchy has remained elusive. Future experiments, such as DUNE and Hyper-KamiokaNDE seek to resolve the Δm^2_{13} and Δm^2_{23} mass splittings and settle the true ordering of the neutrino mass eigenstates.

2.4.2 Neutrino Interactions and Kinematics

Many of the above oscillation experiments rely on very accurate measurements of the neutrino nucleon cross section for accurate inference of fluxes from measurements of interaction rates. This is further complicated by the fact that many target materials are much more complex than a single-nucleon system. Complicated nuclei (for example, Ar_{40}) can sustain interactions on the whole nucleus, or groups of nuclei.

2.4.2.1 Direct Measurement of Neutrino Mass

Direct measurement of neutrino masses is not accessible to oscillation experiments as shown in section 2.3.2.2. These parameters, can however be measured by precise kinematic measurements of nuclear decays. The KATRIN experiment seeks to mea-

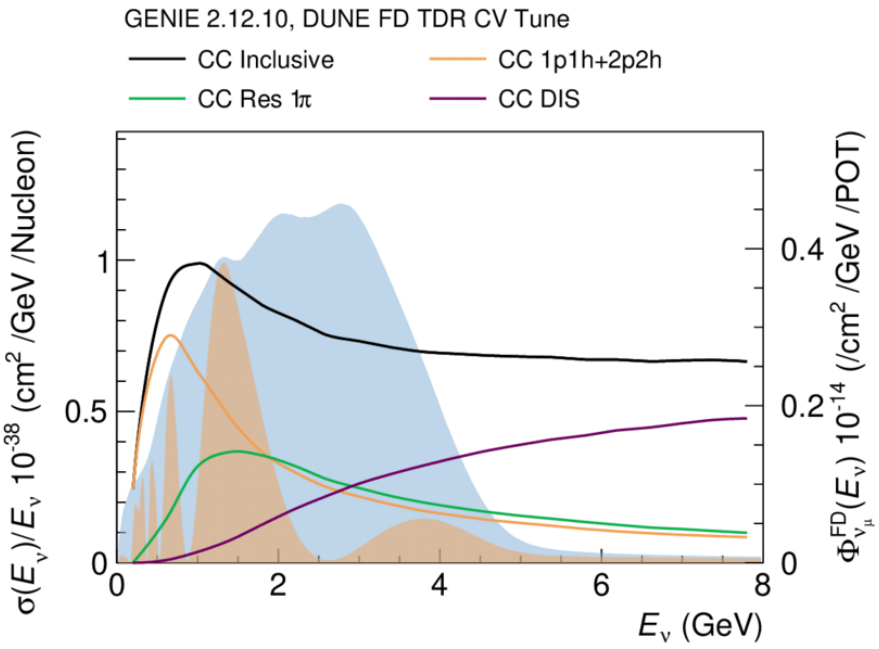

Figure 2.9: Charged current neutrino interaction cross sections in the DUNE interaction model as a function of true neutrino energy. The blue and orange filled regions show the unoscillated and oscillated, respectively, ν_μ flux at the far detector, for reference [*Collaboration et al.* (2021)].

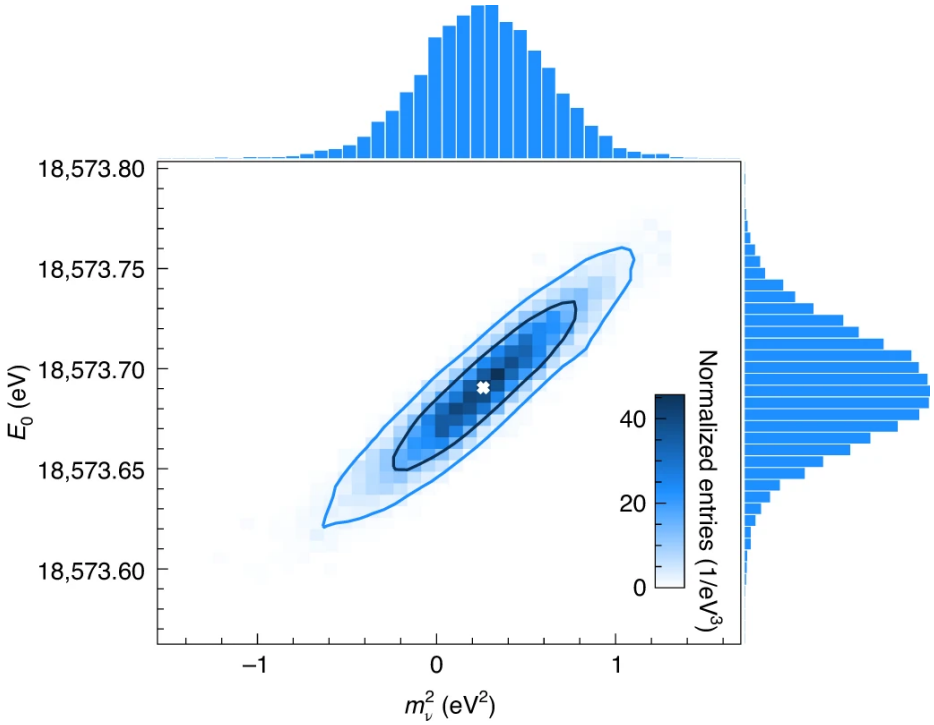

Figure 2.10: Confidence regions of the KATRIN measurement of the neutrino mass, inferred from the energy of decay products of Tritium in flight. The 90% CL sets an upper limit of $m_\nu < 0.9eVc^{-2}$.

sure the β decay of Tritium and measure the energy of the resulting non-neutrino fragments to infer the mass of the neutrino. Since the produced ν_e is an admixture of the three mass-basis states, this is in a sense another indirect measurement, but can be combined with PMNS measurements to infer ν_1, ν_2, ν_3. Current results set an upper limit on this decay product mass of $m_\nu < 0.9eVc^{-2}$ [*Aker et al.* (2022)].

2.5 Conclusion

Neutrinos present one sector of the Standard Model in which new phenomena are being observed. New technology is beginning to enable tests of theories which were once thought inaccessible, and the unique nature of neutrinos may lead to results impacting many fields of physics.

The observation of neutrino oscillation and the implication of (tiny) neutrino mass

leaves a puzzle as to the nature of mass. This oscillation behavior may violate CP-symmetry, adding another avenue outside of the charged-current interaction by which symmetry is broken in the early universe. The possibility of the existence of sterile neutrinos has not been ruled out, and such particles may be intimately linked to dark matter.

CHAPTER III

The Time Projection Chamber

3.1 Principle of Operation

The time projection chamber (TPC) is a detector design concept which first appeared in the PEP ring experiments at SLAC National Accelerator Laboratory in the 1970's [*Willis and Radeka* (1974)]. The operating principle is to surround a target volume of liquid or gas with a strong electric field, with one electrode bearing instrumentation for the measurement of ionized particles. Energetic particles which pass through this volume will deposit energy in the form of ionization, leaving characteristic tracks that trace out the path of the particles and their secondary particles which are created as they scatter or decay through the material. The strong electric field then applies a force to those tracks of ionized material, drifting the positively charged ions towards the cathode, and the negatively charged electrons towards the anode.

In a typical TPC, the anode is instrumented with sensitive electrodes, usually a series of planes of parallel wires or a set of pixels or pads. These anode assemblies can reconstruct a 2-dimensional projection of the deposited charge, and by combining these 2-D images with information about the arrival time of each charge bundle, a fully 3-dimensional reconstruction of the ionization can be made.

The preceding description of this reconstruction method is missing a key step: how does one know the absolute position along the direction of charge drifting if only

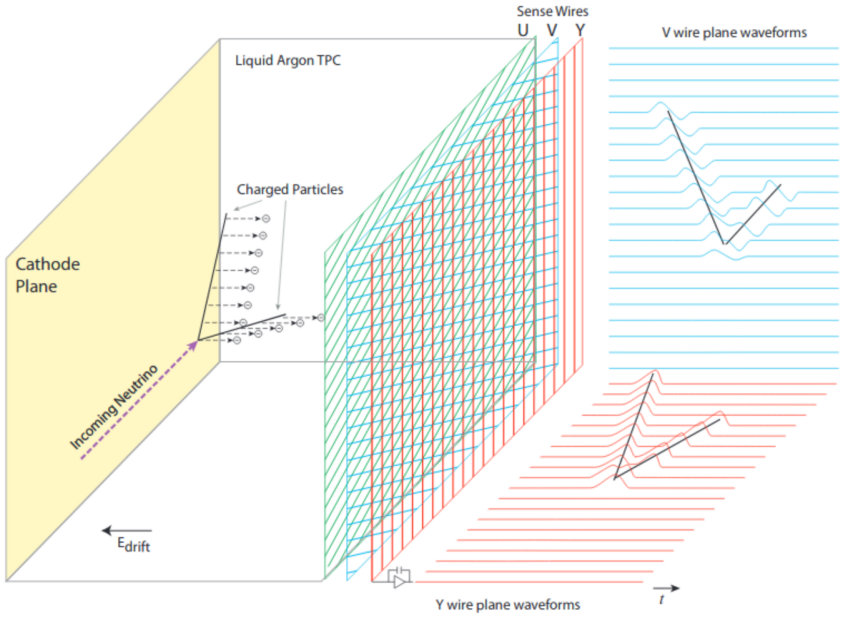

Figure 3.1: Design and operation principle of a wire-plane TPC.

the relative differences in timing are measured? To put it another way: how can one know the time that an event began, if there is a unknown period of time during which the deposited charge must drift towards the instrumented anode? One solution to this issue was proposed in 1977 independently by Carlo Rubbia [*Doke* (1993)] and Chen *et al.* [*Chen and Lathrop* (1978)] in the form of a liquid-argon time projection chamber (LArTPC). This complication to the usual design uses liquefied argon, a noble gas readily found in air, as the target material and takes advantage of the fact that, as part of the ionization process, several short lived atomic states of argon are created and decay, producing scintillation light. The scintillation light produced in this way is of a wavelength (126 nm [*Hofmann et al.* (2013)]) to which LAr is mostly transparent, allowing the light to propagate to dedicated light detection systems, which provide the t_0 for a given particle interaction. From this information, the drift distance can be reconstructed:

$$d_{\text{drift}} = (t_{\text{arrival}} - t_{\text{deposition}})v_{\text{drift}} \tag{3.1}$$

3.2 Particle Interaction and Energy Deposition

A particle's probability to interact with a given target is usually characterized by its *cross section*, σ. This quantity, which is calculated or measured independently for a given particle-target pair, describes the relative increment of a flux Φ that will interact within a target:

$$\frac{\mathrm{d}\Phi}{\mathrm{d}z} = -n\sigma\Phi \tag{3.2}$$

The units of cross section are *barns* (b), with $1\,\mathrm{b} = 10^{-28}\,\mathrm{m}^2$. A related concept to the cross section is the *mean free path*, λ:

$$\lambda = \frac{1}{n\sigma} \tag{3.3}$$

This value is usually more physically intuitive, as it describes the mean distance a particle may travel through a medium between given interactions. As with cross section, this quantity is dependent upon both the material and the radiation traversing it. As described in Chapter II, neutrinos have a very low probability to interact with normal matter. For example, the mean free path of an electron in gas is approximately 10^{-5} cm. In contrast, a neutrino's mean free path through a (much) denser material like solar plasma is upwards of 100 light-years.

For most other particles, including the many of those produced by neutrino inter-

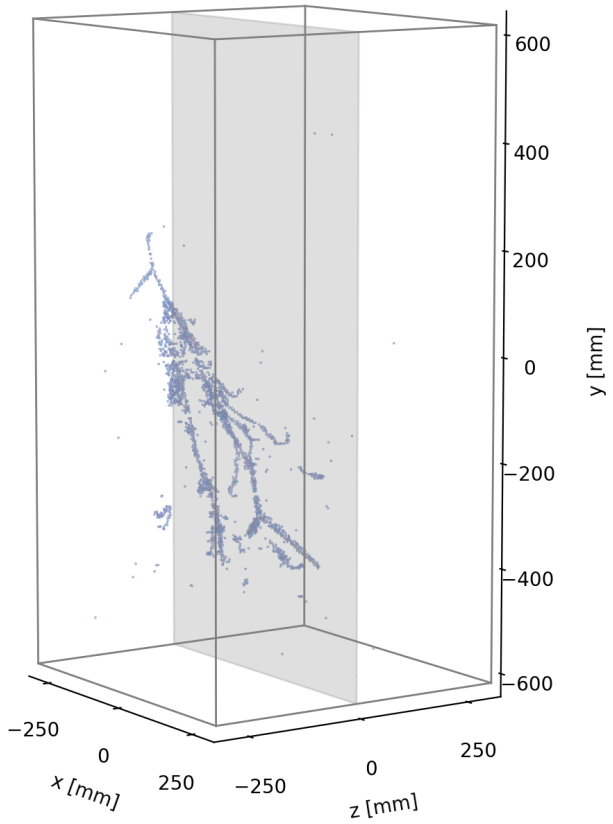

Figure 3.2: A cosmic ray particle interacting in Module0, creating an electromagnetic shower with many secondary particles.

actions, collisions are much more frequent. Instead of considering a beam of many particles attenuating as individuals interact with the surrounding matter, we instead model the way a single particle may evolve as it exchanges energy through small, stochastic interactions. The mean energy loss experienced by an energetic charged particle traveling through matter is typically described by the Bethe-Bloch formula:

$$-\left\langle \frac{\mathrm{d}E}{\mathrm{d}x} \right\rangle = \frac{4\pi}{m_e c^2} \frac{nz^2}{\beta^2} \left(\frac{e^2}{4\pi\epsilon_0} \right)^2 \left[\ln\left(\frac{2m_e c^2 \beta^2}{I(1-\beta^2)} \right) - \beta^2 \right] \tag{3.4}$$

where c is the speed of light, ϵ_0 is the vacuum permittivity, $\beta = \frac{v}{c}$, e is the charge of the electron, and m_e is its mass. This energy loss, also called *stopping power*, is dependent upon the material through which the radiation is traveling and its dependence is characterized by I, the ionization potential of the material.

It must be reiterated that this is an empirical formula, and the angle brackets around $\frac{\mathrm{d}E}{\mathrm{d}x}$ indicate that this is an *average* loss of energy. In reality, this process is quite noisy, with individual energy losses occurring randomly, sometimes with transfer of momentum in a transverse direction, imparting kinks and turns to a particle's track which complicate analysis. Furthermore, these particles can undergo secondary interactions aside from simple ionization, which may produce new particles of different mass and charge, or be absorbed by heavy nuclei which produce very little visible recoil. In the case of hadronic particles, it is typical for secondary interactions to re-interact themselves in an avalanche-like process, forming what is known as a *cascade*-type event (Figure 3.2).

To properly understand these interactions, one must simulate these interactions on a very large scale using computer implementations of such models. One widely-used framework for geometry and tracking is GEANT4 [*Agostinelli et al.* (2003)], which is used in high-energy physics for modeling fluxes and detectors.

3.3 Recombination

After a number of Ar atoms become ionized, several atomic and molecular process can take place, producing both charge and light in with different time-signatures characteristic to each process. Figure 3.3 shows two common processes that an Ar atom may undergo after interaction with an energetic particle: excitation and ionization.

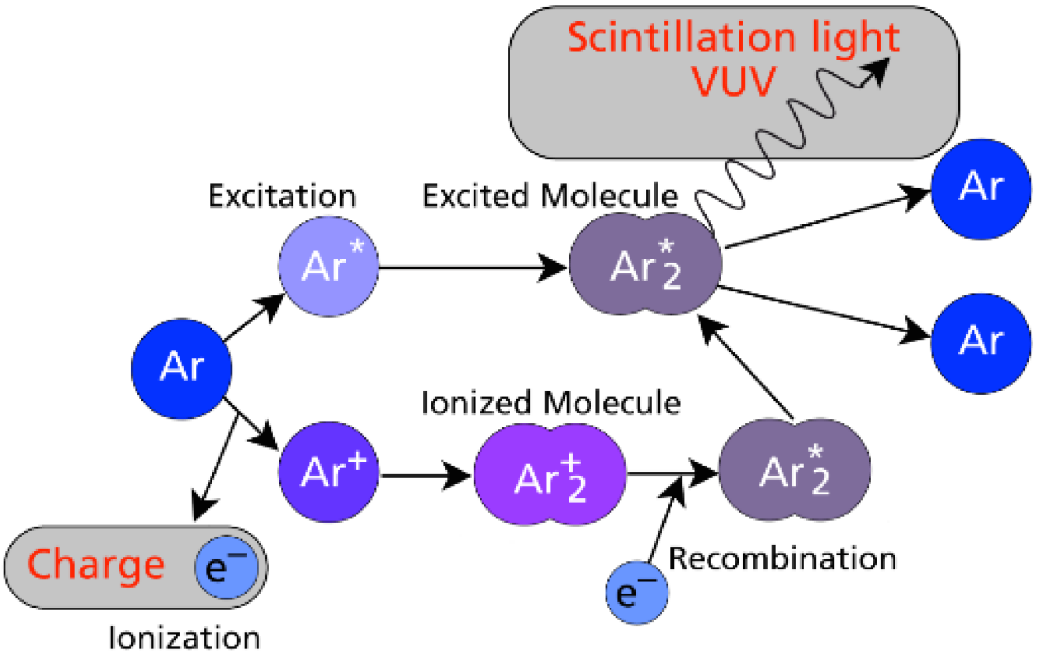

Figure 3.3: Diagram of different process that may produce charge and light following interaction with an energetic particle. [*Araujo* (2019)]

The cross-sections for each process in the diagram is well-understood, but correctly modeling the "recombination" step is very important to map the amount of charge and light observed to the energy deposited in the LAr.

Once electrons are freed from the bound state of the Ar atom, their spatial distribution is thought to be uniform about the remaining ion. Because of the action of the external electric field and the attractive potential between the newly-charged

remnants (and their similarly-produced neighbors), some fraction of these electrons will find their way back to an Ar^+ ion and recombine, without producing a signal.

The two most commonly considered models for this action are the *Birks model* and the *Box model*. In the Birks model, it is assumed that electrons have a gaussian spatial distribution about the ionizing particle's trajectory during the recombination step. It is also assumed that the charge mobility, μ, is the same for electrons and ions. Assuming the electric field strengths typical for a LArTPC (500 V/cm), the model can be simplified to:

$$\mathcal{R}_{\text{Birks}} = \left[1 + k_c \frac{\mathrm{d}E/\,\mathrm{d}x}{\mathcal{E}\sin\phi}\right]^{-1} \tag{3.5}$$

Where k_c is a model parameter specific to liquid argon, $\mathrm{d}E/\,\mathrm{d}x$ is the rate of energy loss in a small segment of the primary particle's track, $\mathcal{E}$ is the local electric field, and ϕ is the relative angle between the drift field and the primary particle's trajectory. In this model, $\mathcal{R}$ corresponds to the fraction of electrons which *survive* the recombination process [*Acciarri et al.* (2013)].

A simpler model, proposed by Thomas and Imel [*Thomas and Imel* (1987)] assumes that electron diffusion and mobility are negligible in LAr. Dropping these terms and applying "Box" boundary conditions, they state:

$$\mathcal{R}_{\text{Box}} = \frac{1}{\xi}\ln(1+\xi), \text{ where } \xi = \frac{k_{\text{Box}} N_0}{4a^2\mu\mathcal{E}} \tag{3.6}$$

3.4 Attenuation and Diffusion

As the ionization electrons drift through the LAr, impurities such as oxygen and Hydrogen can interact and absorb them, attenuating the total signal. As these impu-

rities are roughly homogeneous within the active volume, the amount of attenuation is modeled as an exponential dependence on the overall drift time of a given charge bundle:

$$Q(t) = Q_0 e^{-t/\tau}, \tag{3.7}$$

where $\tau = \frac{1}{\lambda v}$ is a function of the overall purity of the LAr and is referred to as the "electron lifetime", λ being the mean free path.

In addition to absorption, the thermalized electrons will undergo repeated collisions with the surrounding Ar molecules, in a semi-random-walk-like process. This results in diffusion on a charge-cloud scale, which is different in the direction of the drift field (longitudinal) than in the directions perpendicular to the drift field (transverse). The result is that a point-like cloud of charge deposited at some initial position $z = 0, \rho = 0$ at a time $t = 0$ will evolve into a deformed gaussian cloud, including an extinction term which depends on the drift time as in Equation 3.7 [*Li et al.* (2016)]:

$$n(\rho, z, t) = \frac{n_0}{4\pi D_T t \sqrt{4\pi D_L t}} \exp\left(-\frac{(z - vt)^2}{4D_L t} - \lambda v t\right) \exp\left(-\frac{\rho^2}{4D_T t}\right) \tag{3.8}$$

At fields similar to those used in the DUNE LArTPC's (500 V/cm), the value of the diffusion coefficients are $D_L = 7.2\,\mathrm{cm}^2/\mathrm{s}$ and $D_T = 12.0\,\mathrm{cm}^2/\mathrm{s}$ [*Li et al.* (2016)].

Finally, we consider that Equation 3.8 describes the evolution of point-like charge distributions, while charge deposition in LAr is typically along the path of an energetic particle, and is modeled as a series of small, linear segments. The evolution of these segments is modeled by simulation frameworks like `larnd-sim` as a convolution of Equation 3.8 with a line source, and evaluated at the surface of a pixel ($z = z_{\mathrm{deposition}} - z_{\mathrm{anode}}$) at time $t = z/v_{\mathrm{drift}}$.

3.5 Charge Collection

Measuring the free charge within the volume is not as straightforward as measuring the rate of arrival of charges at the anode. In fact, free charges within the volume will begin to induce electrical currents on electrodes in the volume from the time they begin to drift. Therefore, an accurate model of the detector must include thorough simulation of the drift process and the electrostatic system.

3.5.1 Charge Transport in Liquid Argon

The transport of electrons within LAr is dominated by electromagnetic interactions, so the typical Coulomb forces do not apply on a macroscopic scale. Instead, an effective model is constructed from a combination of a fit to ICARUS data [*Amoruso et al.* (2004)] at low fields and the Walkowiak model [*Walkowiak* (2000)] at high fields. The combined model is shown in Figure 3.4.

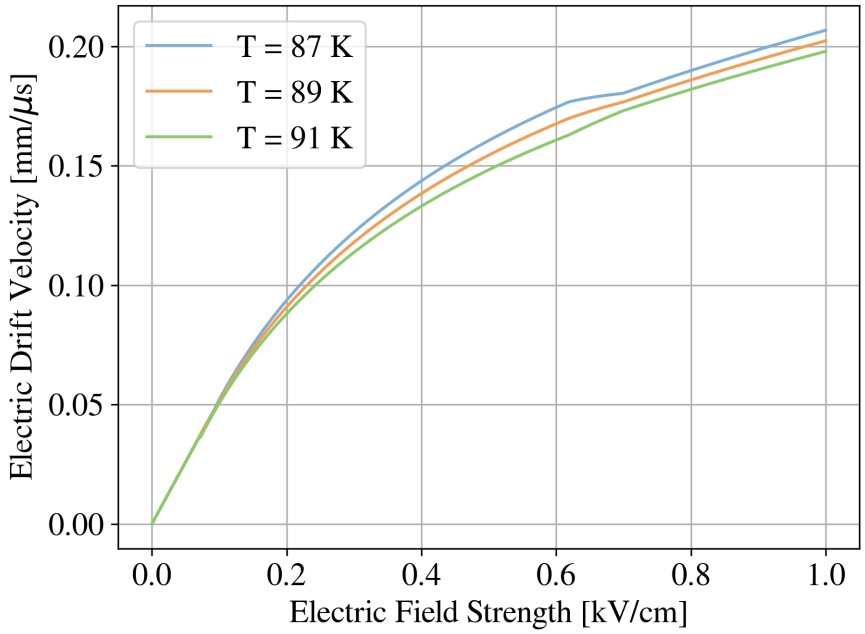

Figure 3.4: The drift model obtained from combining the results of measurements using the ICARUS experiment [*Amoruso et al.* (2004)] and the Walkowiak model [*Walkowiak* (2000)].

To simulate the mean path that a charge bundle will take as it drifts through the volume, an FEM calculation of the TPC geometry is performed to obtain a model of the electric field. Then, starting from a grid of positions a small distance into the drift volume, each test charge is numerically integrated according the the model described in Figure 3.4. This calculation is performed only for the volume nearest to the anode, where the electric field is expected to differ significantly from the nominal drift field within the volume. Some examples of these calculated drift paths are shown in Figure 3.5.

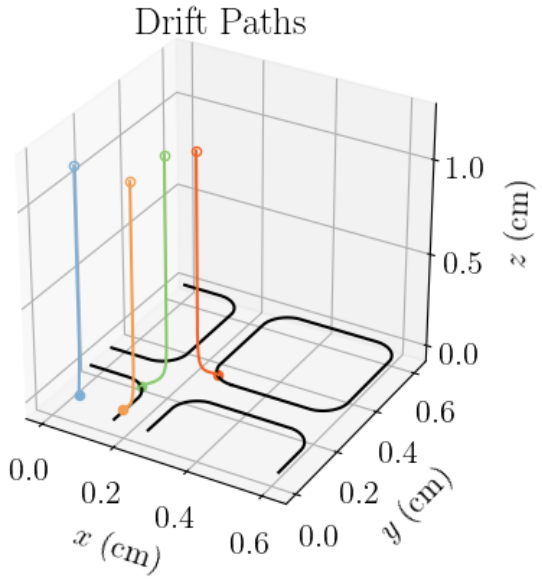

Figure 3.5: An example of a few drift paths within the pixelated anode geometry of DUNE ND-LAr.

3.5.2 Electrode Response and the Ramo Theorem

The current response of an electrode in the presence of a moving charge is more than just the arrival rate of individual charge carriers. Instead, it is helpful to think of this process as a problem of image charges. As a given charge carrier approaches, for instance, a conductive plane which is divided into pixels which are kept at a certain

voltage by an external power supply, the charge will induce an image charge on the plane as a whole. As the charge moves nearer and nearer to a single pixel, the induced charge will become greater in that single pixel, while becoming weaker in the others. Finally, as the free charge actually reaches the pixel, it meets with its image charge which is now very near to the magnitude of the free charge itself. Thus, we have the *weighting field*, or *weighting potential*, which is analogous to the electric field of a system, but is the solution obtained when the electrode of interest is fixed at unit potential while the remaining electrodes in the system are set to ground. This field describes the "field of view" of a single electrode in the system, with some notable properties:

- The weighting field for a given electrode is between 0 and 1 across the system
- The sum of weighting fields for every electrode in the system is 1 everywhere within the system

This field was first described by William Shockley [*Shockley* (1938)] and Simon Ramo [*Ramo* (1939)] in their theorem, which further states that the current induced on such an electrode of interest is given by

$$i = q\vec{E}_{\mathrm{W}} \cdot \vec{v} \tag{3.9}$$

Where q is the magnitude of the charge moving near the electrode, $\vec{E}_{\mathrm{W}}$ is the electric field corresponding to the weighting potential, and $\vec{v}$ is the velocity of that charge. Applying this theorem, using a weighting potential calculated with an FEM solver in the same manner as was done for the drift field, we obtain the current as a function of time for several test charge positions (Figure 3.6).

Charges which terminate on the electrode of interest will have a positive integral – in fact, this integral is identically q, as can be seen from Equation 3.9 and the

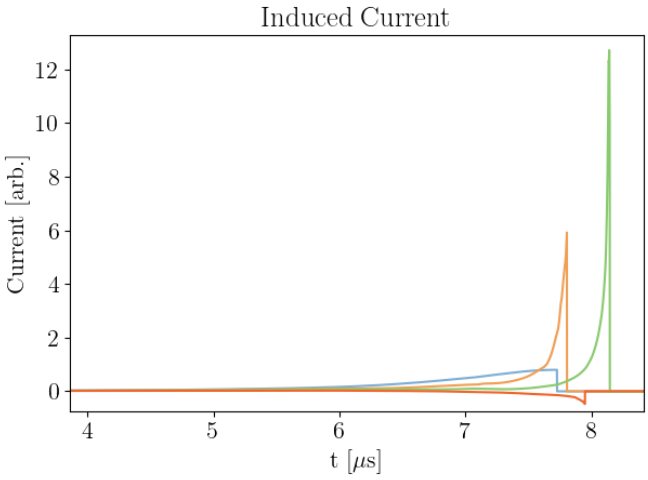

Figure 3.6: The current time-series calculated for the drift paths shown in Figure 3.5. Note that the paths which terminate on the left-most pixel (the pixel of interest here), the current is strictly positive (unipolar), while for the test charge which terminates on a neighboring pixel, the current is both positive and negative (bipolar).

definition of the weighting field. Meanwhile, neighboring pixels will see a bipolar pulse, whose integral is 0. In a highly-symmetric system such as a large plane of identical pixels, this calculation can be transposed onto every pixel in the system.

3.6 Light Detection Systems

In addition to the charge readout systems described above, TPC's will typically also contain one or more systems for detecting scintillation light created during the dimerization process shown in Figure 3.3. The photons created during the decay of the Ar_2^* dimer, particularly those in the 3rd continuum emission, will propagate through the argon with very little scattering.

Large-area light tiles with wavelength shifting coatings are positioned perpendicularly to the anode planes. These tiles will collect and guide light towards silicon photomultipliers (SiPM's), which collect and digitize these signals on the order of 10's of ns. These signals provide an external trigger for the charge collection systems

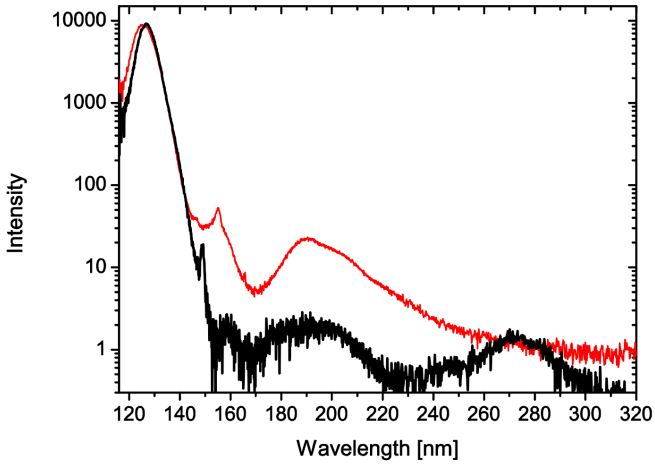

Figure 3.7: The VUV/UV emission spectrum of liquid argon at 85 K, compared to the spectrum of gaseous argon (red) at 295 K, 300 mbar. The spectrum is dominated by a broad emission line at 126.8 nm, analogous to the 2nd excimer continuum of the gas phase. The structure around 270 nm is analogous to the 3rd continuum emission of the gas phase [*Heindl et al.* (2010)].

which is relatively slower (charge signals drift to the anode between 0 and 300 μs, depending upon their initial drift position).

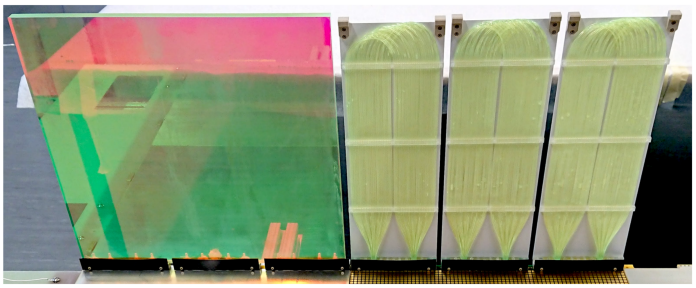

Figure 3.8: An ArCLight tile (left) and three LCM tiles (right) fitted to LArPix tiles during assembly of Module0.

3.7 Drift Field Uniformity

Of great importance to the successful execution of the principles outlined in this chapter is the accurate modeling of the drift field. In most cases, it is assumed that the electric field is uniform across the entirety of the active volume and its direction is perfectly aligned along the anode-cathode axis. In reality, the drift field is formed by a *field cage* or *field shell* made out of several resistive and conductive elements and powered by a high-voltage delivery system external to the TPC and cryostat.

CHAPTER IV

The Deep Underground Neutrino Experiment

The Deep Underground Neutrino Experiment (DUNE) is a next-generation neutrino oscillation experiment which seeks to answer the outstanding questions regarding the role of neutrinos in the our universe. The prevalence of matter over anti-matter, the complex dynamics of supernova neutrino bursts that are a vital part of the production of heavy elements necessary for life, and other rare processes like proton decay are main focuses of this experiment. These questions, in addition to those discussed in Chapter II, have informed the design of this detector which is the result of the work of an international collaboration of more than 1000 scientists and engineers from 31 countries (Figure IV).

4.1 Introduction to Long-Baseline Oscillation Experiments

DUNE expands upon the paradigm of the long-baseline neutrino oscillation experiment. Its predecessors include T2K and NOνA, which both feature a neutrino beam production facility, a robust near detector (ND), and a large far detector FD. The principle of operation for this type of experiment is to measure the flux of neutrinos of a given flavor at both the near site and the far site, and by comparison of the relative composition of the beam at each site, make measurements of the underlying physical model parameters described in Section 2.3.3.

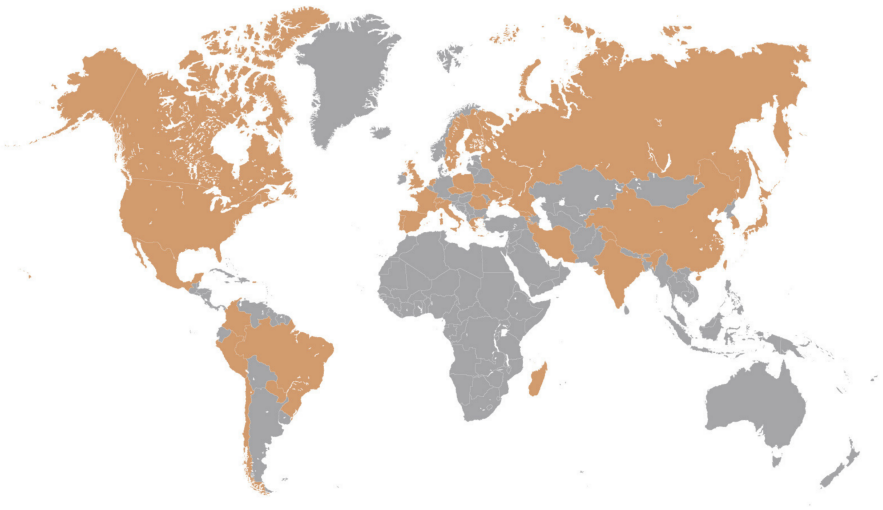

Figure 4.1: The international DUNE collaboration. Countries with institutional members in DUNE are highlighted in light brown.

In practice, there are several methods by which the measurement of oscillation parameters can be done. The simplest experiment one can imagine does not require an ND at all, but instead relies upon precise modeling of the flux produced by the beam to make a prediction of the neutrino components at the site of production *ab initio*. This method is very susceptible to the uncertainties associated with the production of neutrinos due to the complex hadronic processes that occur within the nuclear targets. Proton beams impinge upon a target (typically graphite/carbon) [*Tariq et al.* (2016)], producing hadronic cascades which are subsequently focused using magnetic horns so that their $\pi^{\pm}$ components are relatively re-focused. This pion component then decays in a long *decay pipe*, producing primarily $\mu^{\pm}$ and ν_{μ} ($\bar{\nu}_{\mu}$). The muon component is absorbed by a length of inert material so that they are sufficiently thermalized before their own decay, so as not to contribute to the overall beam neutrino flux.

The details of this chain of particles are subject to very small deviations in the geometries of the beam target, the focusing horns and their electromagnetic char-

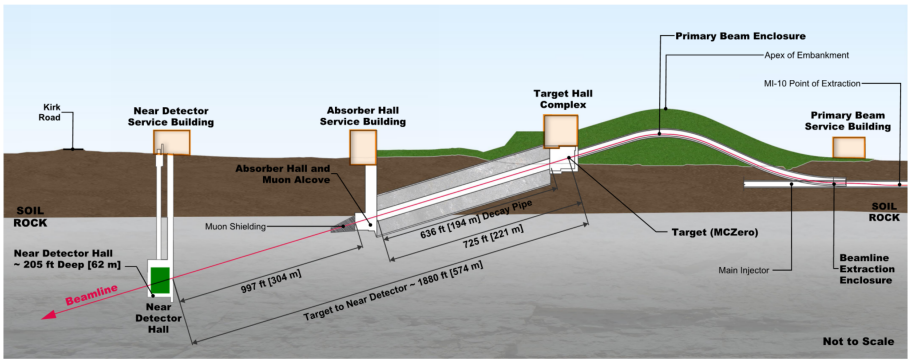

Figure 4.2: The LBNF neutrino beamline including the near detector hall at Fermi National Accelerator Facility in Batavia, Illinois.

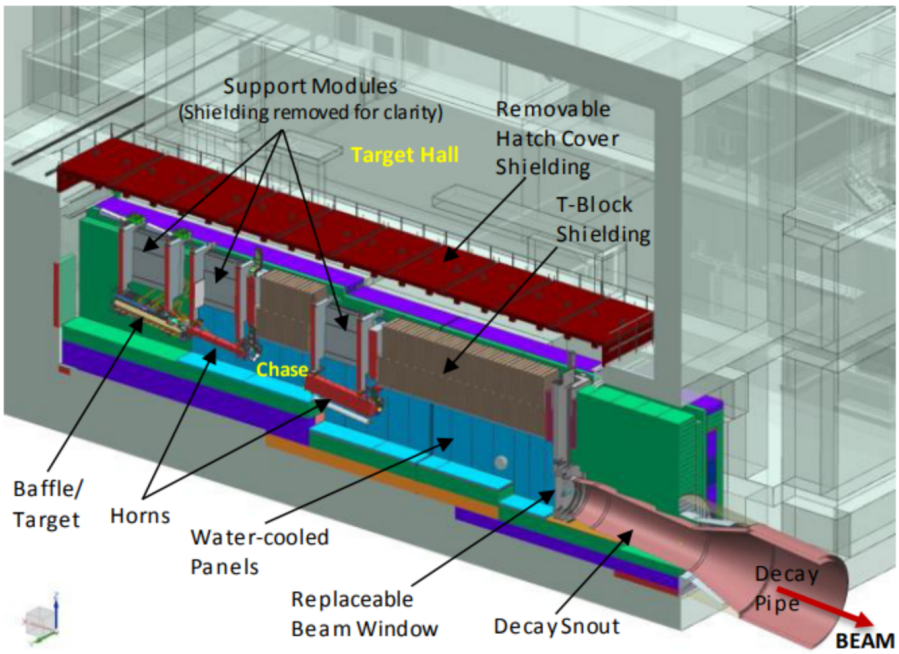

Figure 4.3: Cross section of the LBNF target facility showing the components of the neutrino production design. The initial charged-particle beam is incident upon a nuclear target. The resulting hadronic fluxes are focused by magnetic fields produced by a series of horns. The resulting flux, dominated by pions, is directed to a decay volume. Downstream of this volume is a muon absorber hall (not shown) [*Tariq et al.* (2016)].

acteristics, and the shape of the decay pipe. In addition, the models governing the hadronic interactions within and downstream of the target, including the relative production of pions and kaons, contribute a significant theoretical uncertainty to the exact composition of the beam. Both of these mesons will eventually decay to some combination of neutrinos, but while pions will decay via $\pi^+ \to \mu^+ + \nu_\mu$ with a branching fraction of 0.999877, kaons may produce charged and neutral pions or decay promptly via the semileptonic $K^+ \to e^+ + \nu_e$ as much as 5.07% of each decay. This intrinsic ν_e component significantly complicates any ab initio model of beam flux.

The inclusion of a near detector system in a long-baseline experiment allows for direct measurement of the flux at a short distance from the beam production site, where relatively little oscillation has taken place. From this measurement of the interaction rate of each component of the neutrino flux, and from careful modeling of the ND detector response, a hypothesis of the incident flux is *unfolded*. This flux hypothesis is then propagated to the FD position using an oscillation parameter hypothesis, including matter effects as the beam typically travels through a significantly section of earth, and the resulting *FD event rate prediction* is compared to the observation at the FD.

4.2 Physics Goals of DUNE

DUNE will improve upon the measurements of preceding experiments by improving sensitivity to oscillation parameters, primarily $\sin^2\theta_{23}$, δ_{CP}, and Δm^2_{32}. DUNE will very quickly resolve the hierarchy of neutrino masses at the 5σ confidence level in 1 year of lifetime (assuming δ_{CP} is maximal at $-\frac{\pi}{2}$) and in 2 years of lifetime for all possible values of δ_{CP}. It will achieve a 3σ measurement of δ_{CP} if its value is maximal in 3 years, with a 5σ measurement on its value across 50% of possible values within 10 years of running (Figure 4.2).

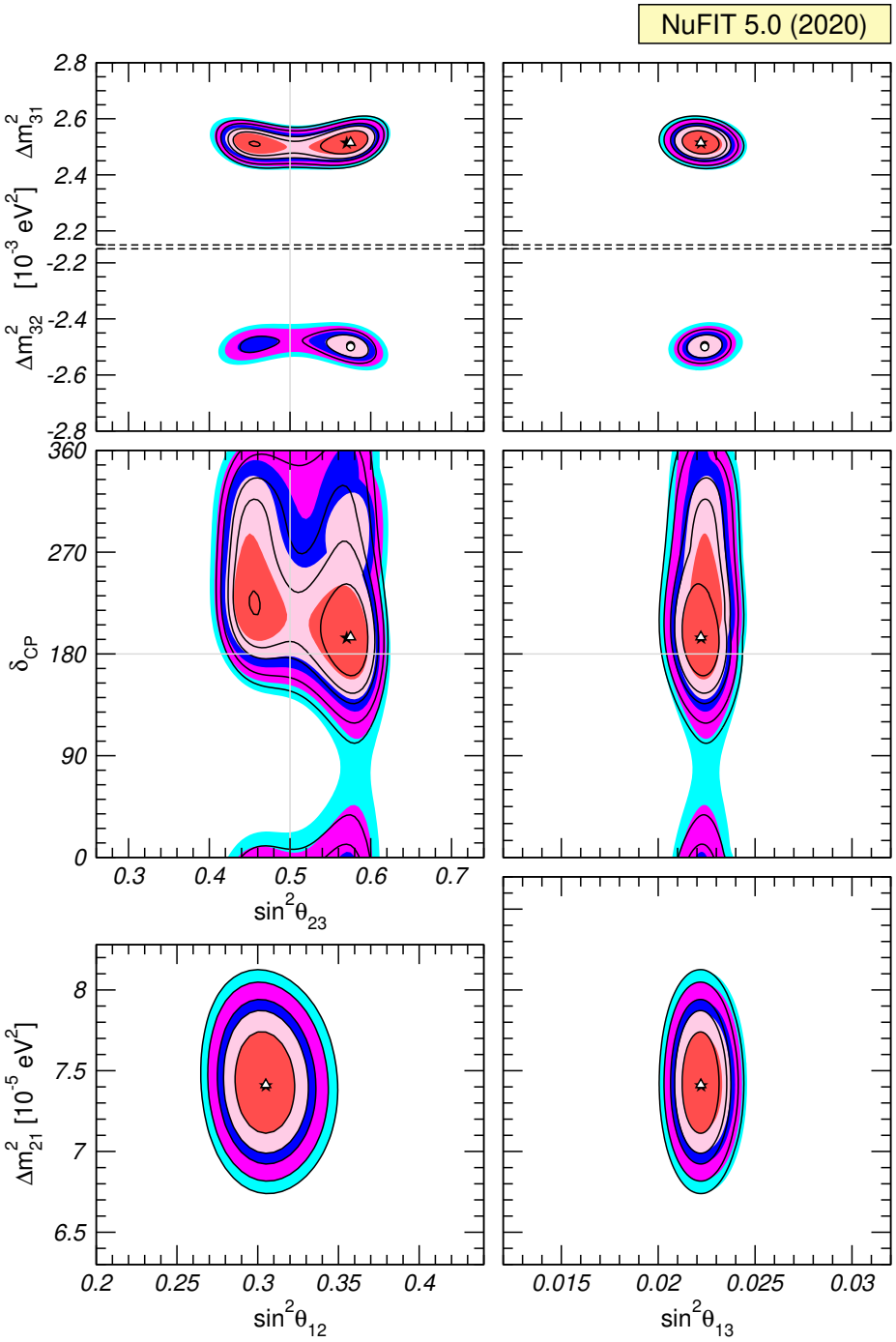

Figure 4.4: Current best-fit values of oscillation parameters using the nuFIT global 3ν oscillation analysis. Each panel shows the two-dimensional projection of the allowed six-dimensional region after marginalization with respect the undisplayed parameters. Colored regions (black contour curves) are obtained without (with) the inclusion of tabulated Super-K atmospheric χ^2 data. [*Esteban et al.* (2020)].

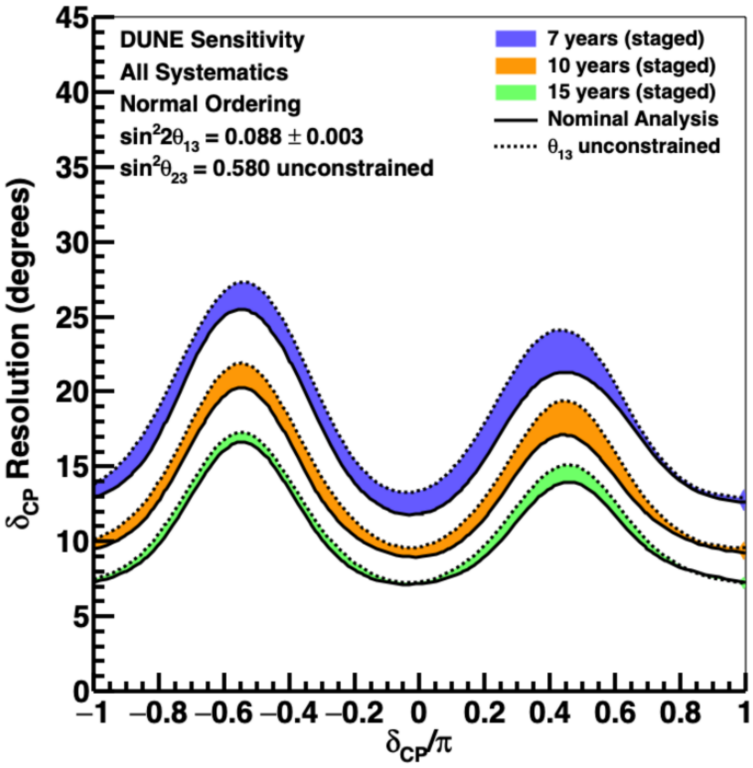

Figure 4.5: Simulated resolution in degrees of the measurement of δ_{CP} using DUNE as a function of the true value of δ_{CP} for seven (blue), ten (orange), and fifteen (green) years of exposure, assuming normal ordering.

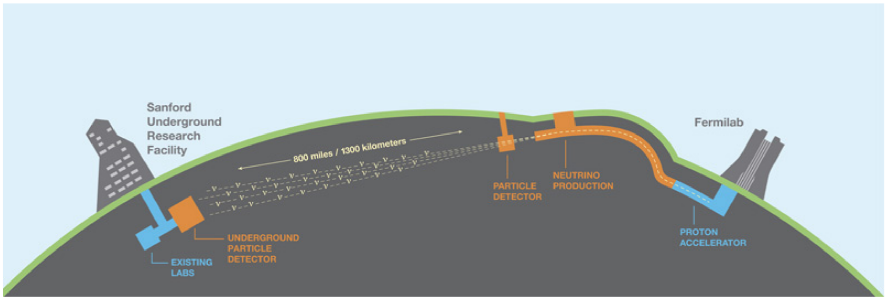

Figure 4.6: Illustration of the overall configuration of the LBNF/DUNE beamline and detectors. The neutrino beam is produced at LBNF in Illinois, immediately traveling through the ND facility and detectors on the FNAL campus and ultimately to the DUNE far detector complex in Lead, South Dakota, 1300 km away [*Abi et al.* (2020a)].

DUNE will feature four monolithic far detectors located at the bottom of the retired mine which once was host to the Homestake experiment. The far detector site is operated by the Sanford Underground Research Facility (SURF) and is also home to the LZ dark matter experiment. These 10 kT detectors will at the time of their commission be the largest TPCs ever built. The design of the FD modules will consist of two horizontal-drift TPC modules, one vertical drift TPC, and one module-of-opportunity whose design is not yet finalized.

DUNE will have a robust near detector system made up of three distinct detectors working together, and a transverse positioning system called DUNE-PRISM to better constrain beam and interaction systematics, as well as to enable unique experimental techniques. These detectors are designed to closely mimic or outperform the response characteristics of the FD units, while accurately reading individual neutrino events in a high-rate environment just 574 m from the beam source.

4.3 Components of DUNE-FD

The DUNE far detectors are hosted deep underground in the Sanford Underground Research Facility (SURF) at the location of the Homestake gold mine underneath

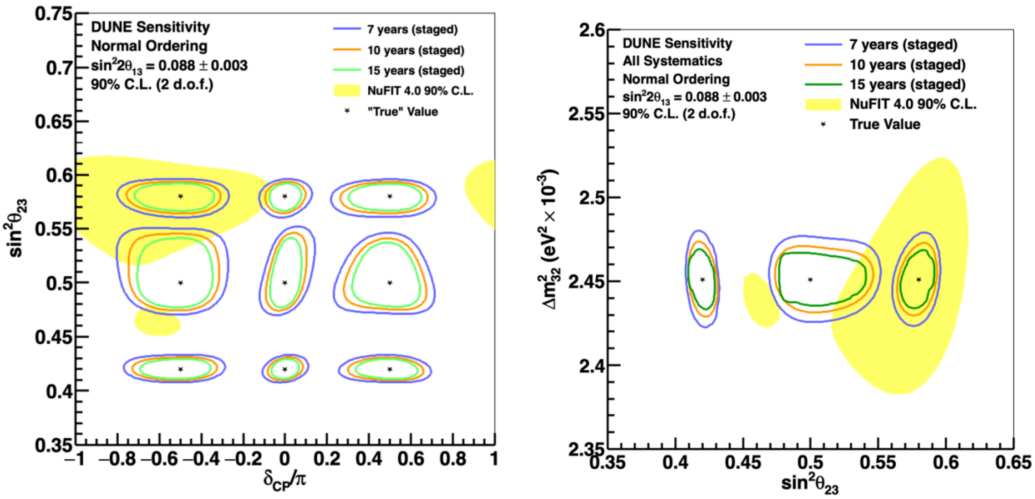

Figure 4.7: 2-dimensional 90% constant $\Delta\chi^2$ confidence intervals in the spaces of $\sin^2\theta_{23} - \delta_{\mathrm{CP}}$ (left) and $\Delta m^2_{32} - \sin^2\theta_{23}$ (right) for different injected "true" parameter values for 7, 10, and 15 simulated years of running time with the DUNE baseline and projected sensitivity. The 90% confidence level region for the NuFIT 4.0 global fit is included in yellow for comparison [*Gonzalez-Garcia et al.* (2021)] [*Abi et al.* (2020b)].

Lead, South Dakota, which once hosted the first experiment to successfully detect neutrinos by Davis and Bahcall. This site is positioned 1300 km from the beam source.

The experimental halls are situated roughly 1500m under the surface of the Earth, offering good protection from the high rate of cosmic rays (165 Hz) for a detector system of this size. At this depth, the relative rate of neutrino events originating from the beam is slightly greater than the rate of events of cosmic ray origin.

4.3.0.1 Horizontal Drift LArTPC

The first two modules will be constructed according to a horizontal-drift design. This design features a large 65.8 m × 18.9 m × 17.8 m outer-dimension cryostat (Figure 4.3.0.1) containing a LArTPC with four distinct drift volumes arranged in an anode-cathode-anode-cathode pattern. Each anode plane is made of 50 anode

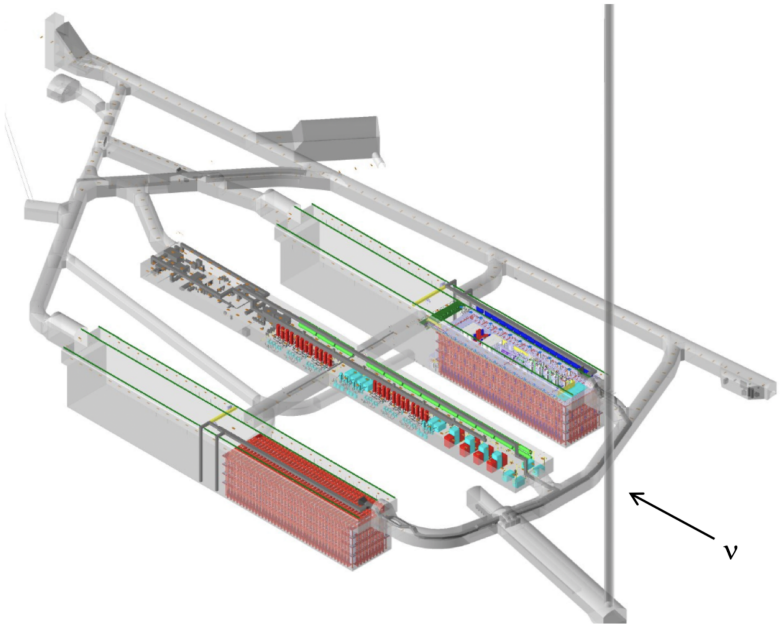

Figure 4.8: Diagram of the DUNE underground caverns at the far detector site at SURF in South Dakota. The two experimental halls which host the four far detector modules are supported by a central utility cavern (CUC) for slow-control and ancillary systems. The Ross Shaft is the main access tunnel to the DUNE area and it appears on the right [*Abi et al.* (2020a)].

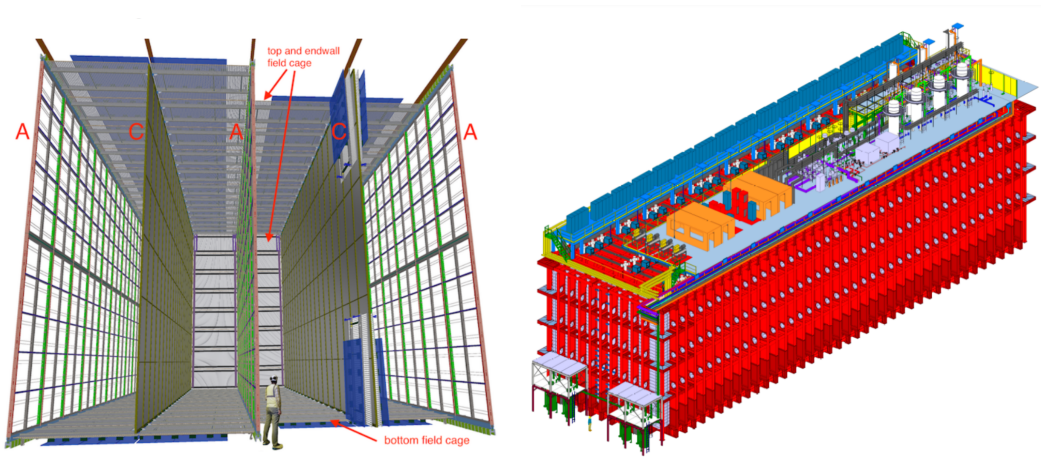

Figure 4.9: A cutaway schematic view of the DUNE Horizontal Drift (HD) TPC (left) and the external view of the full cryostat which houses a single 10 kT far detector module (right).

plane assemblies (APAs) arranged in 2 rows of 25, which hang vertically from the top structure. The APAs contain four distinct sets of wrapped wires: a collection plane (X), two induction planes (U and V), and a shielding *grid* plane (G), to reduce the impact of far-field induction. The wire plane arrangement is shown in Figure 4.3.0.1, such that the collection and grid plane wires run vertically, while the induction planes are wrapped at an angle of 35.7° to the vertical. The spacing between adjacent wires (wire pitch) is 4.79 mm.

The horizontal drift FD will feature a maximum drift length of 3 m and make continuous measurements of the voltage on each wire at a rate of 2 MHz.

4.3.0.2 Vertical Drift LArTPC

One of the DUNE FD modules will feature a vertical drift (VD) TPC, which differs from the HD design in a number of ways. Most notably, the anode plane of this module will be use etched PCB material instead of stretched wires, shown in Figure 4.3.0.2. The VD design also features a single cathode running along the middle horizontal plane, with a vertical drift field. The maximum drift distance under this

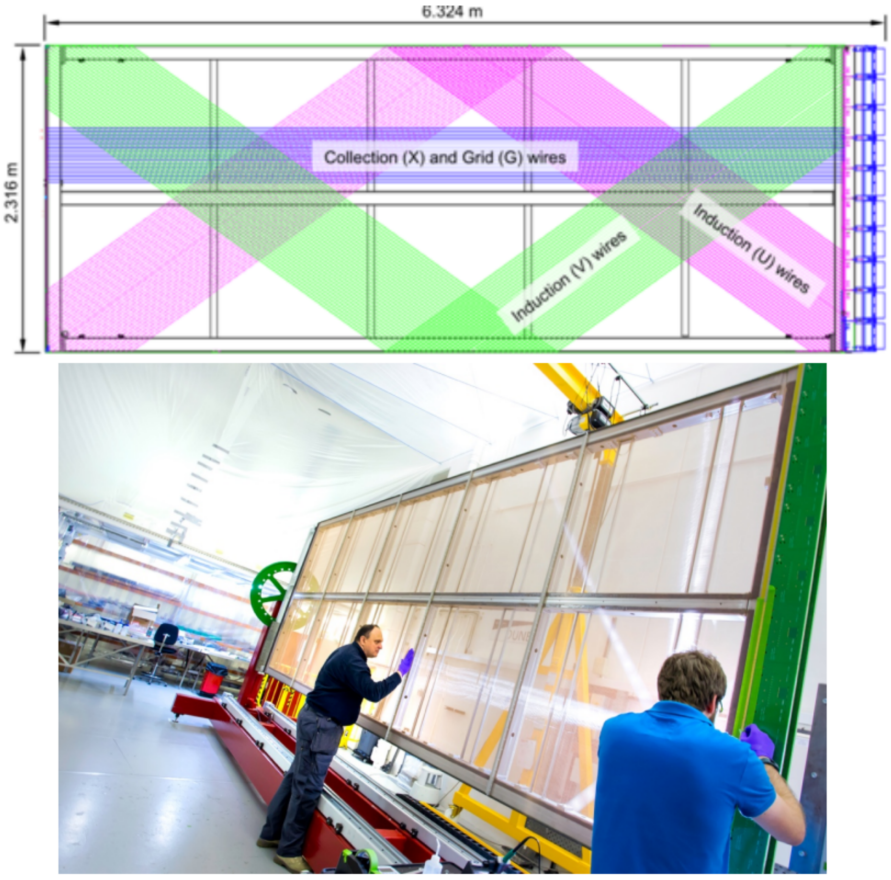

Figure 4.10: A schematic of the APA, shown here on its side (top). The collection (X) and grid (G) planes are aligned with the vertical axis, while the two induction planes (U and V) are wrapped at an angle of 35.7° with respect to the X plane. The support structure from which the planes hang can be seen on the right side of the assembly. An APA in a wire-winding machine (bottom) is being prepared for mounting with the ProtoDUNE-SP prototype TPC at CERN.

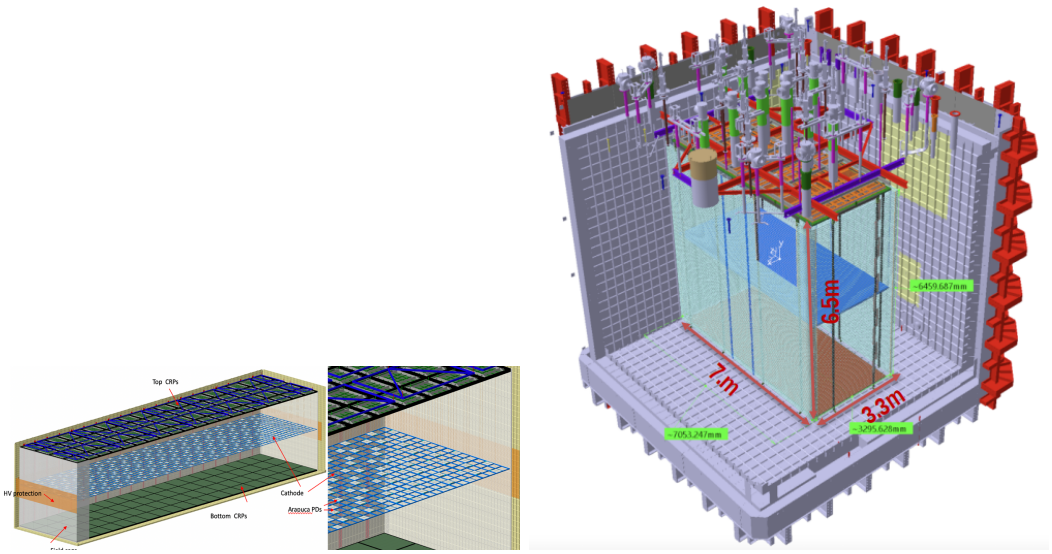

Figure 4.11: A cutaway schematic view of the DUNE Vertical Drift (VD) modular detector (left). A cutaway view showing the modular construction of the VD detector with two TPC subassemblies inside of a DUNE FD cryostat structure (right).

design will be longer than the HD modules, with a drift distance of 6 m.

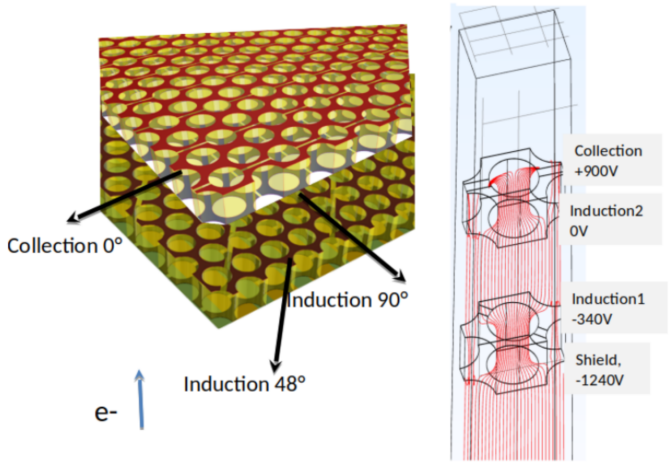

Figure 4.12: A closeup view of the DUNE VD far detector anode plane, which is composed of etched PCB with collection, induction and shield planes attached to two large perforated planes. On the right is a numerical simulation of the drift paths of charges in a column near the anode plane.

CHAPTER V

DUNE-PRISM

In a typical long-baseline neutrino oscillation experiment, an observation of a neutrino flux interacting with an instrumented target is compared to a a model prediction of that flux, under various oscillation hypotheses. This method requires very accurate modeling of the neutrino beam, the interaction of that beam with the matter upstream (dirt interactions) and with the target itself, and lastly (and of objective interest to oscillation experimentalists) the oscillation model. The details of the first two models – the beam production and the neutrino interaction cross-section – are often treated as nuisance parameters. While these parameters are not the primary target of such analyses, these models are of great importance to both the oscillation analysis (these model uncertainties contribute greatly to the overall uncertainty on the measurement of oscillation parameters) and to the broader community of nuclear and particle physics.

The need for a stronger constraint on these parameters has lead to the proposal of the Precision Reaction-Independent Spectrum Measurement (PRISM) program. This technique uses a near detector which moves through the direction transverse to the neutrino beam, allowing us to probe another dimension of the kinematic space which defines the flux. This technique can be leveraged to construct oscillation analysis which can minimize the contribution of interaction uncertainties in the measurement

of oscillation parameters or to directly measure aspects of the neutrino interaction model which are inaccessible to a normal, fixed-position detector.

5.1 Neutrino Production and the Off-Axis Flux Dependence

Neutrinos, being electrically neutral, are not well suited to direct acceleration. Instead, a proton beam is accelerated using existing beamlines (in the case of DUNE and NOνA, this is done up to and including the main injector ring at FNAL). The high-energy proton beam is then directed to a graphite target, resulting in a mess of hadronic products. These products are directed through a series of magnetic focusing horns, tuned to refocus the charged pion component. Positive or negative pions are selected by the switching polarity of the current, using forward horn current (FHC) or reverse horn current (RHC) respectively. The refocused charged pion beam then travels down a length of pipe where they are allowed to decay into their preferred products (branching ratio 99%): anti-muons/muons and their partner neutrinos/anti-neutrinos. The efficiency of the focusing elements to select only pions is not perfect, and some fraction of the beam will be composed of kaons, which are of similar charge-to-mass ratio. These particles are not as constrained in their decay as pions, and contribute to the intrinsic ν_e component of the beam.

The resulting beam, being the product of many interaction and decay processes after the initial proton beam phase, is relatively broad in both its energy and angular spectrum.

5.2 DUNE-PRISM and the ND Hall Complex

The DUNE near detector hall complex houses the three main near detector components: ND-LAr, a liquid argon TPC meant to closely match the far detector in its response to the neutrino flux; ND-GAr, a gaseous argon TPC in a magnetic field,

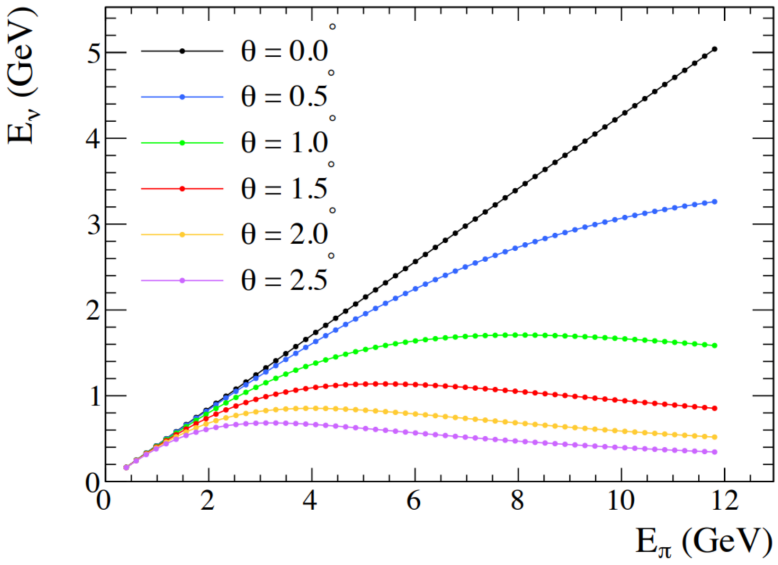

Figure 5.1: The energy of the daughter neutrino produced by pion decay as a function of the decay angle in the laboratory frame with energy corresponding to LBNF [*Duffy* (2017)].

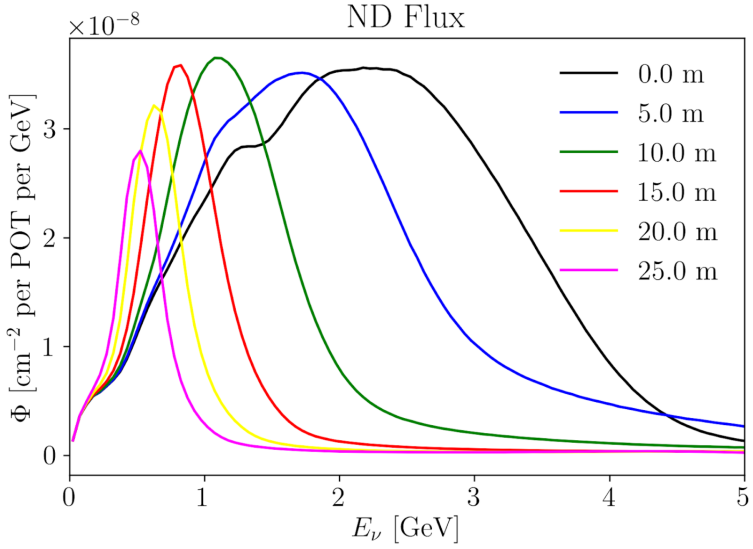

Figure 5.2: The LBNE ν_μ flux at the distance of the ND experiment hall at various off-axis distances. As the distance from on-axis increases, the average energy becomes lower and the width of the spectrum decreases, in accordance with the decay relationship shown in Figure 5.1.

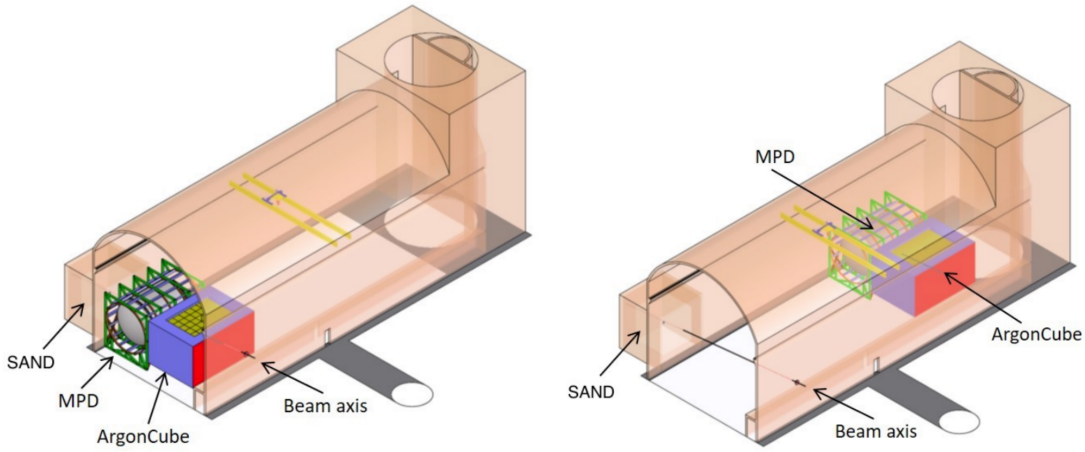

Figure 5.3: The Near Detector experimental hall showing the three subsystems of the DUNE near detector. The two upstream components, ArgonCube (LArTPC) and MPD (Gaseous Argon TPC) are designed to move transversely to the axis of the neutrino beam, allowing them to sample far off-axis fluxes.

designed for high-precision sign selection and calorimetry of muons which do not stop in the upstream ND-LAr; and SAND, which is a plastic scintillator-based beam monitoring device containing a central liquid argon target. Of these three detectors, the two upstream components, ND-LAr and ND-GAr, will be mounted on a set of Hilman rollers [hil], allowing them to move between 0 and 30.5 m relative to the beam's central axis.

5.3 The Linear Combination Analysis

A simple long-baseline oscillation analysis intends to measure $P_{\nu_\alpha \to \nu_\beta}(E_\nu)$, the probability for a neutrino of flavor α (either e, μ, or τ) to oscillate into one of flavor β. A detector observes only the rate of interaction from which flux must be inferred. This rate is proportional to the incident flux at the detector position and the cross section of the neutrino (each flavor having its own probability and its own flux).

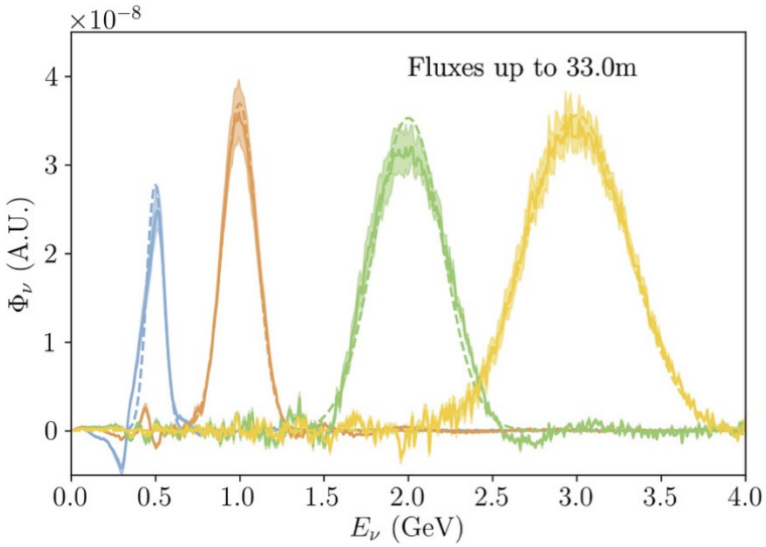

Figure 5.4: Demonstration of the flux matching technique using arbitrary (gaussian) target shapes at different mean energy locations, with a 10% width [*Abud et al.* (2021)].

Furthermore, the observation of such a detector is in terms of *reconstructed* variables, inferred from deposited energies and subject to the operating principles of the device. These various effects, including sensitivity, effective area and mass, and efficiency of identification and reconstruction, is represented by a detector response matrix, which is determined by detailed modeling. Including all of these effects, comparing the interaction rate between a near and far detector for a particular oscillation channel (the oscillation of ν_μ to ν_e) can be represent using the expression in Equation 5.1.

$$\frac{\frac{\mathrm{d}N^{\mathrm{far}}_{\nu_\mu}}{\mathrm{d}E_{\mathrm{rec}}}}{\frac{\mathrm{d}N^{\mathrm{near}}_{\nu_\mu}}{\mathrm{d}E_{\mathrm{rec}}}} = \frac{\int P_{\nu_\mu \to \nu_e}(E_\nu)\Phi^{\mathrm{far}}_{\nu_\mu}(E_\nu)\sigma^{\mathrm{Ar}}_{\nu_\mu}(E_\nu)T^{\mathrm{far}}_{\nu_\mu}(E_\nu, E_{\mathrm{rec}})\,\mathrm{d}E_\nu}{\int \Phi^{\mathrm{near}}_{\nu_\mu}(E_\nu)\sigma^{\mathrm{Ar}}_{\nu_\mu}(E_\nu)T^{\mathrm{near}}_{\nu_\mu}(E_\nu, E_{\mathrm{rec}})\,\mathrm{d}E_\nu} \tag{5.1}$$

From this expression, it is clear that extracting the oscillation probability component alone is not trivial. The typical process involves precise characterization of the detector response and "unfolding" the rate of neutrino interaction in terms of true kinematic variables. If the near and far detector are very similar in terms of interaction probability (specifically, the nuclear targets and their cross sections), then

oscillated and unoscillated fluxes can be compared directly. If different detection media are used, this is another effect which must be unfolded before flux comparisons can be made.

In the PRISM paradigm, we assume similar detector technologies for near and far detectors. Then using a detector design which enables the sampling of flux at multiple off-axis positions, we can build a "composite" flux from a linear combination of these components. This linear combination is chosen to match the FD oscillated flux inside of some region of observable phase space. By tuning this linear combination to various oscillation hypotheses and comparing the corresponding ND rate to the observe FD rate, a near-to-far comparison can be made directly in terms of the observed quantities, avoiding the unfolding process and sidestepping many of the accompanying systematic uncertainties.

Mathematically, finding a set of coefficients for which the ND composite flux matches an FD oscillated flux under some oscillation hypothesis is an under-determined problem. To better constrain the set of allowed coefficients, Tikhonov regularization is used.

$$\vec{c} = \left[N^T P N + \Gamma^T \Gamma\right]^{-1} N^T P \vec{F} \tag{5.2}$$

In Equation 5.2 a coefficient vector $\vec{c}$ is obtained from a matrix N representing the unoscillated flux at the near detector (with rows representing the neutrino energy and columns representing the off-axis position) and a vector $\vec{F}$ representing the far detector flux (with only rows representing the neutrino energy). In addition matrices P and Γ represent a pseudo-covariance and regularization penalty matrix, respectively. The covariance matrix serves as a tool to tune the flux-matching in energy space, while the Γ matrix penalizes coefficients which, in the case of PRISM, are highly-varying from off-axis position to off-axis position.

The DUNE neutrino beam spectrum at the ND site as a function of energy and

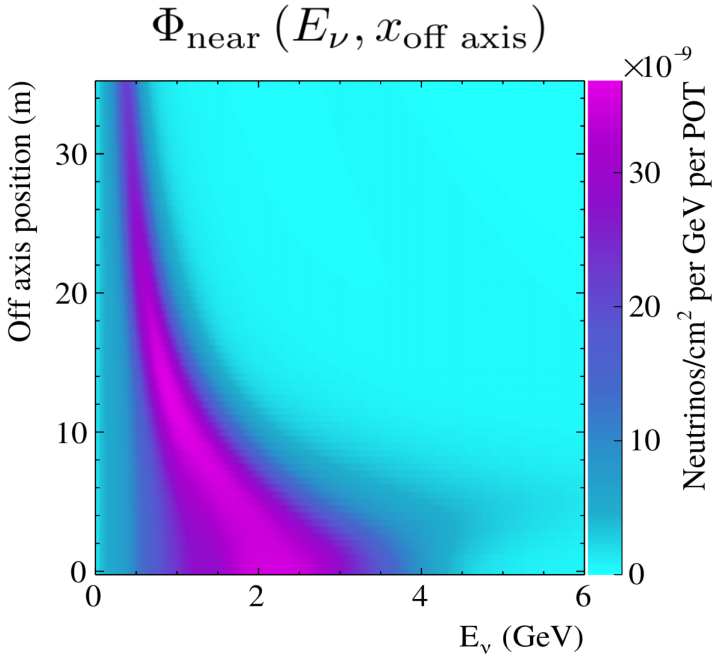

Figure 5.5: The DUNE near detector ν_μ flux as a function of true neutrino energy and off-axis position. In the PRISM flux-matching method, this model is represented as a matrix and used as an input to the coefficient-solving algorithm.

off-axis position is shown in Figure 5.3.

Using a nominal oscillation hypothesis, such as the T2K best fit measurement, we can demonstrate the ability of the method described above to produce a composite ND flux which closely matches the oscillated DUNE FD ν_μ appearance flux, shown in Figure 5.3.

The ND neutrino spectrum is a function of not only the energy and off-axis angle, but also many details of the beam production. Practically, the current in the final magnetic focusing horn is of great importance to the shape of the ND ν_μ spectrum. Such beam-PRISM augmentations have been proposed, and the DUNE collaboration has adopted a special horn current run plan with the ND system in the on-axis position for 1 week of the year. The relative shape of this special 280 kA run (the nominal

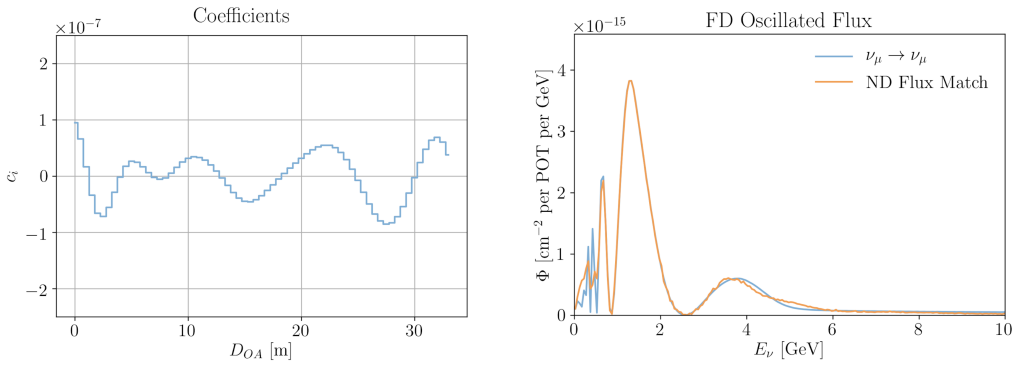

Figure 5.6: Coefficients found using Tikhonov regularization with an L1-norm penalty matrix (left). The resulting coefficients have a low absolute value, and are smoothly-varying as a function of off-axis position. An example of an oscillated $\nu_\mu \rightarrow \nu_\mu$ flux at the DUNE far detector with a corresponding flux-matched ND linear combination (right). This composite flux is formed using the coefficients shown in the left figure. The flux matching is tuned to minimize the difference between these two shapes between 0.5 GeV and 4 GeV.

horn current is 293 kA) can be seen in Figure 5.3, with several off-axis relative fluxes shown for reference.

A flux match including this additional degree of freedom is shown in Figure 5.3.

In the context of an oscillation analysis, this linear combination method is trained on and applied to event rates instead of fluxes. At the time of these studies, robust detector simulation was not available, so flux models are shown instead.

The oscillation analysis is built from a set of coefficients trained to a range of oscillation parameters. Figures 5.3 and 5.3 demonstrate the ability for this algorithm to perform accurately over a range of oscillation parameter space which is consistent with the findings of previous experiments. In analysis, the pre-trained coefficients are used as a proxy for a given oscillation parameter hypothesis, and the ND composite rate observation (in a given observable variable) is compared to the observed FD rate distribution, in that observable space. In this way, the "unfolding" technique which requires extremely accurate modeling of detector responses is avoided altogether.

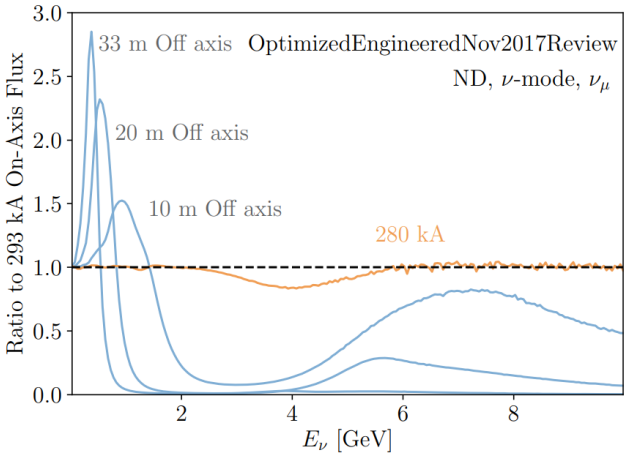

Figure 5.7: The ratio of the nominal on-axis flux is shown for three off-axis positions, and for on-axis running where the nominal 293 kA horn current has been lowered to 280 kA. The modified horn current provides an additional constraint just above the first oscillation maximum, with no effect at the lower energies sampled by the off-axis fluxes. This ratio serves as a rough illustration of the relative fitting abilities each additional flux adds to the space of shapes accessible to the fitting method [*Abud et al.* (2021)].

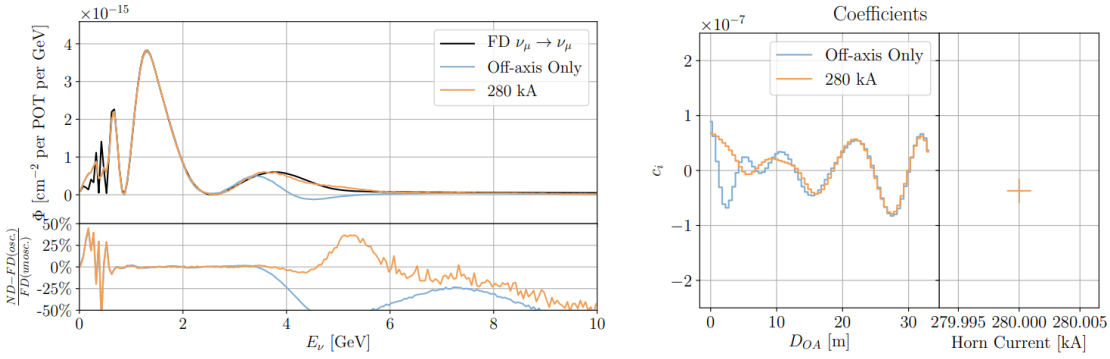

Figure 5.8: The FD flux and the ND linear combination flux match (left) and corresponding coefficients (right) are shown utilizing an additional horn current flux. The inclusion of the additional flux improves the quality of the fit in the highest-energy oscillation minimum region, between 3-5 GeV, consistent with what is shown in Figure 5.3 [*Abud et al.* (2021)].

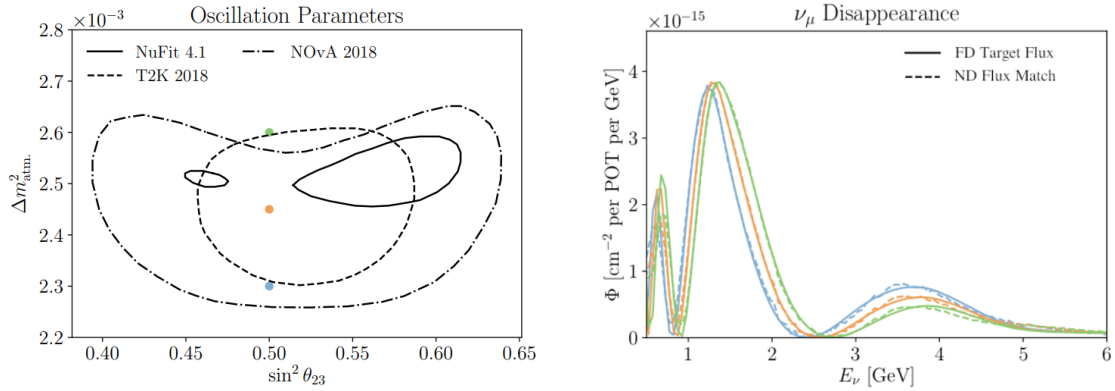

Figure 5.9: FD predicted muon neutrino spectra under a variety of oscillation hypotheses. Left: current best results for muon neutrino disappearance parameters, colors showing chosen oscillation hypotheses. Right: solid lines corresponding to the FD oscillated flux predictions in color coordination with points on the let plot. The dashed lines are the best match spectra for oscillated FD fluxes constructed from linear combinations of ND fluxes (33 m off-axis + 280 kA special horn current run) [*Abud et al.* (2021)].

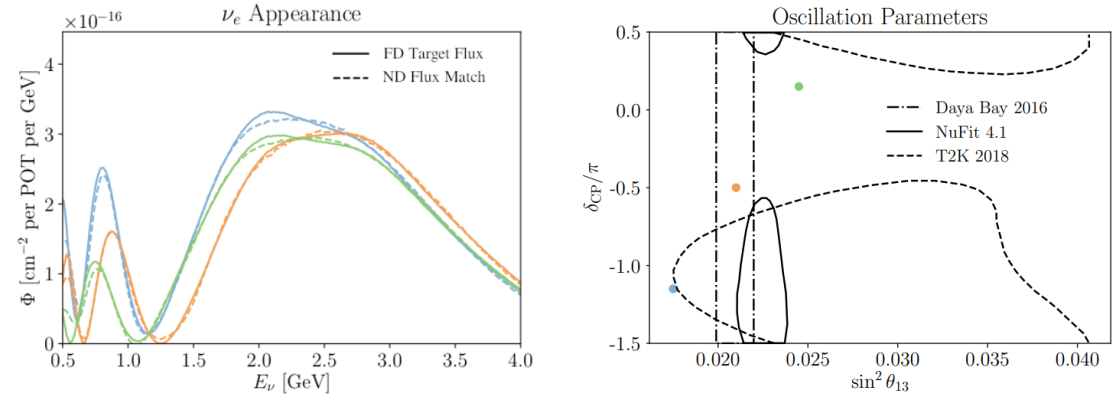

Figure 5.10: The flux matching of the ND ν_μ flux to the oscillated FD ν_e flux (left) is shown assuming various sets of oscillation parameters (right). Target fluxes are shown with solid lines and resulting fits are shown in dashed lines [*Abud et al.* (2021)].

Monte Carlo simulations of hadron production systematic variations can be used to demonstrate the error-suppressive effect of this analysis technique on near-to-far extrapolations. Figure 5.3 shows the double-difference between a combined flux under a systematic variation in hadron production model and the nominal counterpart to the FD flux difference under the same hadron production shift. The differences shown are less than 2% within the energy region of flux matching, for a range of oscillation parameters in $\Delta m^2_{\text{atm.}} - \sin^2\theta_{23}$ space.

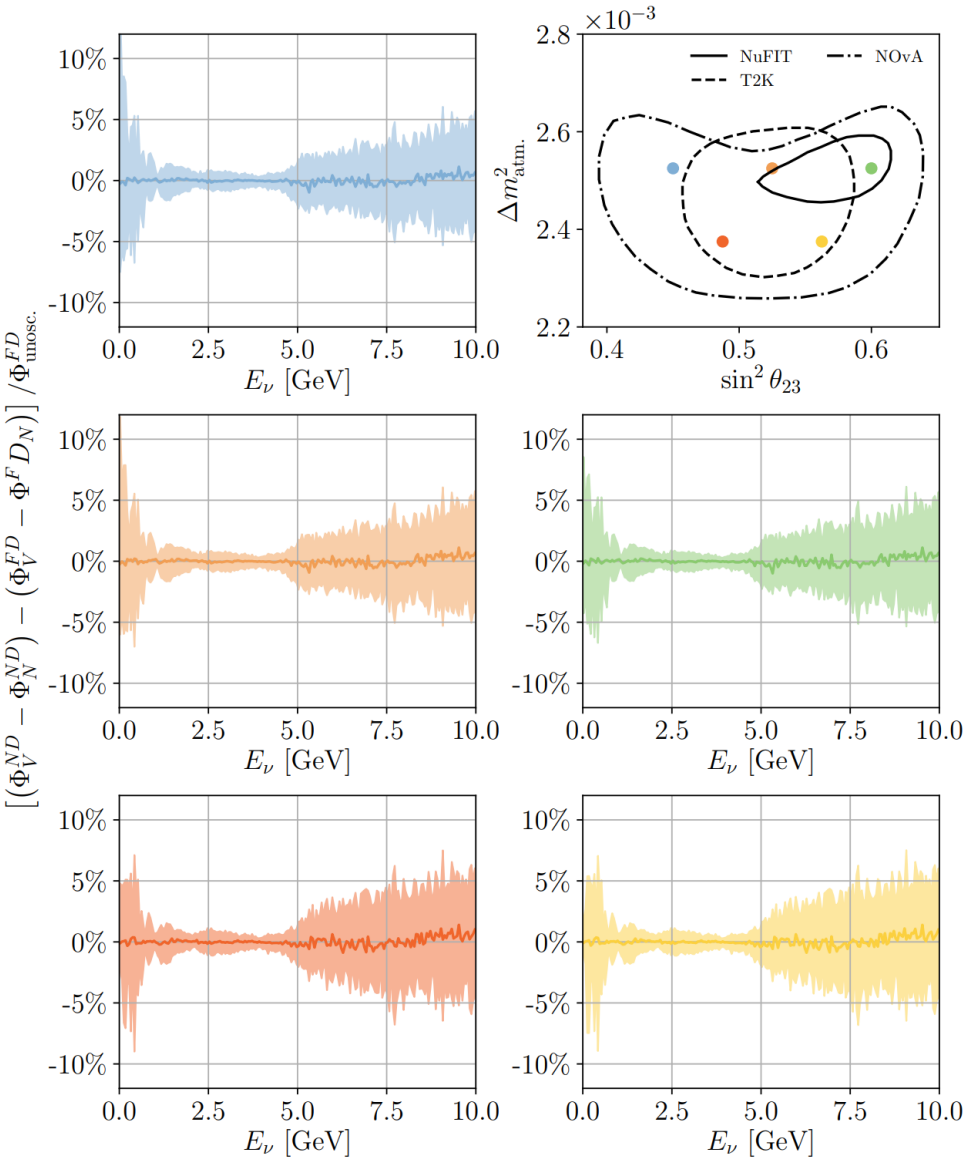

Figure 5.11: Cancellation of hadron production systematic variations assuming various oscillation hypotheses (top right). Shown are median values (solid line) and 60% containment intervals (bands). The figure colors correspond to the oscillation hypothesis points on the upper right panel [*Abud et al.* (2021)].

CHAPTER VI

The DUNE Near Detector

The near detector program for DUNE consists of a set of three distinct detectors working together in a single experimental hall 574 meters from the neutrino production facility (LBNF) [*Abud et al.* (2021)].

The three components of the near detector system are a segmented liquid argon time projection chamber (ND-LAr, also organized under the name *ArgonCube*), a magnetized, monolithic gaseous argon time projection chamber (ND-GAr), and an on-axis scintillator-based beam monitor (System for On-Axis Neutrino Detection, SAND). Together, these systems will provide a superb measurement of the unoscillated neutrino flux from the LBNF beam, have the ability to study neutrino-nucleon interaction mechanics with novel techniques enabled by the PRISM system, and vitally contribute to the measurement of oscillation parameters by the DUNE far detector systems.

6.1 Goals of the Near Detector Program

The overarching goals of the near detector program are as follows:

- To make precision measurement of the neutrino flux produced by LBNF in a way that is transferable to the DUNE far detectors. Since the DUNE far

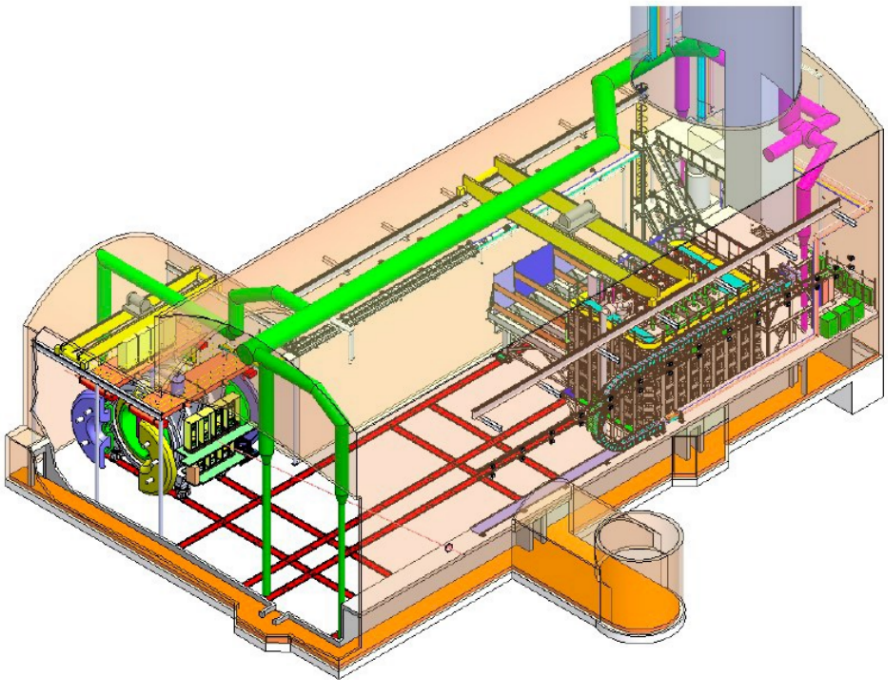

Figure 6.1: Diagram of the DUNE near detector hall. In this view, the LBNF neutrino beam enters from the lower-right side on a slight downwards (6°) angle. The image shows the ND-LAr and TMS elements in their farthest off-axis position, having moved via the PRISM system, with the on-axis SAND detector in its alcove directly on the beam axis.

detectors are primarily LArTPCs, the ND systems must utilize an argon target using similar LArTPC technology.

- To sufficiently constrain neutrino interaction models – including both neutrino-nucleon interaction models and detector models – to improve the analysis methods used by the DUNE FD.

- To verify and improve ab initio models of LBNF beam simulations, which are highly dependent upon systematics such as particle productions in the target, beam optics, etc. These simulated flux profiles must be constrained for all flavor components and modes of beam operation.

- To verify the consistency of beam production details as a function of time; the ND systems must be able to rapidly identify and measure shifts in beam production.

6.1.1 PRISM

The PRISM system, described in more detail in Chapter V, utilizes a system of Hilman rollers to allow for the motion of the two upstream detectors (ND-LAr and ND-GAr) through approximately 30.5 m in the direction transverse to the LBNF beam. This allows for the sampling of neutrino fluxes from different regions of the pion decay angular spectrum. This view, combined with the excellent energy resolution allowed by the LArTPC technology, allows for very detailed analysis of the neutrino beam production systematics and native measurement of double-differential neutrino production cross sections.

In addition to the improved view of neutrino production kinematics, the angular dependence of the neutrino energy spectrum allows for novel analysis techniques which can reduce the impact of neutrino-nucleus interaction modeling on the measurement of oscillation parameters. See Section 5.3 for a more complete discussion of the linear

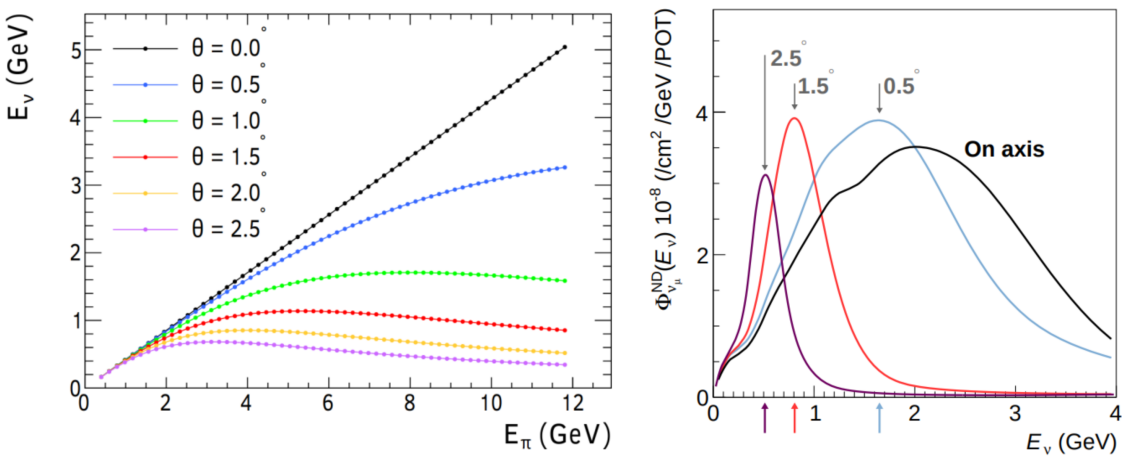

Figure 6.2: The observed neutrino energy in the lab frame from the in-flight decay of a pion as a function of the pion's energy and the angle with respect to the pion's momentum (left). The predicted DUNE beam ν_μ flux at the ND site as a function of the off-axis angle (right). The arrows indicate the peak ν_μ energy for the three off-axis positions shown.

combination analysis.

6.1.2 Oscillation Analysis

6.1.3 Interaction Physics

6.2 ND-LAr: The ArgonCube Detector

The principal component of the DUNE near detector suite is the ArgonCube experiment, or ND-LAr. It is a modular LArTPC featuring pixelated anode planes, low-profile field shaping elements, and a highly responsive light readout system. ND-LAr is the primary target of the ND detectors and is designed to closely mimic the detection methods of the FD LArTPCs, but due to its relative closeness to the beam source and lack of overburden to shield from cosmic ray-induced events, it is required to outperform the DUNE FD modules in several aspects. This is achieved by employing several novel techniques, which are discussed below:

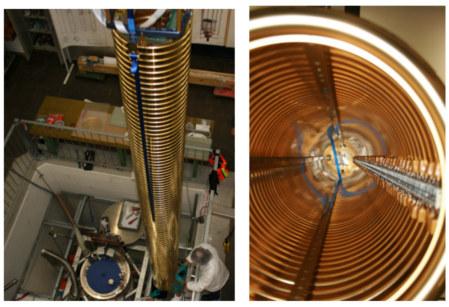

Figure 6.3: Photograph of the ARGONTUBE TPC with 125 field shaping rings (left). The view from inside of the TPC, showing the high-voltage generator on the right side (right).

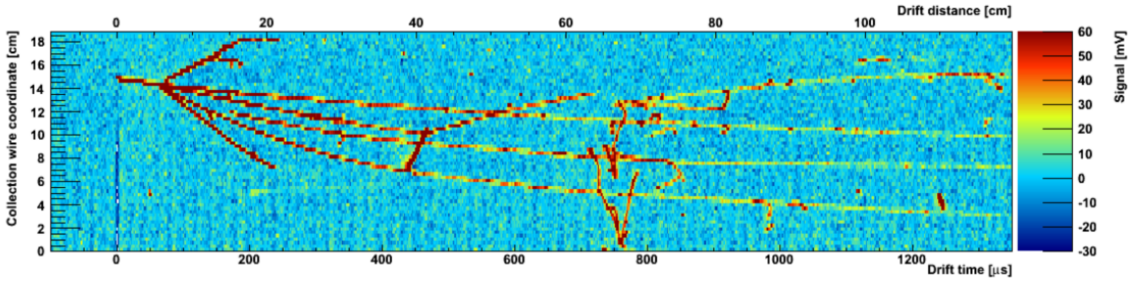

Figure 6.4: Collection view of a cosmic particle interacting with a nucleus in ARGONTUBE with at least 6 secondary particles.

6.3 Prototypes and Component Technologies

The development of the ArgonCube detector began with the design and operation of the ARGONTUBE experiment, a 5m long drift LArTPC operated at AEC-LHEP, University of Bern [*Ereditato et al.* (2013)].

This detector served as a demonstration of the ability to achieve high purity of LAr required for long-drift TPCs. This detector and the associated LAr purification system demonstrated a charge lifetime of $2.05 \pm 0.08\,\mu$s.

This is considered to be the predecessor to the ArgonCube program, a planned LArTPC near detector for DUNE. The ArgonCube detector utilizes a number of techniques which make it unique among LArTPCs, including a modular design, a

low-profile field cage, or *field shell*; and a printed circuit board (PCB) anode plane featuring a pixelated charge collection system for native 2D projective charge measurement and modular attachment of SiPM-interfaced light readout systems.

6.3.1 Modularization

ND-LAr is designed in a modular fashion. The detector consists of an array of 1 m $\times$ 1 m $\times$ 3 m modules arranged in a grid of 5 modules by 7 modules. There are many advantages of using many small TPCs instead of a single, monolithic volume:

- A short drift distance decreases the need for ultra-high purity
- Shorter drift distance decreases the steady-state concentration of Ar^+ ions within the volume (see *space charge effect*, Chapter III.).
- Smaller TPC volume improves optical segmentation, allowing for better spatial resolution of light systems and more granular triggering in a high-rate environment.
- High-density charge readout planes and closely-packed modules improves reconstruction of multi-module tracks and mitigates risks due to individual electronics failures.
- Despite independent charge and light collection systems, modules share a single cryostat and LAr purification, High-voltage, and other slow-control systems.

6.3.2 Field Shell

The ArgonCube shaping devices are designed to be a low-profile laminate of a uniformly-resistive sheet material attached to the structural elements of the TPC. The initial design utilized a highly-resistive carbon-loaded Kapton® (DuPont DR8 polyimide) laminated to 1/8"-thick G10 module support structures. The kapton

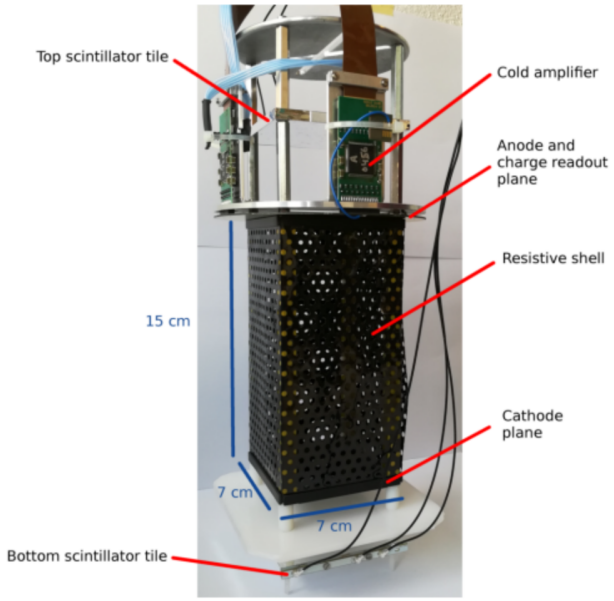

Figure 6.5: Prototype TPC demonstrating the resistive field shell concept. The resistive shell is perforated to allow for LAr to be circulated, and provides a smooth potential gradient along the drift direction. The cathode plane is attached to a metalized hoop at the bottom of the TPC and is also composed of a uniformly resistive polymer material.

material provides a resistance on the order of 10^{10} G$\Omega/\square$, allowing for a smooth voltage gradient along the direction of the drift field with little power dissipation and heating due to conduction [*Berner et al.* (2019)]. The cathode itself is also a resistive material, though it can be less resistive because of the lower expected current through that plane. The cathode is manufactured from a 1/8" copper-clad G10 board, with copper removed except for a metalized ring around the edge for contacting the cathode film, the field shaping side elements, and the HV feedthrough "pill".

6.3.3 Light Detection Systems

DUNE ND-LAr features two distinct light detection technologies which make up the Light Readout System (LRS): ArCLight and the Light Collection Module (LCM). These modules work together to provide fast timing information from prompt scin-

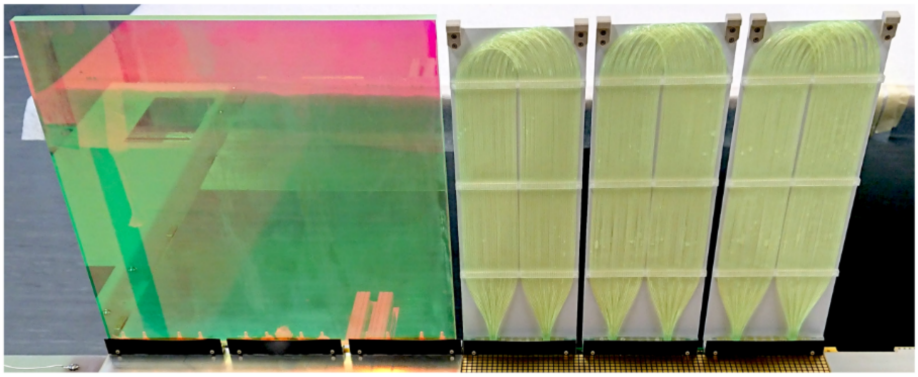

Figure 6.6: A photograph of an ArCLight tile (left) and three LCM tiles (right).

tillation photons (Figure 3.3) from an ionization event within a given module. The quickly arriving light signals ($\mathcal{O}$(10ns)) provide an excellent t_0 for a charge signal and improve rejection of unassociated tracks to mitigate pileup.

Each of the 70 anode planes hosts 30 LCM and 10 ArCLight modules in an alternating pattern of 3 LCM - 1 ArCLight. These planes are arranged along the inside of the field cage at a 90 degree angle to the anode plane. Each LCM panel is 1/3 the size of an ArCLight panel, so that the total surface area is shared equally between the two technologies. The LCM and ArCLight panels share the same basic principle: the scintillation vacuum ultraviolet (VUV) 128 nm light produced by the ionization of the LAr is shifted by a Wavelength Shifter (WLS) to the visible range. In both systems, Tetra-Phenyl-Butadiene (TPB) coats the surface of the panel and is used as a WLS. The resulting shifted light has a broad spectrum peaked around 425 nm.

The ArCLight (Figure 6.3.3, left) was developed by the University of Bern, and utilizes a dichroic film (the ARAPUCA principle [*Souza* (2021)]) to trap light and guide it to six SiPMs mounted on the periphery of each LArPix tile.

The LCM tiles (Figure 6.3.3, right) similarly guide WLS light towards the anode-mounted SiPMs, but do so via total internal refraction within a set of Kururay Y-11 fibers, bundled together to interface to each of the two SiPMs on the anode end, with

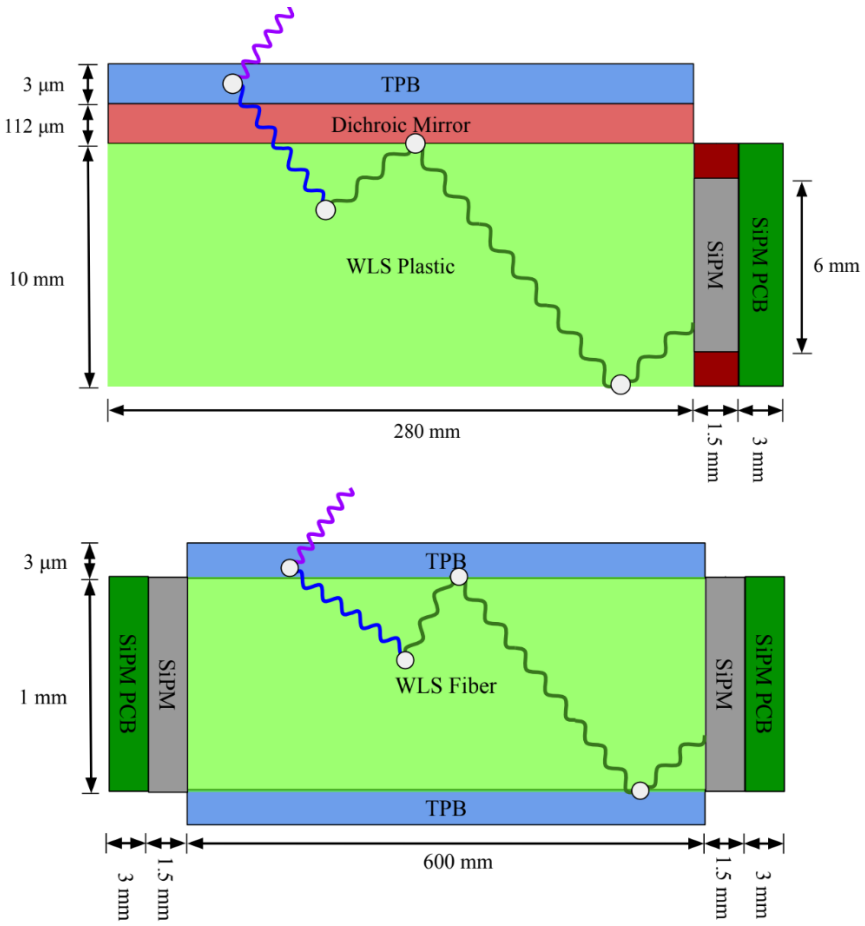

Figure 6.7: The detection principle behind the two light readout system modules. ArCLight (top) is a monolithic light guide mounted to a silicon photomultiplier (SiPM) while the LCM modules are comprised of a series of wavelength-shifting (WLS) fibers, interfaced on both sides to a SiPM.

a 50 mm radius bend on the cathode-facing end.

6.3.4 LArPix

DUNE ND-LAr also features a pixelated anode charge measurement system, called LArPix. This technology allows for native 3D imaging without the need for additional induction planes and the accompanying de-convolution transformations as in the case of a traditional wire-plane TPC.

The LArPix tile features a set of 10,240 independently-triggerable pixels (or tiles)

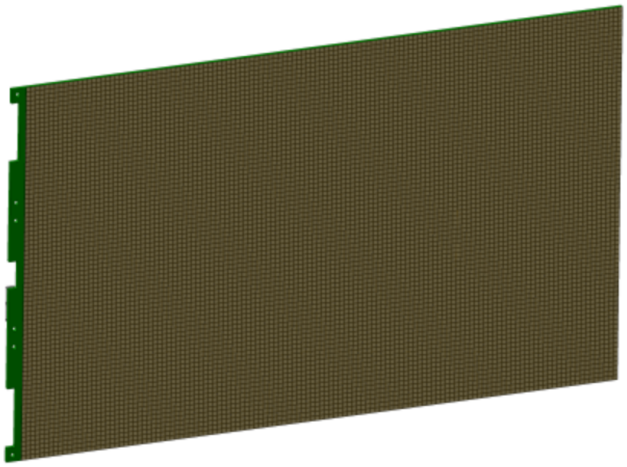

Figure 6.8: A single full-sized LArPix pixel anode tile with 10,240 self-triggering charge-sensitive pixels. Each ND-LAr TPC anode contains 20 identical tiles arranged in two columns.

with configurable thresholds and low quiescent power consumption. Tiles feature a charge-sensitive amplifier which, when a certain amount of charge is collected, will trigger a collection period followed by digitization and flushing of the collected charge. The result is a "hit packet" containing the total digitized charge and timestamp at the time of digitization. These hit packets are fed through a network of controller chips and on to the dedicated PACMAN Data Acquisition (DAQ) system for offline recording for later analysis [*Dwyer et al.* (2018)].

6.4 2 × 2 and Single Modules

The first demonstration of the ArgonCube technique is to be carried out by four 60% scale versions of the final ND-LAr modules. These single modules will be integrated into a 2 × 2 array with a unified DAQ system and deployed in the NuMI beam in the MINOS experimental hall at Fermilab. The integrated 2 × 2 experiment will begin to take data in spring of 2023. As of the publication of this document, the first two modules, Module-0 and Module-1, have been commissioned

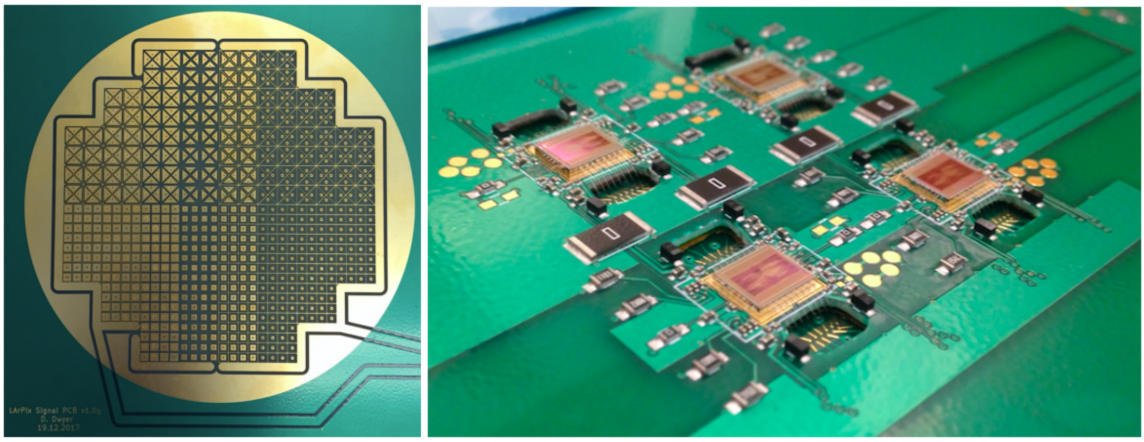

Figure 6.9: Photograph of the LArPix prototype anode, showing the TPC-facing side with pixelated charge collection pads (left) and the back side of the readout assembly (right). This system has only 128 of the pads instrumented, which are interfaced to four LArPix ASICs in a two-layer PCB.

at the University of Bern and have been transported to FNAL for integration with the 2×2 cryostat. The remaining two modules are currently under construction at Bern and will be validated in individual runs before subsequent transit and integration.

6.4.1 Module-0

Module-0 is the first demonstration of a scale model of the ArgonCube design is is 60% of the scale of ND-LAr and the anode is made up of 2x4 LArPix tiles. Each of the outer tiles holds a set of light detection systems [**?**].

The Module-0 detector was commissioned in April of 2021, running at the University of Bern from 2021-04-02 to 2021-04-10, collecting a total of 2.5×10^7 charge and light triggered cosmic ray events (Figure 6.4.1). A selection of these events, with some very simple reconstruction of drift position using drift time, are shown in Figure 6.4.1.

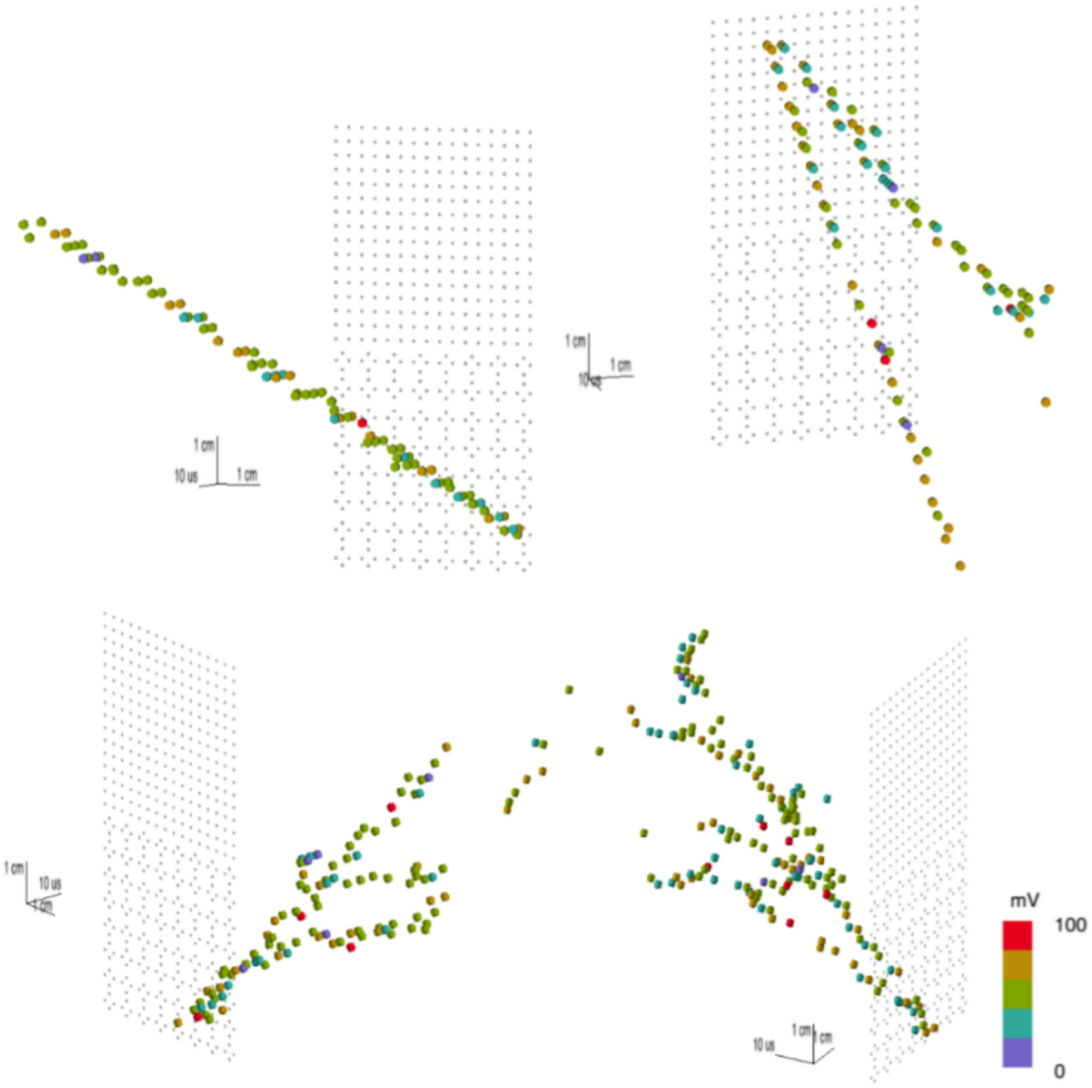

Figure 6.10: Selection of tracks recorded by the LArPix prototype shown in Figure 6.3.4 in a 60-cm drift LArTPC. The upper figures show simple straight muon tracks, while the lower figures show small electromagnetic showers. These hits are raw data, with no additional filtering included.

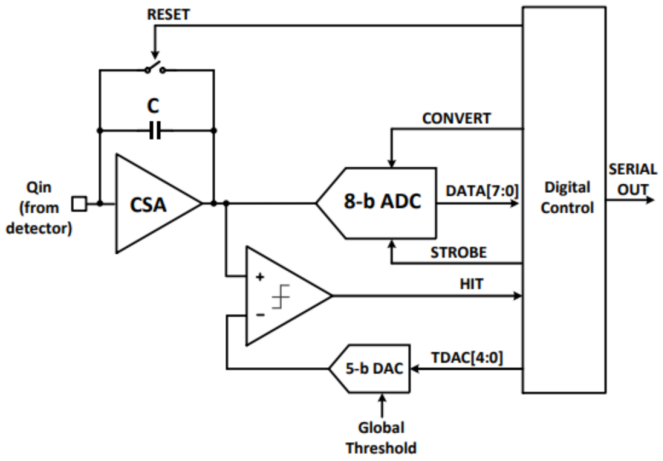

Figure 6.11: Block Diagram of the LArPix application-specific integrated circuit (ASIC).

6.4.2 Module-1

Module1 is the second in the series of four small-scale ArgonCube modules. This detector is designed identically to module0, with some small differences in grounding schemes. The module1 detector was commissioned at the University of Bern, running from 2022-02-07 to 2022-02-11.

6.4.3 ArgonCube 2×2

The 2×2 demonstrator will be the first prototype which has multiple ArgonCube modules working together in tandem. This is also the first prototype which will run in a neutrino beam. It will run at FNAL in the NuMI beam, using some components of MINOS (the Minerva ND) for external tagging of muons entering the detector.

6.5 ArgonCube Full Scale Demonstrator

The next iteration of the ND-LAr prototyping program is the Full-Scale Demonstrator (FSD). This will be the first full ND-LAr module produced which will undergo

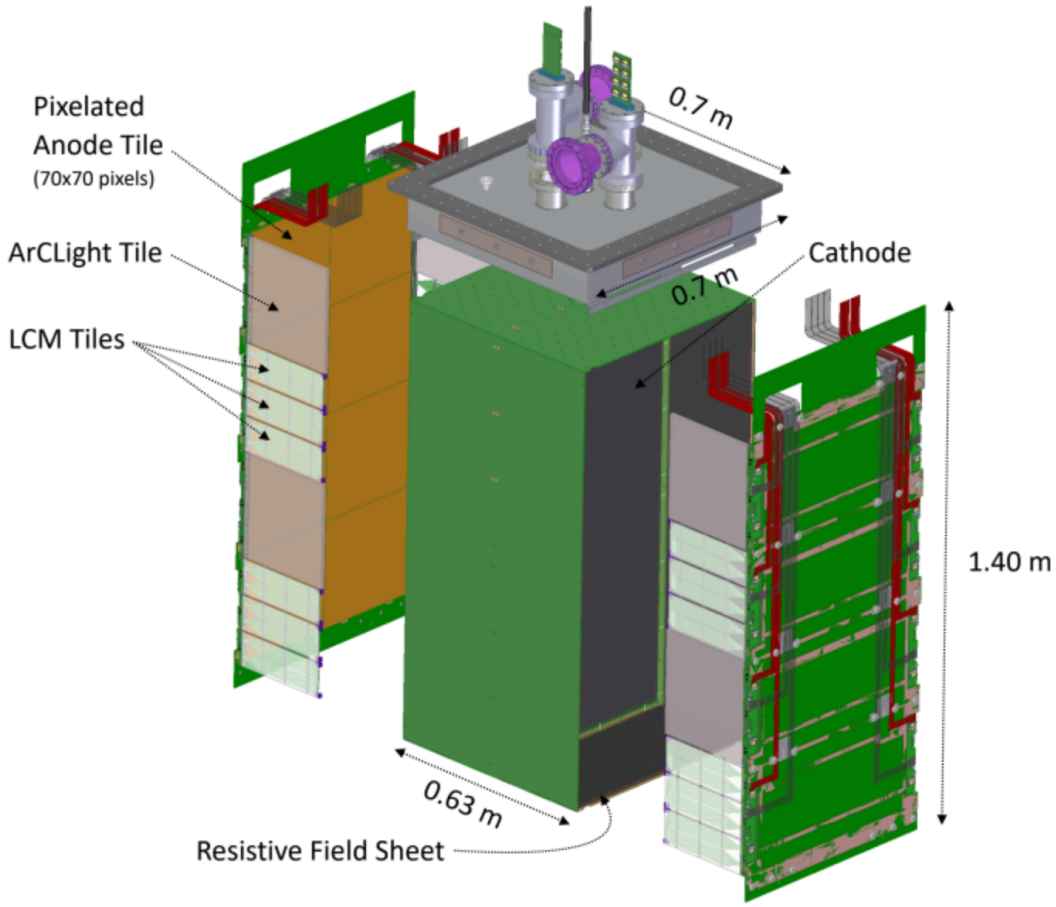

Figure 6.12: A CAD diagram of the 60% scale Module-0 detector. This module features 8 small LArPix tiles per anode plane, with 4 ArCLight panels and 12 LCM panels. The field shaping is provided by carbon-loaded Kapton laminate, described in Section 6.3.2 above [**?**].

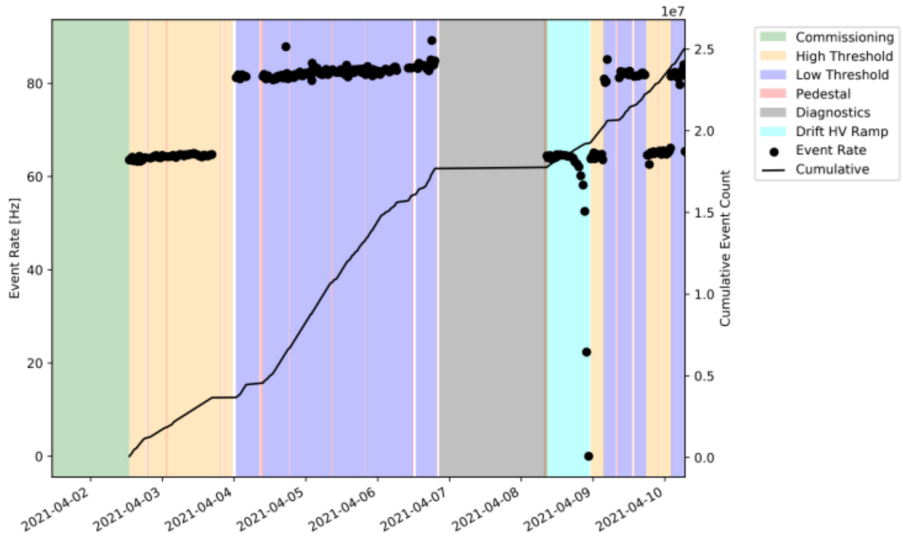

Figure 6.13: The event rate over the course of the initial run of the Module-0 detector. Instantaneous event rates (in Hz) are shown in points corresponding to the left vertical axis, while cumulative counts are indicated by the line corresponding to the right vertical axis. Specifics of individual runs are indicated by the color of the band and include threshold configurations, intermittent pedestal (dark ADC counts) and HV ramping for micro-physical studies [**?**].

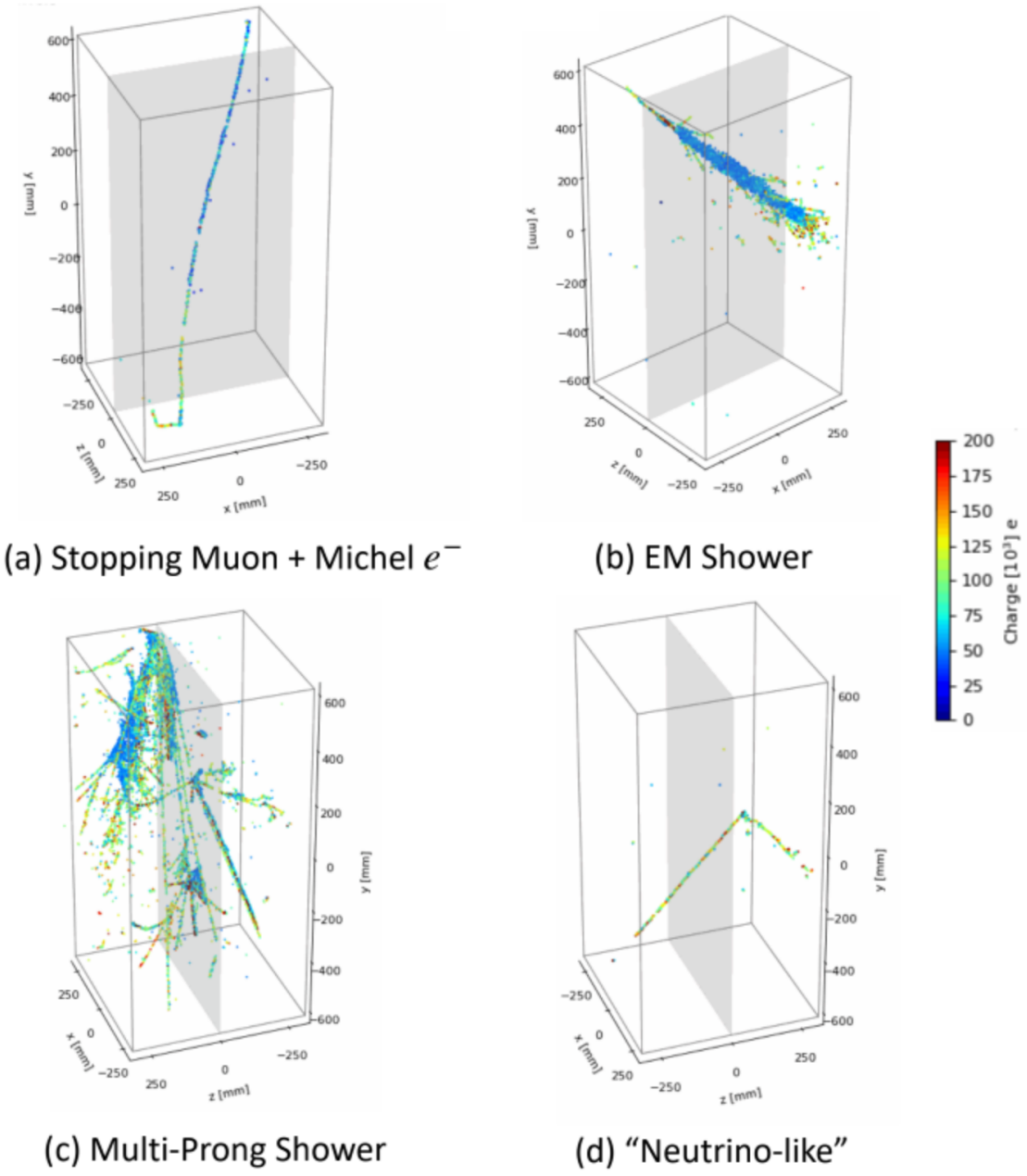

Figure 6.14: Gallery of four cosmic ray induced events collected by the Module-0 detector. In each subfigure, the gray plane represents the cathode ($z = 0$ mm), while the color scale indicates the collected charge associated with each hit in thousands of electrons. (b) shows an electromagnetic shower, while (d) appears to be a neutrino-like event, as the starting vertex appears to be contained inside of the active volume [**?**].

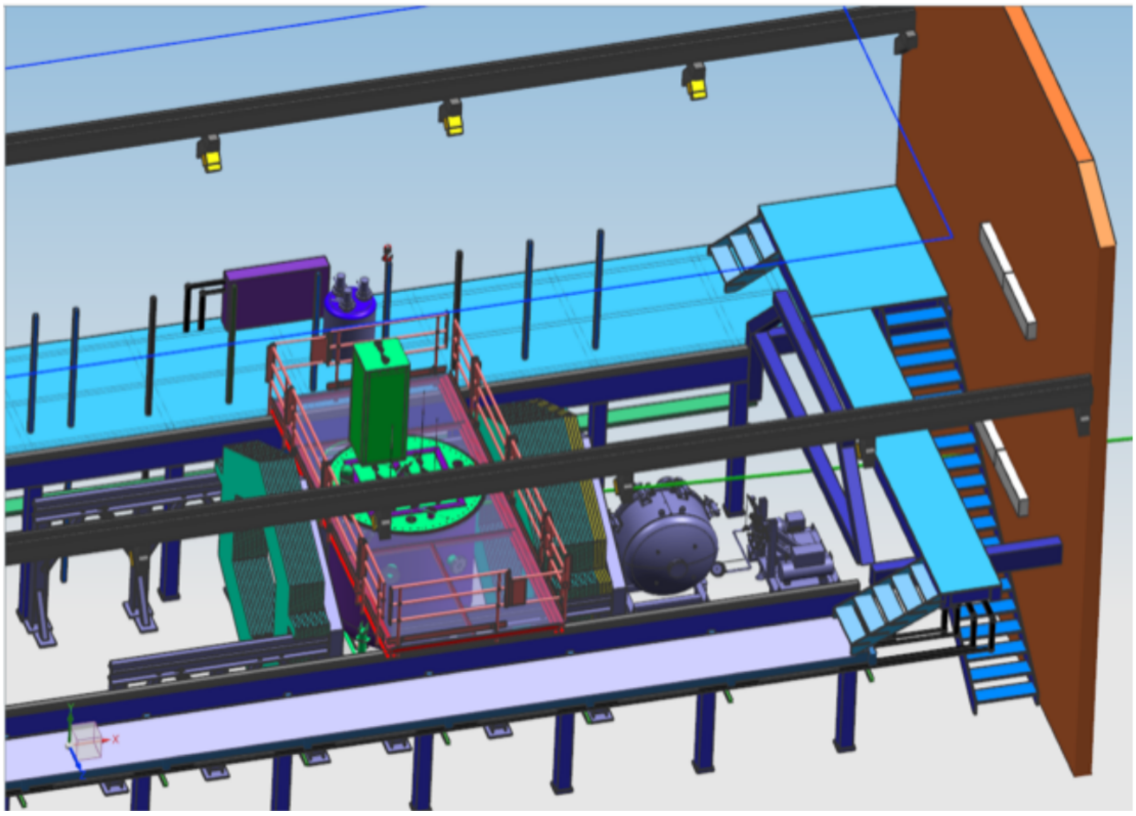

Figure 6.15: CAD model of the MINOS experimental hall showing the ArgonCube 2×2 cryostat with a single module withdrawn. In this diagram, the NuMI beam enters the hall from the lower left side. This configuration (called *ProtoDUNE-ND*) also features sections of the MINERνA detector upstream and downstream of the 2×2 cryostat, to provide muon tagging of incoming and outgoing charged particles. A prototype of the gas TPC of ND-GAr is also shown at the downstream end of the hall.

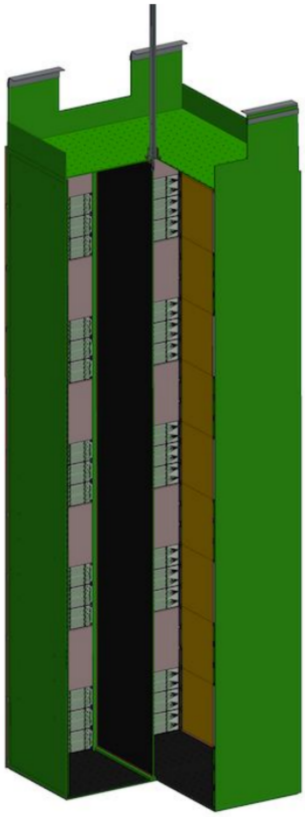

Figure 6.16: CAD drawing of the Full Scale Demonstrator design. Most features are common to the aforementioned 2 × 2 modules, scaled up to the full ND-LAr size (1 m × 1 m × 3 m.

significant testing as an individual experiment. Compared to the Single Cube modules and the 2 × 2 modules, this module has dimensions 100 cm × 100 cm × 300 cm. It features slightly larger charge readout tiles (30 cm × 50 cm, compared to Module0/1's 30 cm × 30 cm). Each anode plane features an array of 2 (horizontally) × 10 (vertically) such tiles with each hosting a light-readout-SiPM system on its edge. The slightly larger tiles also feature 160 LArPix ASICs for a total of 10240 charge readout channels per tile.

6.6 Single Cube and Distributed Testing

During the past few years, and particularly due to the COVID-19 pandemic, the development of small-scale, single-tile test stands was employed to improve the ability of institutions to pursue technology development for the ArgonCube program. These *Single Cubes* are typically 30cm x 30cm x 30cm, and may or may not feature a light readout system, depending upon their goals.

University of Colorado at Boulder, the Stanford Linear Accelerator Center (SLAC), the University of Texas at Austin, and other institutions have used these systems for testing field cage configurations, slow control systems, light detector integration, etc.

In particular, the SLAC system has lead in the validation of alternative field cage constructions, including striped resistor-chain styles and custom carbon-laden epoxy coatings, shown in Figure 6.6.

6.7 ND-GAr: DUNE-ND's Gaseous Argon TPC

Directly downstream of the ND-LAr detector is the downstream tracker, a multi-purpose detector designed primarily for sign-selection of through-going muon tracks and calorimetry beyond what ND-LAr alone is capable of.

This detector features a High-Pressure gas TPC (HPgTPC) surrounded by an electromagnetic calorimeter (ECAL), contained within a 0.5 T magnetic field, shown in Figure 6.7.

The HPgTPC is also capable of measuring charged particles with energy below the threshold of a LArTPC, so events originating within ND-GAr and low-energy particles escaping ND-LAr can be measured in more detail, greatly extending the particle ID (PID) performance of the overall system. This is especially useful in separation of proton- and pion-like particles.

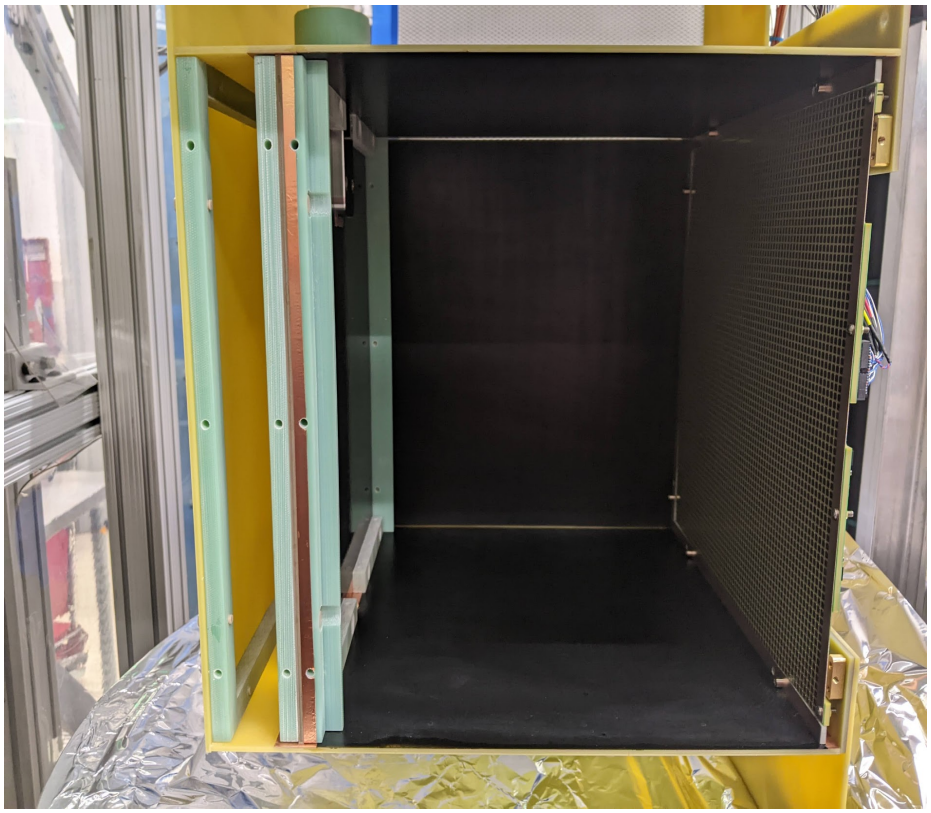

Figure 6.17: The SLAC Single Cube system outside of the cryostat, showing the single-sided TPC with one wall missing. Seen is the cathode (left), a single LArPix tile (right), and a custom carbon-doped sprayed epoxy field cage forming the remaining walls.

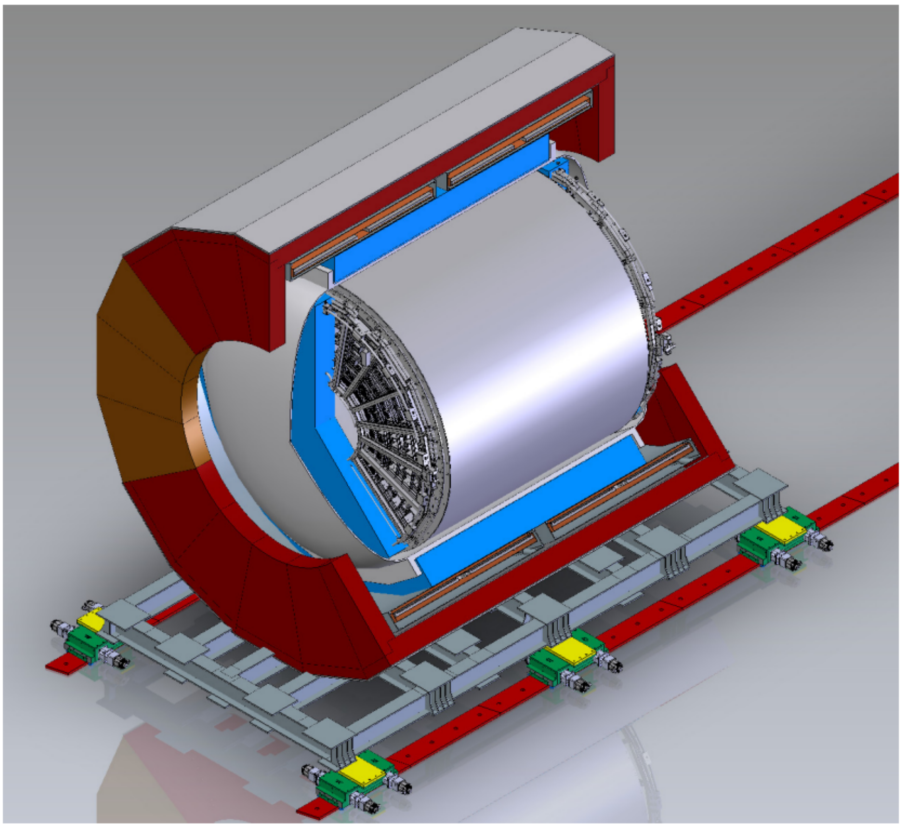

Figure 6.18: Schematic of ND-GAr showing the High-Pressure gas TPC (HPgTPC), its pressure vessel, the electromagnetic calorimeter (ECAL), the magnet, and the return iron. Not shown are external detectors for muon-tagging upstream of the detector.

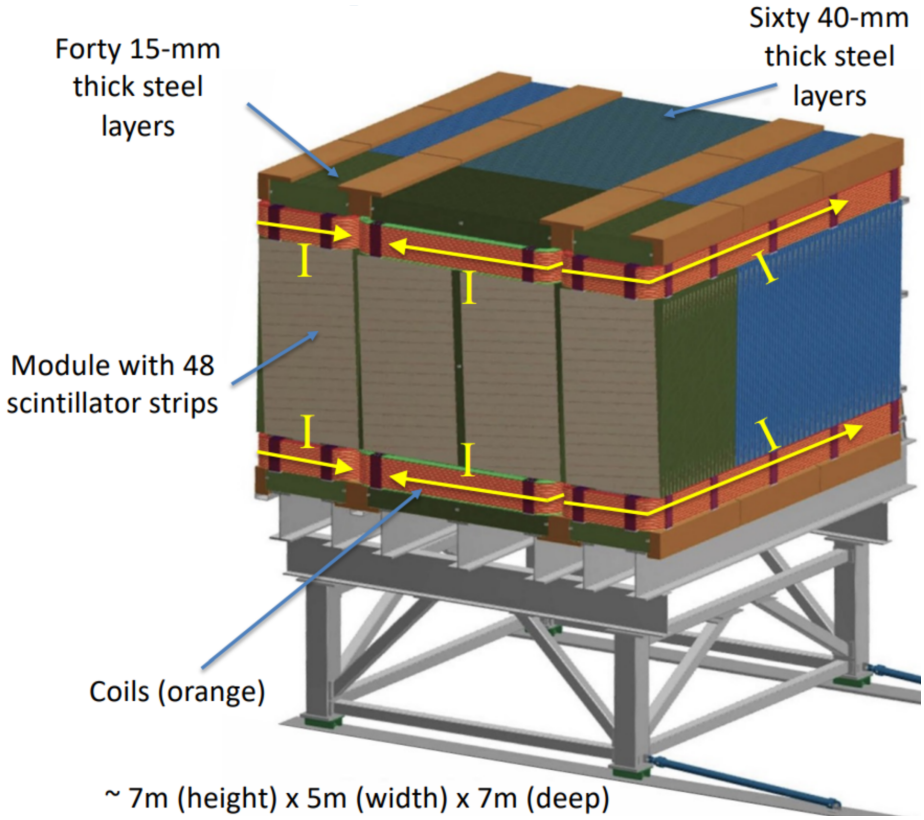

Figure 6.19: Diagram of The Muon Spectrometer external structure, including annotations describing important features. In this view, the beam (and ND-LAr) are on the forward-left side.

6.7.1 TMS: The Muon Spectrometer

As a matter of staging and cost management, the full ND-GAr detector will not be implemented immediately alongside the commission of the far detector modules and the first beam spills. Instead, the day-one downstream near detector will be a temporary magnetized spectrometer composed of 192 strips of 3.54 cm wide scintillator bars. These strips are interfaced with Y11 WLS fiber, allowing for resolution on the order of 4 cm in the bending plane, and approximately 45 cm in the remaining (vertical) direction. This resolution allows for a sign selection efficiency of 95%.

The detector is placed under a magnetic field, so that muons escaping the upstream ND-LAr detector can be measured for their electric charge. The direction of the

winding of the coils with two sets of coils on two smaller sections of the outside of the volume and a larger column in the center with a counter-oriented field produce a complicated field within the volume which is largely isolated to the TMS itself. This design is primarily to prevent excessive magnetic fields within the upstream and downstream elements of the near detector complex. The system features support for Hilman rollers for interface with the PRISM motion system.

6.8 SAND: The System for On-Axis Neutrino Detection

The System for On-Axis Neutrino Detection (SAND) is the component of the ND experimental complex which is permanently on-axis, and will serve as a beam monitor as well as a multi-purpose detector designed to provide precision cross section measurements on various nuclear targets.

The SAND detector will be magnetized using a re-purposed KLOE superconducting magnet. Allowing for calorimetry and spectrometry and taking advantage of an already well-understood magnetic field shaping device.

The SAND system features a large volume of scintillating straw-tube trackers (STT), surrounded by a front-facing electromagnetic calorimeter. The system also contains a 1T volume of LAr (called the *SAND GRAIN*) which serves as a target for the other tracking elements (Figure 6.8).

This detector will provide a measurement of the beam flux using a LAr target and can be leveraged by the PRISM system to alert of shifts in beam delivery systematic parameters. Such a shift can be measured on short timescales and may prompt the PRISM system to return to its on-axis position for re-calibration on the fly.

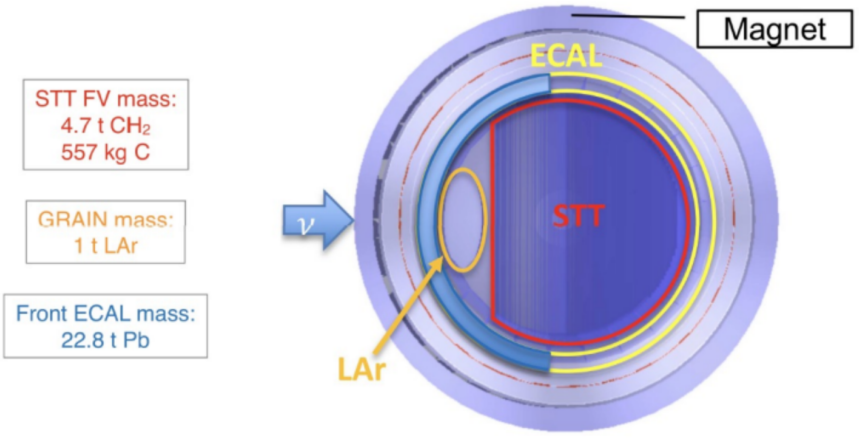

Figure 6.20: Cutaway diagram of the SAND detector system, showing the main detector elements: the GRAIN LAr target, the downstream STT scintillator system, and the surrounding electromagnetic calorimeter.

CHAPTER VII

Calibration

The need for a dedicated calibration program with a signal injection mechanism in DUNE LAr-ND is driven by the need for a reliable understanding of the detector's operation as it changes with age, under mechanical stresses, and in all of the small ways in which its design deviates from the ideal conditions of a TPC. DUNE is expected to operate for 15 years or more with as little interruption as possible in order to reach the estimated discovery potential for δ_{CP} shown in Figure 4.2.

As described in Chapter III, a TPC operates by the motion of deposited charge through a volume of matter towards an instrumented anode plane, where it can be read out. The reconstruction of this 3-dimensional space relies upon accurate deconvolution of the anode signals from the $(x_{\mathrm{pixel}}, y_{\mathrm{pixel}}, t_{\mathrm{ionization}}, t_{\mathrm{readout}})$ coordinate system to the $(x, y, z, t_{\mathrm{ionization}})$ system. These coordinates define the *image* or *reconstructed* space and the *true* space, respectively. In the simplest model, the drift field is perfectly uniform and uni-directional within the volume, so that ionized electron clouds drift straight toward the anode. Then, the x and y deflection is minimal, and the reconstructed z position is simply $v_{\mathrm{drift}}\Delta t_{\mathrm{drift}}$, so the image and true spaces are equal, up to the finite resolution of the anode electronics. In reality, small differences in the relative location of field shaping devices, including tilting or mis-alignment of cathode or anode planes, choices of field cage design – or failures thereof – can

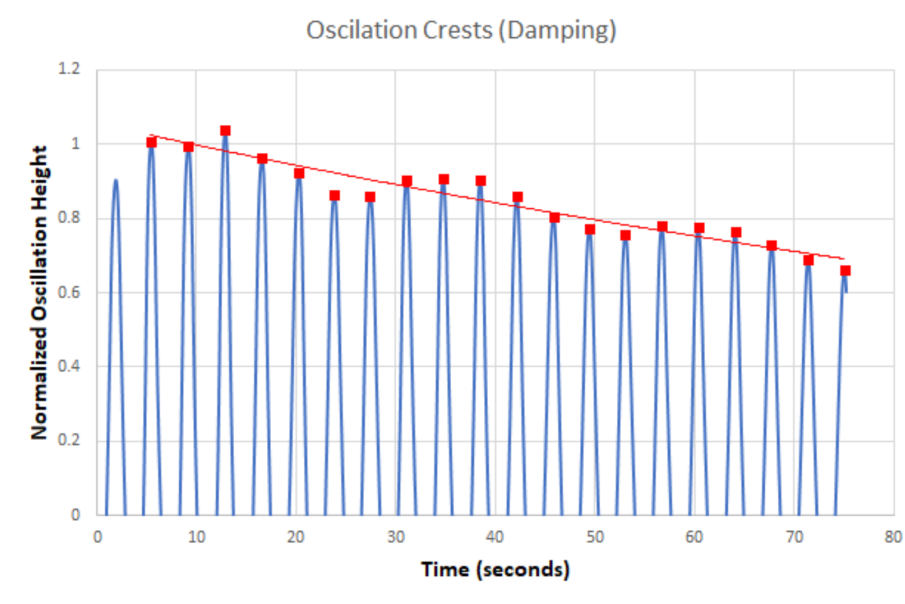

Figure 7.1: Finite element analysis of fluid flow resonances induced by PRISM-like motion within a segmented detector geometry. The natural period of this sloshing motion is 3.66 seconds and the damping factor is $\approx 9.3 \times 10^{-4}$.

produce a non-ideal drift field, complicating deconvolution and necessitating robust measurements of drift field properties.

One particular source of agitation to the ND system is the PRISM motion subsystems. As discussed in Chapter VI, the PRISM program requires the motion of the detector along the direction transverse to the LBNF beam. This motion is supported by a set of Hilman rollers, and is constrained to extremely slow speeds. Still, this motion will be repeated on a weekly timescale, and preliminary simulations have shown that resonant motion in the form of sloshing of liquid material within the cryostat will be induced. The ND-LAr design includes baffle structures to resist this motion, but these elements are integrated into the module structure which are integrated with field shaping elements, thus the alignment of these elements are subject to forces resulting from this sloshing motion. The repeated motion of the entire cryostat should be followed by a re-calibration of the drift field at each new position, to account for any displacement induced by the motion.

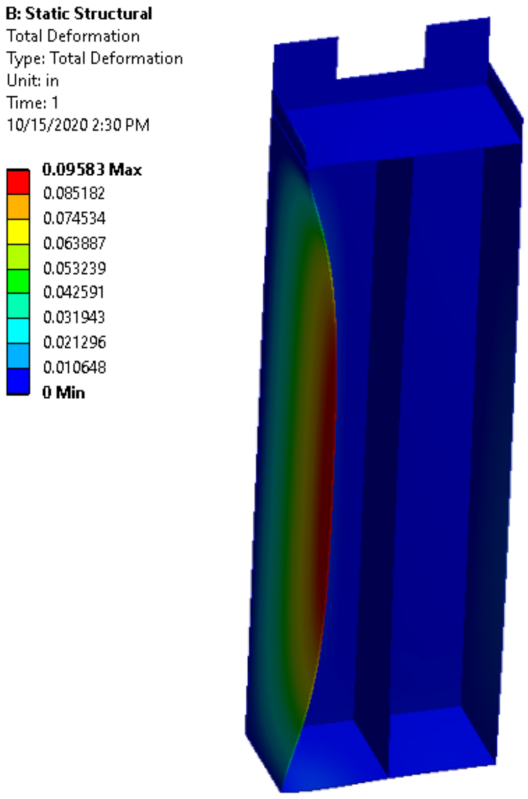

Figure 7.2: The static deformation of an ArgonCube module due to pressure waves in sloshing LAr (see Figure VII). The maximum displacement of the field structure is seen in the center of the anode with a magnitude of 0.09583 inches (2.434 mm). This analysis assumes no plastic deformation of module structures due to this sloshing.

The structural elements of each module are made from G10, a glass-fiber reinforced epoxy laminate. Each module hangs from an aluminum flange, which forms part of the cryostat sealing surface. The module structure supports many printed circuit board elements (which are themselves laminates of G10 and copper, with surface-mounted components), field shaping materials, light-detection systems, and other components. While the design of the modules anticipates some thermal expansion/shrinkage and attempts to account for this with the inclusion of materials matched by their coefficient of thermal expansion (CTE), spring washers, and other techniques to allow for changes in fitment with respect to temperature, these changes have the potential to effect the alignment of field structures.

Even in the case of perfect alignment of field shaping elements, the design of those elements, and the electrical properties of other materials inside of the TPC volume will have an effect on the resulting field. The traditional field cage configuration, the resistor-chain field cage, produces some inhomogeneities in the drift field on the scale of the strip spacing and width. This effect is negligible near the center of the drift volume, but becomes important near the edges. Even in the case of a uniformly-resistive sheet material as in a DR8 field shell, finite-width strips of conductor on the anode and cathode sides meant for a "metalization" contact have the effect of producing a "lip", which distorts the field by up to 1% of the nominal value throughout the volume. Holes in the field cage for LAr recirculation can further complicate the field (Figure 7.7). Apart from the field cage system itself, materials other than LAr inside of the TPC volume, such as the plastic scintillators and fibers found in the light detection systems, have the capacity to become polarized or collect free charges over time, further distorting the field as it runs.

Over the course of the experiment, it is expected that some materials will undergo changes due to aging. The module structure has several laminated and composite materials and many polymeric materials which may interact with the LAr over time

in a way which can change their composition. There is also a known time dependence of certain field cage configurations – the DR8 and sprayed field cage solutions must settle into a resistance by being "burned in" by high voltage over time. Though this settling mostly occurs over the first few days of running, a repeatable calibration program for measuring the drift field would provide a way to correct for defects due to a slow variation of field cage resistance [**?**].

Lastly, it is known from other large-scale LAr TPC experiments that the accumulation of *space charge* or the buildup of a positive charge density due to the much slower transport of Ar_2^+ can effect the drift field uniformity. The magnitude of this effect is driven by the intensity of cosmic rays (or generally, the rate of ionization of the medium), the drift velocities of electrons and ionized Ar, and the total drift length. A simple estimate of the concentration of space charges indicates that this effect scales with total drift length and ionization rate, and scales inversely with average drift velocity. Because the drift length of ND-LAr is considerably shorter than MicroBooNE and the detector system is deeper underground, this effect is expected to be much smaller, but it is still expected to contribute to an overall inwards deflection of electrons as they drift towards the anode plane as seen in MicroBooNE.

7.1 Calibration Sources

Calibration measurements should be repeatable often enough to gauge the evolution of those measurements over time, as well as to ensure that calibration is done close in time to measurements of the detector. The calibration measurements presented in this thesis utilize cosmic ray muon flux, and a charge injection system mounted to the cathode panel. In addition, DUNE ND-LAr will receive a considerable flux of "rock muons" which are muons generated by upstream neutrino interactions originating from the LBNF beam.

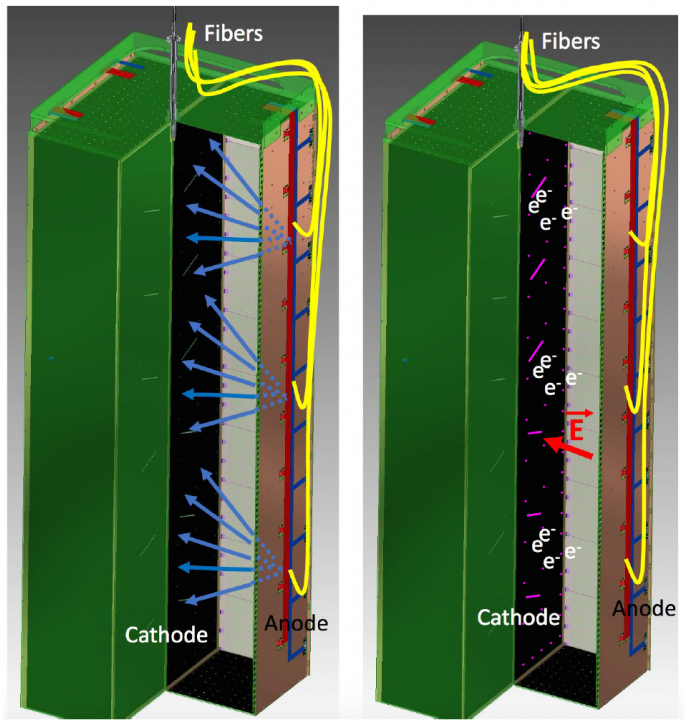

Figure 7.3: Diagram of the photoelectric charge injection system. 266 nm light is injected through a series of feedthroughs along the center-line of the anode plane and is incident on photocathodes mounted on the TPC cathode wall. The resulting charge drifts through the electric field, producing a distorted image of a known "test pattern" as a way to probe the quality of the drift field within the detector.

7.1.1 Photoelectric Charge Injection System

DUNE ND will include a laser charge injection system which utilizes photocathodes mounted to the TPC cathode to produce a charge signal with a pre-defined spatial pattern and with specific timing. This charge cloud will drift from cathode to anode, undergoing deflection according to any inhomogeneities in the drift field that may be present. As with other deposited charge, this cloud will also undergo diffusion on its way to the charge readout system. This charge injection system will provide a fast way to validate the drift model, assess integrated E field defects, and measure LAr purity and diffusion properties.

The laser source is a CFR200 Quantel Compact Nd:YAG 266 nm, pulsed laser.

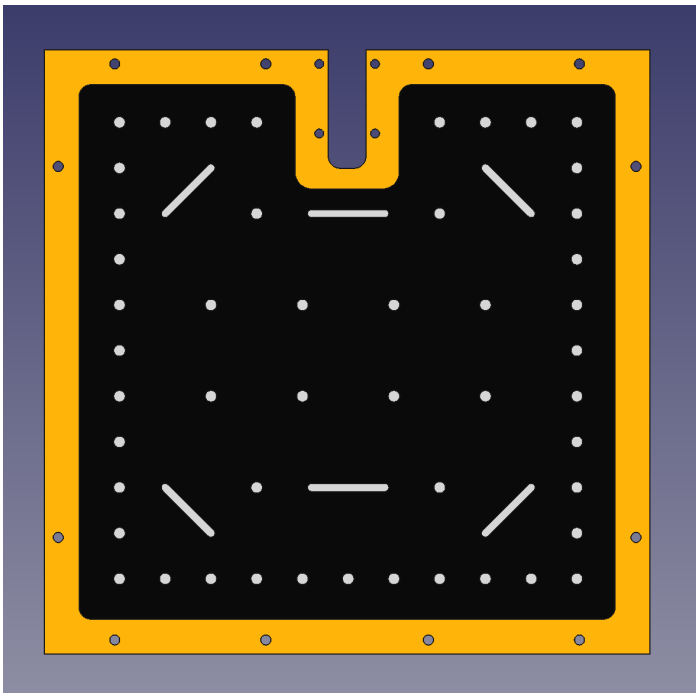

Figure 7.4: CAD drawing of the SLAC Cube cathode with nominal test pattern

The light travels from this source through a multiplexer and then fed into the cryostat through a SMA coupling in the top flange of each module. Six fibers are used per module, with three feedthroughs on each anode plane. An internal fiber run then travels through a shielding tube to the back of each anode plane. There is a small "spool" around which excess fiber can be run to accommodate slack and thermal shrinkage due to cryogenic temperatures. From here, the fibers interface with a small J-shaped light guide which feeds through the anode to the inside of the TPC.

The photoelectric targets mounted to the cathode plane are arranged with high density near the edges of the drift volume, where it is expected that drift field inhomogeneities will be greatest.

7.1.2 Cosmic Ray Tracks

Cosmic rays interact in the Earth's upper atmosphere, producing complex air showers containing a mess of electromagnetic and hadronic components. Of these

secondary particles, the components that survive and reach the surface are largely muons and gamma rays. In the DUNE ND-LAr, muons present as long straight tracks, being minimally ionizing particles. These particles deposit very little energy (2 MeV g^{-1} cm^2), with very little change to the direction of their momentum. Such particles can potentially stop within the detector volume, either by decaying (producing a decay electron known as a Michel electron), or losing enough energy that they stop ionizing the surrounding material. Those muons that pass through the detector as minimally ionizing particles (MIPs) can provide an excellent standard ruler against which the anode image can be compared to measure curvature induced by defects in the drift field.

7.2 Calibration Measurements

7.2.1 Drift Field Uniformity

Certain deviations from a flat, uniform drift field are expected due to design constraints and the effects of polarization and charge accumulation within the TPC volume. The need for a field shaping device is primarily driven by the impingement of external electric fields into the TPC volume. Close to the center of the TPC, along the drift axis, the drift field will be very uniform and uni-directional. This is close to the simple "field between two infinite conductors" example with which one may be familiar. In an array of modules with similar electrostatic configurations, this assumption may even be good close to the edges of an individual TPC volume, as long as that volume borders another TPC. Close to the the terminal edges of the detector, however, field lines tend to bow outwards, as the potential gradient changes significantly from a linear shape. The inclusion of a field shaping device (a "field cage" or "field shell") helps to maintain this linearity on the edges of each TPC volume. These devices take the form of resistor-chain voltage dividers connecting a series of

Figure 7.5: SLAC Cube TPC outfitted with a resistor-chain type field shaping device.

conducting rings parallel with intended equipotential surfaces of the field, or, as in the proposed field cage for DUNE ND-LAr, a continuously resistive sheet material.

A secondary effect of these devices is to provide a resistive coupling between anode and cathode, which, in the case of electrical fault, can more safely route stored energy and avoid damage to sensitive electronics on the anode. No field shaping device is perfectly performant, however, so modeling the expected fields produced by a given device is critical to design and subsequent calibration measurements.

7.2.1.1 Space Charge Accumulation

The space charge effect is the process by which, over time, the TPC volume develops a net positive charge. This is due to the difference in the drift velocity of the electron and the ionized Ar_2^+, which are much slower. The effect, in steady-state, is a linear charge density which increases from anode to cathode. The magnitude of this charge distribution is dependent upon the drift field, the rate of ionization within

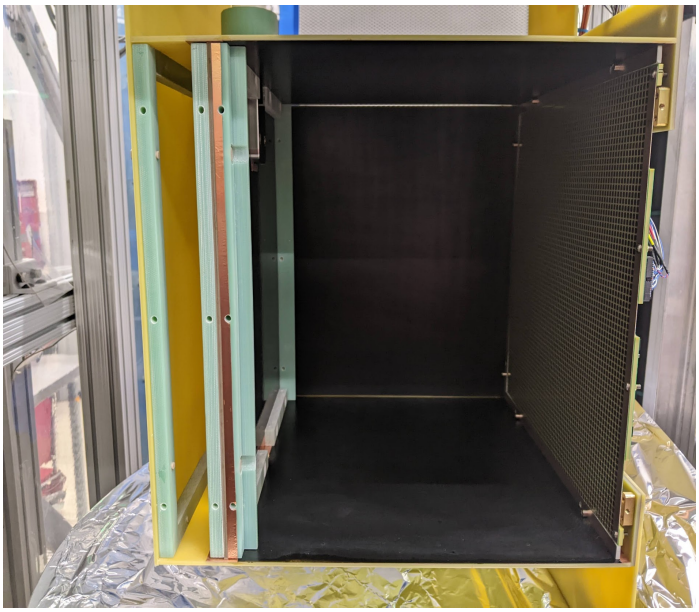

Figure 7.6: SLAC Cube TPC outfitted with a carbon coating type field shaping device.

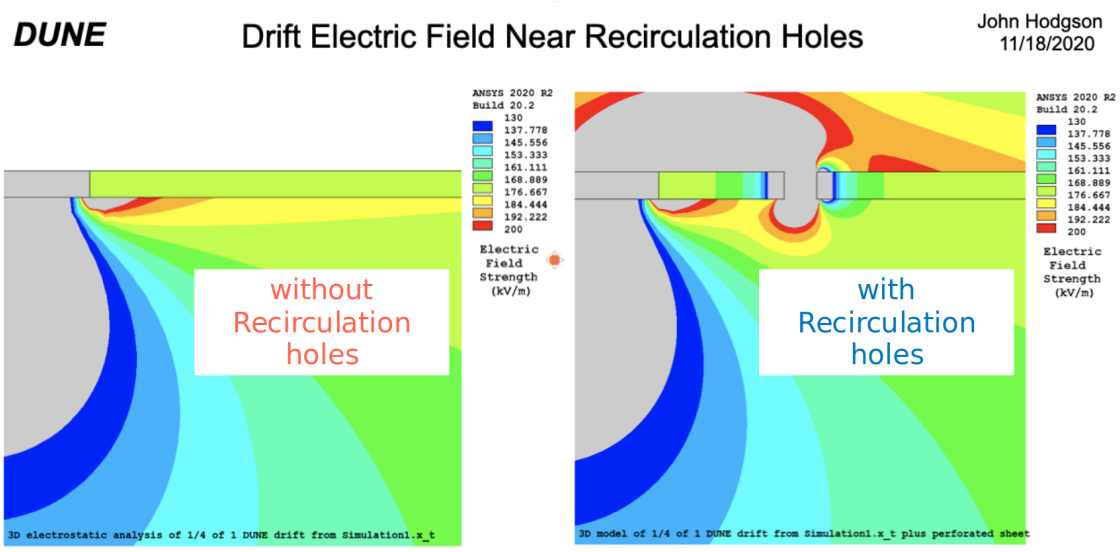

Figure 7.7: FEM calculation of the drift field in ND-LAr near a small recirculation hole in the top of a resistive-sheet field cage.

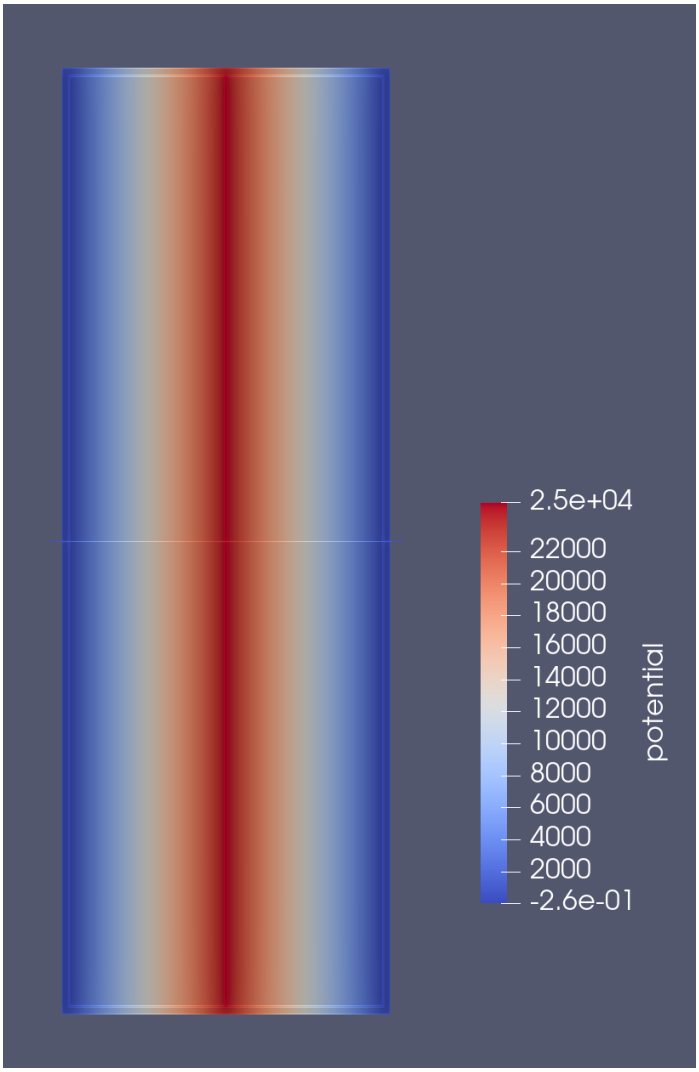

Figure 7.8: FEM calculation of the drift field in ND-LAr with a resistor-chain field cage design with a configuration of 10 strips of width 3mm between each anode and cathode.

the volume, and the distance between anode and cathode. This effect can produce defects in the drift field on the order of 10% [*Abratenko et al.* (2020)].

7.2.1.2 Crossing Muon Analysis

The Module0 and Module1 experiments served as the first tests of the integrated ArgonCube systems. They are $\tilde{6}0\%$ scale versions of a full ND-LAr TPC, each containing two anodes with a set of 2×4 LArPix tiles per anode and 8 light detection systems (ArCLight and LCM, in an alternating pattern as shown in Figure 7.2.1.2) per anode. These modules have a 30 cm drift distance and a total fiducial volume of approximately 60 cm (horizontal) × 120 cm (vertical) × 30 cm (drift) × 2 (TPCs). The Module0 experiment ran between April 2 and April 10, 2021, while the Module1 experiment was commissioned and ran from February 7 to February 11, 2022.

Using a selection of cosmic ray muons which pass through both anodes of each of these modules, we can make precise measurements of the effects of non-uniform drift fields. The drift model assumes thermalized electrons moving along field lines within the TPC with a velocity dependent upon the local magnitude of the drift field, as shown in Figure 3.4. As charge bundles follow these field lines, they may be deflected in the transverse (x, y) directions, and the time span of their drifting may be effected by this change in overall path length, or due to variations in drift field strength. We define two coordinate systems for understanding these spatial deformations:

- *Image space*, which is the naive 3D reconstruction one can make by assuming that the deposition x and y positions of a charge bundle are just the position of the pixel on which they register a hit. The z position in this scheme is found from the drift interval (thus a reliable t_0 is required for this analysis) and the nominal drift velocity: $z_{\text{reco}} = (t_{\text{hit}} - t_{\text{dep.}})\hat{v}_{\text{drift}}$

- *True space*, which is the true location of deposited energy within the detector, which aligns with the physical boundaries of the TPC.

The goal of the analysis is to understand the mapping which relates these two spaces to each other. If the field within the TPC is known completely, this relationship can be determined by numerical integration along drift paths of charges, as described in Chapter III and shown (on a small scale) in Figure 3.5:

$$\vec{r}_{\text{image}} = \vec{r}_{\text{true}} + \int_{t_{\text{dep.}}}^{t_{\text{hit}}} v_{\text{drift}}(\vec{r})\, dt \tag{7.1}$$

In the simple case where $\vec{v}_{\text{drift}}(\vec{r}) = \hat{v}_{\text{drift}}\hat{z}$, we can see that Equation 7.1 simplifies to

$$\vec{r}_{\text{image}} = \vec{r}_{\text{hit}} + (t_{\text{hit}} - t_{\text{dep.}})\hat{v}_{\text{drift}}\hat{z} \tag{7.2}$$

A key feature of this method of reconstruction of 3D charge positions is that errors due to imperfections in the drift field are cumulative with distance from the anode plane. For this analysis, we look at a selection of cosmic ray muon tracks in both the Module0 and Module1 TPCs which cross through both anode planes, providing two anchor points in 3D space where there is little difference between the image space and the true space locations of charge bundles. A subset of these tracks with simple line fit reconstructions can be seen in Figure 7.2.1.2.

The *true track* hypothesis is determined by a principal component analysis of the five hits nearest to each anode. This number of anchor points is chosen to avoid bias due to the occasional inclusion of noise hits in the track clustering as well as the aliasing effect of the 4.434 mm pixel pitch. The true hit location is then taken to be the location of along the true track axis which is closest to the reco hit. A diagram of this method is shown in Figure 7.2.1.2.

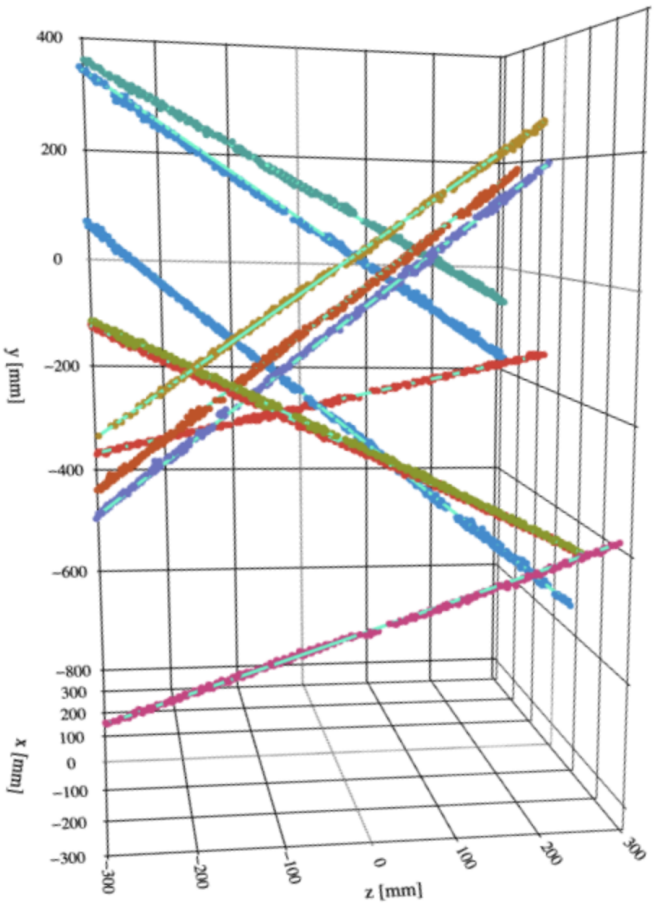

Figure 7.9: A subset of the tracks used in this analysis. These tracks are selected because they pass through both anode planes (located at $z = \pm 300$ mm). The cathode (not depicted) is located at $z = 0$ mm. Each track's hits are shown in a different color, with the corresponding line fit shown in cyan.

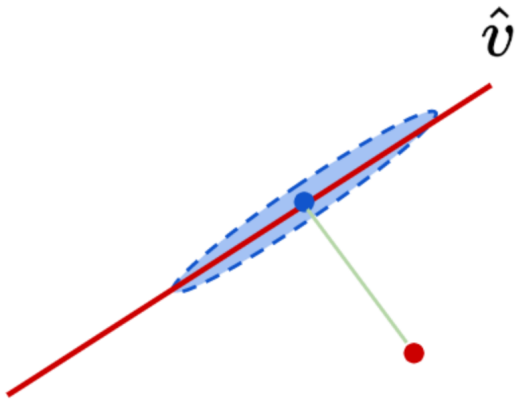

Figure 7.10: The true hit finding method involves comparing the 3D position of the reconstructed hits to the nearby PCA axis. The true hit location is taken to be the point along this axis which is nearest to the reco hit position. As the uncertainty in the true position is greater in the direction of the axis than in the radial direction, there is a relative weighting of these two contributions to the aggregated displacement fields, resulting in a true hit hypothesis which appears like an elongated gaussian cloud.

From this selection of anode-anode crossing track hits, we measure the average displacement within a voxelization of the TPCs with 2 cm × 2 cm × 2 cm bins. The x, y, and z projections of the hit-to-hit displacements are weighted according to their angle with respect to their PCA axis. For example, the x displacement for a given hit with a 3D displacement $\vec{ds}$ belonging to a track with PCA axis $\hat{v}$ is $\vec{ds} \cdot \hat{x}$ and is given a an uncertainty (whose inverse is used as a weight):

$$\sigma_x = \sqrt{((\hat{v} \cdot \hat{x})\sigma_{\text{axial}})^2 + (|\hat{v} \times \hat{x}|\sigma_{\text{radial}})^2} \tag{7.3}$$

So then the value of the measured displacement field in a given direction within a voxel is simply the weighted average of the hit-to-hit displacements for reconstructed hits which fall into this 3D bin. Figure 7.2.1.2 shows the value of this field in the z-slice nearest to the cathode in the Module1 negative-z TPC. This is the region expected to show the greatest degree of deformity.

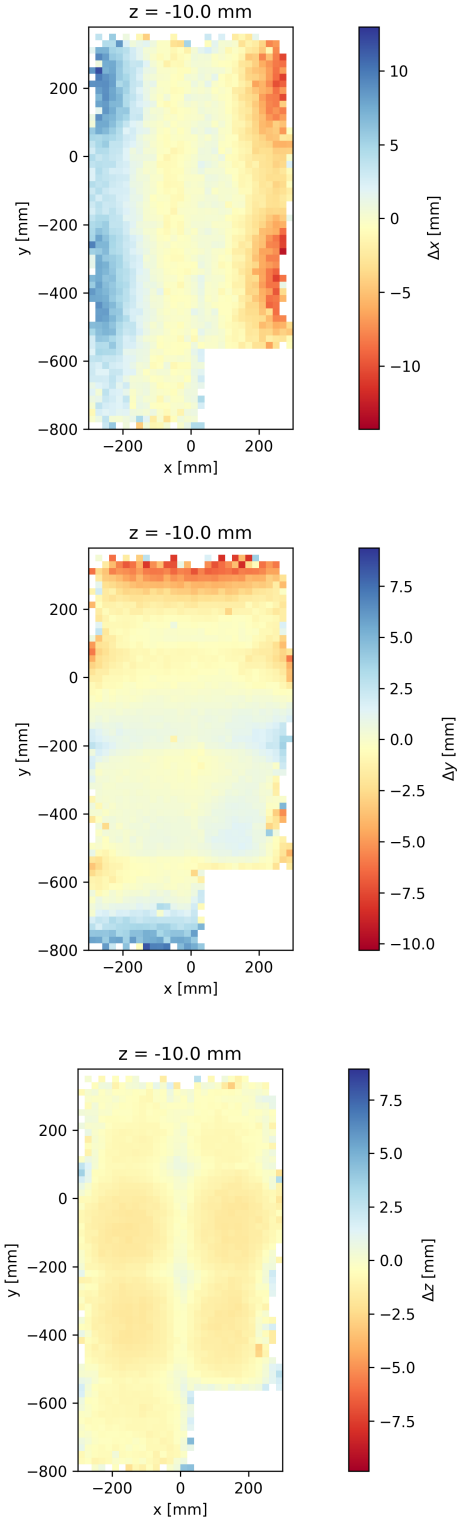

Figure 7.11: Spatial displacement maps of *reco* - *true* hit positions within the Module1 TPC in the 2 cm slice in z closest to the left side of the cathode. These maps indicate an inwards deflection in x and y, with a noticeable correlation of the x deflection to the position of the LCM light detection panels. The magnitude of these displacements are on the order of 10 mm.

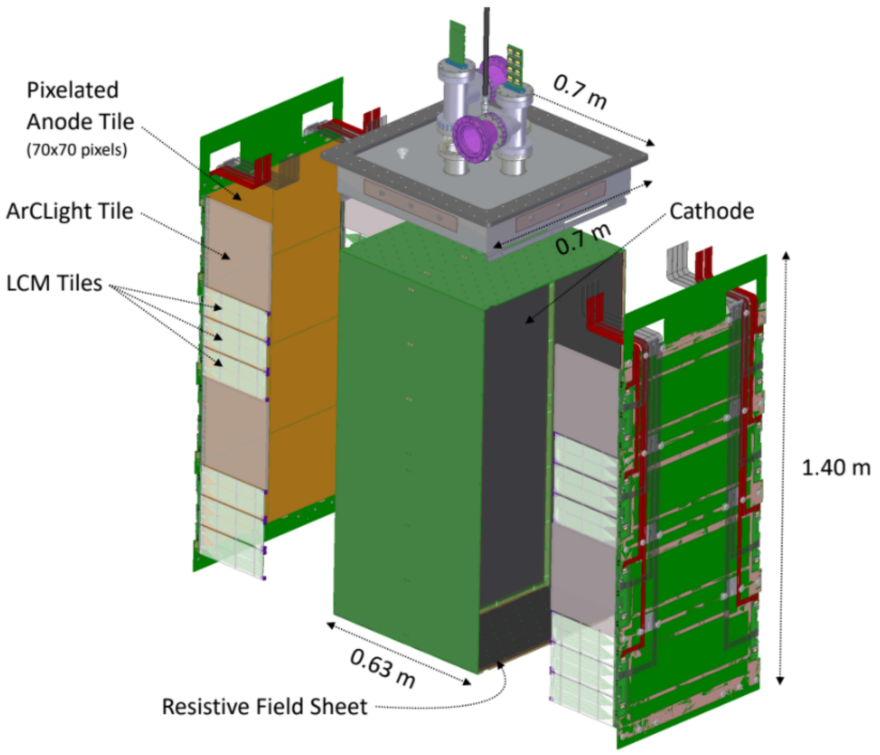

Figure 7.12: An exploded-view CAD model of the assembled Module0/Module1 module structure. Note the light detection systems mounted to the outer edges of the anode LArPix tiles. The arrangement here is not reflective of the final configuration of these tiles, which is properly shown in Figure 7.2.1.2, prior to Module0's final assembly.

What is observed is a relatively flat displacement field throughout the TPC volumes, with an accumulation of spatial distortion effects near the cathode. The magnitude of the spatial distortions is on the order of 10 mm, with some voxels showing a deflection of at most 15 mm. Compared to the pixel pitch of 4.434 mm in the Module0 and Module1 versions of the LArPix tiles, this is a relatively minor effect and one which can be corrected for before higher-levels of reconstruction.

Most notably, the x-component of the displacement field nearest to the Module1 cathode shows a significant correlation with the position of the LCM light collection systems on the edges of the TPC volume. The layout of the light detector systems is shown in Figure 7.2.1.2.

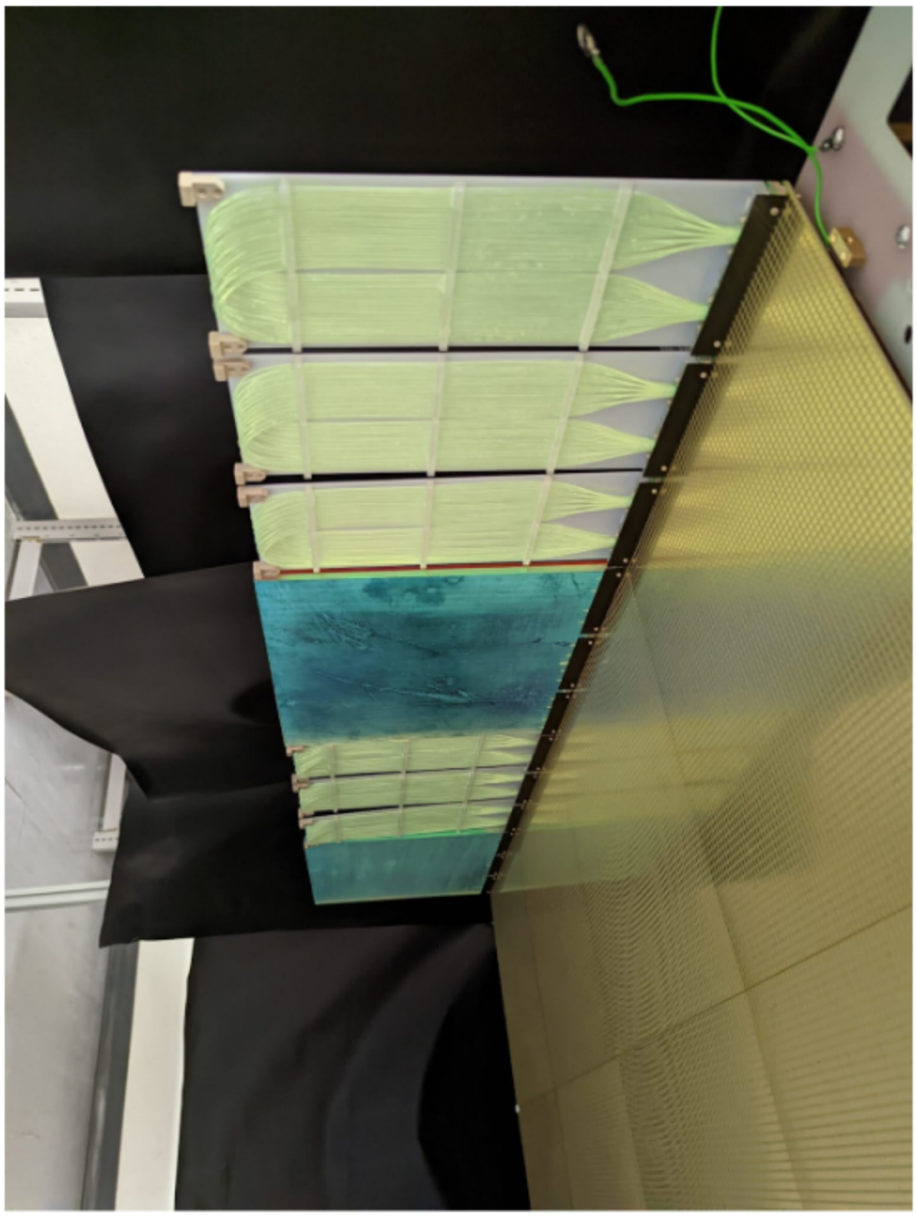

Figure 7.13: A photograph of the assembled Module0 anode plane assembly before integration with the field shell and structural elements of the module. The upper right corner shows the top edge of the anode plane. The arrangement of the light detection systems along the plane is LCM-ARcLight-LCM-ARcLight.

The exact origin of this displacement effect and its relation to the LCM tile structure is still not fully understood, but a few hypotheses are being investigated. One possible explanation is the mechanical deformation of the relatively complex LCM structure, compared to the monolithic structure of the ArCLight panels. Figure 7.2.1.2 shows the looped-fiber structure of the LCM, mounted to a PCB plate which serves as a supporting structure. Mechanical bending of this structure could physically block the drift paths of some charge bundles deposited nearby. Another suggested origin for this phenomenon is purely electrical. These structures may have vastly different dielectric properties than the surrounding materials, causing large amounts of bound charge on the surfaces of the modules. This theory is disfavored currently as such bound charge distributions tend to produce attractive potential configurations, as shown in Figure 7.2.1.2. The last prominent hypothesis for this repulsion is the accumulation of charge in the form of drift electrons which terminate on the surface of these modules soon after high voltage is applied to the system. This negative charge density could produce the observed repulsive deflection behavior seen in Figure 7.2.1.2.

This same analysis was carried out on the opposite Module1 TPC and on Module0 data and a similar pattern is observed, with some variations in the magnitude of the effect and with some differences in which LCM tiles exhibit this behavior. More plots of the displacement field throughout the volume, including slices along different axes can be found in Appendix A.

Preliminary finite element method (FEM) simulations have been carried out to try to replicate the behavior seen in Module0 and Module1 data. Purely electrostatic configurations have been the initial target. Figure 7.2.1.2 shows the effects of drastically higher dielectric properties in the region around an LCM module. This results in an attractive potential, rather than a repulsive one seen in data.

Charge accumulation, whether negative drift elections or ionized Ar ions, can be

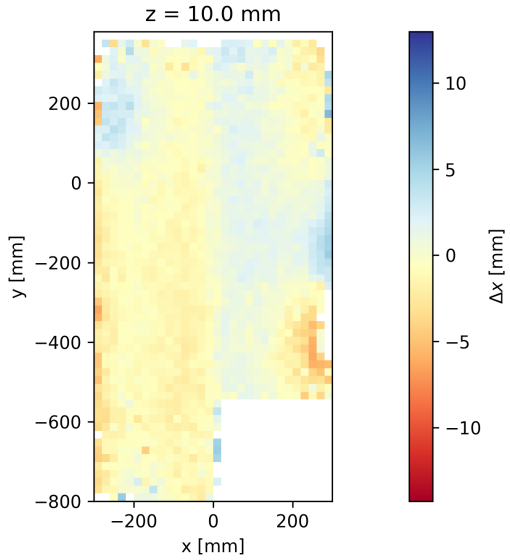

Figure 7.14: Spatial displacement map of the x-component of *reco* - *true* hit positions within the Module1 TPC in the 2 cm slice in z closest to the right side of the cathode. These maps show a similar pattern of inwards deflection as is seen in Figure **??**, but the magnitude of the effect is smaller ($\Delta x \approx 5$ mm), and only 3 of the 4 LCM tiles in this TPC seem to exhibit this behavior.

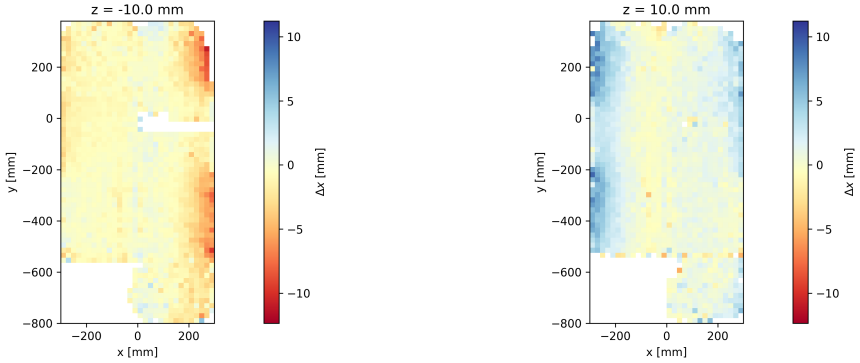

Figure 7.15: Spatial displacement maps of *reco* - *true* hit positions within the Module0 TPC in the 2 cm slice in z closest to the cathode (negative-z is shown in the left, positive-z is shown on the right). These maps indicate the same inwards deflection in x and y seen in the Module1 data, with a similar magnitude ($\Delta x \approx 10$ mm) as seen in the Module1 negative-z TPC. The spatial configuration of these high-displacement regions remains correlated with the position of LCM units, though this module only shows this behavior on modules on the right side of their respective anode planes.

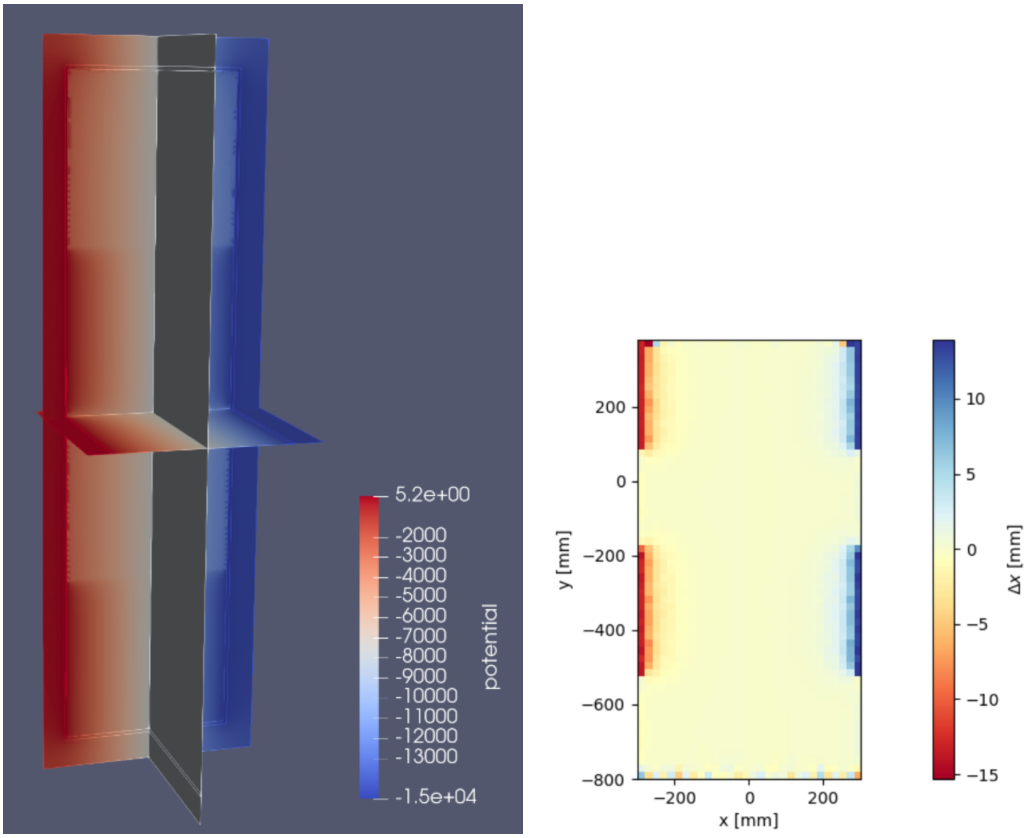

Figure 7.16: The effects of a vastly different ($\epsilon_{\text{rel}} = 10^4$) dielectric constant in a region of the TPC occupied by LCM modules. The left diagram shows a slice of the potential field very close to the edge of the fiducial volume ($x \approx -300mm$), where a large dielectric constant appears to "flatten" the gradient produced by the field shell exterior to these modules. The right plot is the resulting displacement map generated by simulation of drift paths along a grid aligned to the voxelization scheme described above. Note that this displacement map shows that these modules become attractive under this configuration.

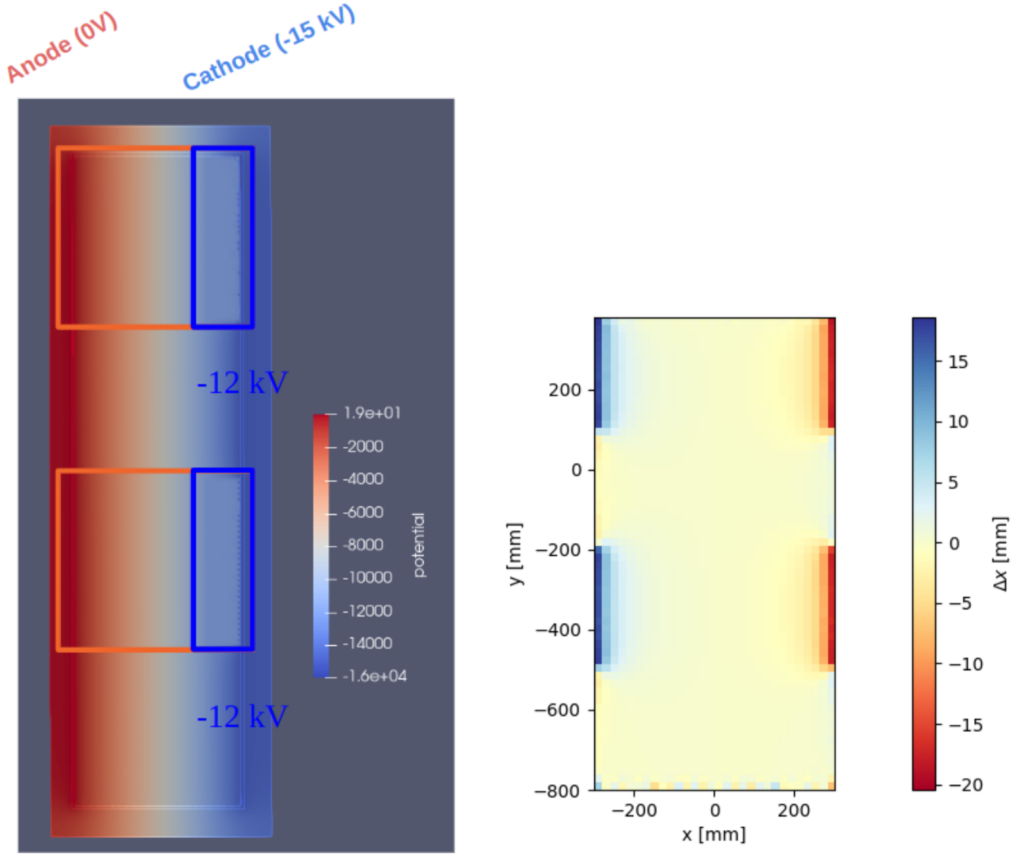

Figure 7.17: Drift potential (left) on a slice of the fiducial volume near to the light readout systems ($x \approx -300mm$) with an artificially raised surface near the cathode on the LCM surfaces. The resulting displacement map (right) shows a repulsive behavior which is of a similar magnitude to what is seen in the Module0/Module1 data.

expected to produce a potential on the surface of these modules which is offset from the gradient otherwise produced by the field shaping elements. It is seen that a surface potential of -12 kV on a portion of the LCM tiles nearest to the cathode can approximately reproduce the inwards deflection effect shown by many of the LCM tiles in Module0/Module1 data.

The results of these studies have been submitted to the DUNE LAr-ND consortium for review and will inform design choices for detector prototypes going forward. These maps and the associated analysis will also form a framework for spatial correction of

deposited charges as an input to reconstruction of particles and higher-level physics analysis of neutrino signals.

CHAPTER VIII

Summary

The DUNE long-baseline neutrino experiment represents the culmination of many decades of theoretical and experimental work in the fields of high-energy physics. It promises to shed light on the most rare processes described by the Standard Model in order to understand the holes in our current understanding of the universe, and in the process, patch them up. DUNE will unambiguously measure the true ordering of the neutrino masses, a long-standing problem deeply connected to the origins of mass. DUNE will also present unprecedented sensitivity to the ability for neutrino oscillation to violate CP-symmetry, which is a key feature of the evolution of the early universe.

This thesis has shown that DUNE's generational step forward in precision is greatly dependent upon a robust and well-understood near detector program. The DUNE near detector system will take advantage of several new technologies within the LArTPC paradigm, as well as new techniques to augment the long-baseline oscillation experimental design.

The DUNE ND system will make use of the PRISM technique, an off-axis motion system by which the two upstream ND components will move transverse to the axis of the neutrino beam. This motion allows for sampling of the flux across a large portion of the angular spectrum, granting it the ability to disentangle system-

atic uncertainties of beam production and neutrino-target interactions. Furthermore, this transverse motion enables unique long-baseline analysis techniques, namely the linear-combination analysis, which can drastically reduce the dependence of oscillation measurements on these systematics and improve sensitivity to difficult to measure regions of the parameter space such as θ_{23}.

The DUNE ND-LAr subdetector will feature a unique modular design with low-profile field shaping elements, pixelated charge readout systems, and efficient low-profile light collection systems. It will also feature a laser photoelectric charge injection system for on-demand calibration measurements of the drift field. The need for a purpose-built calibration system is demonstrated by the observed deformities due to both the well-understood design compromises, and the as of yet not understood defects which seem to result from elements of the light readout system. These aspects, combined with the additional agitation of repeated motion, make a clear case for a system which is able to asses the quality of field shaping on very short timescales.

APPENDICES

APPENDIX A

Displacement Maps

This appendix includes more slices and projections of the Module-0 and Module-1 displacement maps introduced in Chapter VII.

A.1 Module-0

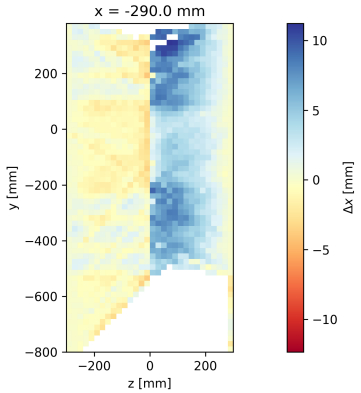
x = -290.0 mm
y [mm]
z [mm]
Δx [mm]

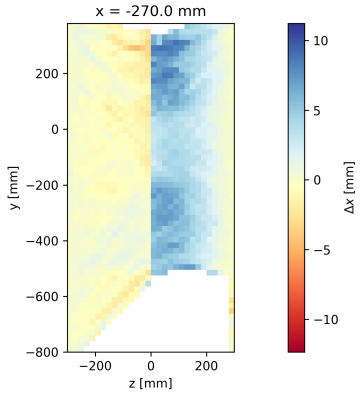
x = -270.0 mm
y [mm]
z [mm]
Δx [mm]

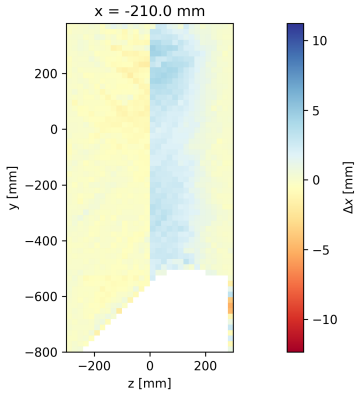
x = -210.0 mm
y [mm]
z [mm]
Δx [mm]

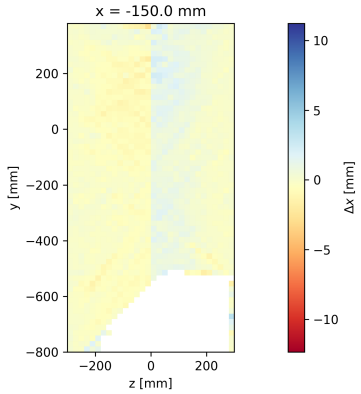
x = -150.0 mm
y [mm]
z [mm]
Δx [mm]

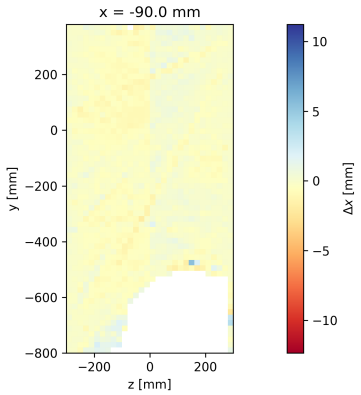
x = -90.0 mm
y [mm]
z [mm]
Δx [mm]

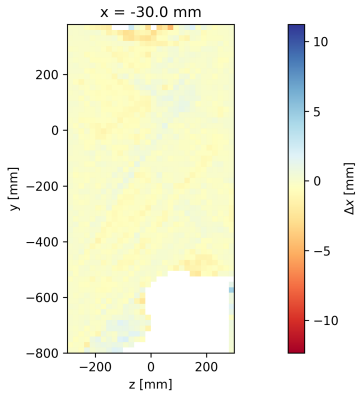
x = -30.0 mm
y [mm]
z [mm]
Δx [mm]

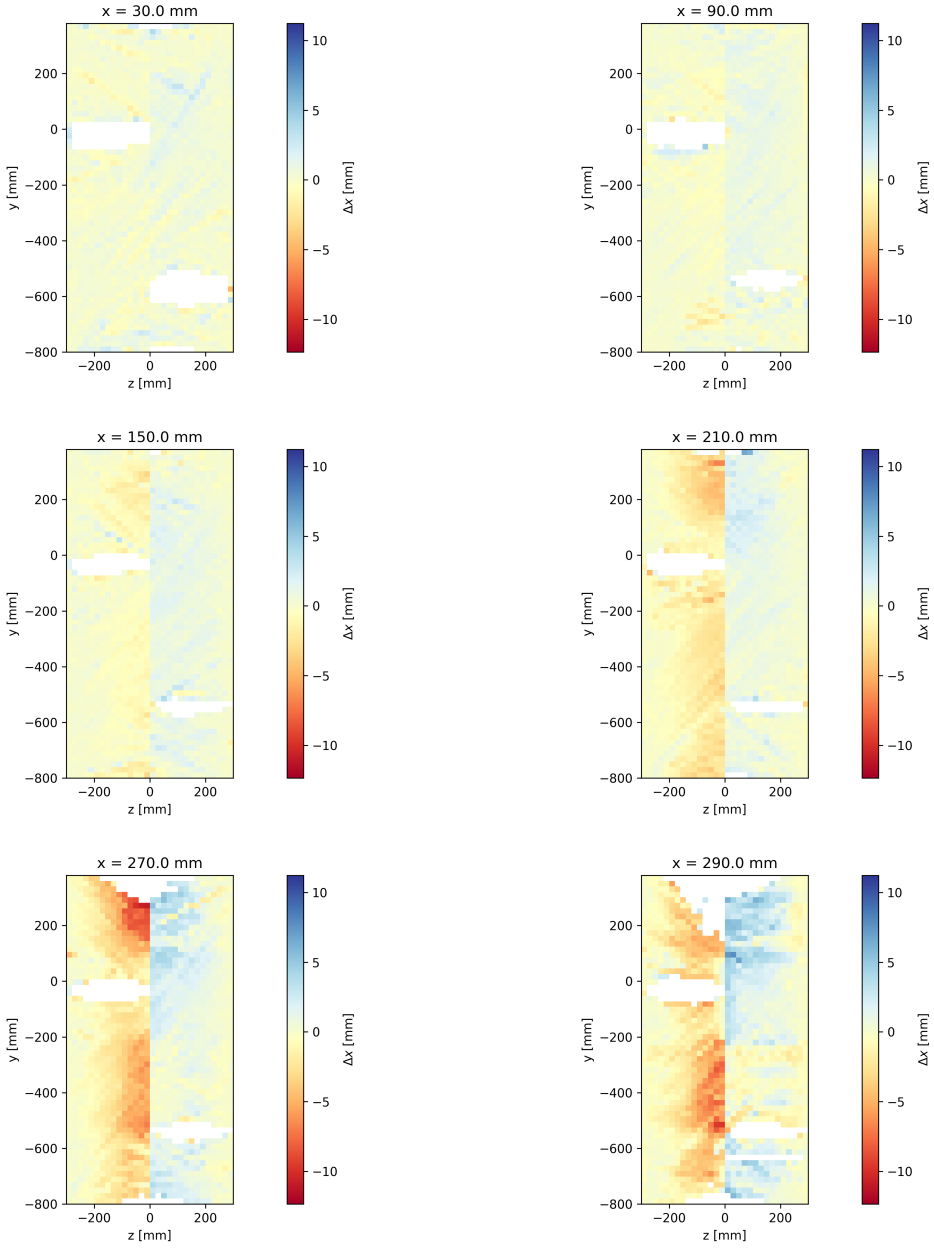
x = 30.0 mm
x = 90.0 mm
x = 150.0 mm
x = 210.0 mm
x = 270.0 mm
x = 290.0 mm
y [mm]
z [mm]
Δx [mm]
200
0
−200
−400
−600
−800
10
5
0
−5
−10

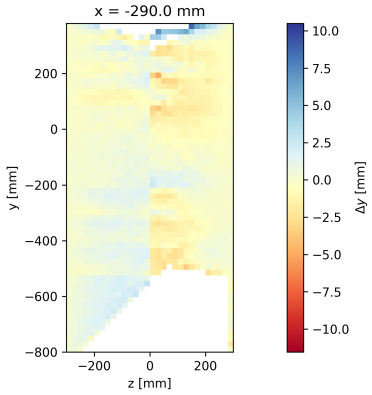
x = -290.0 mm
y [mm]
z [mm]
Δy [mm]

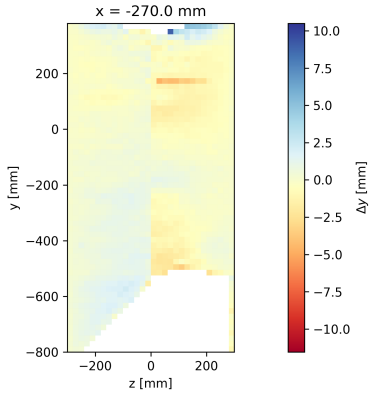
x = -270.0 mm
y [mm]
z [mm]
Δy [mm]

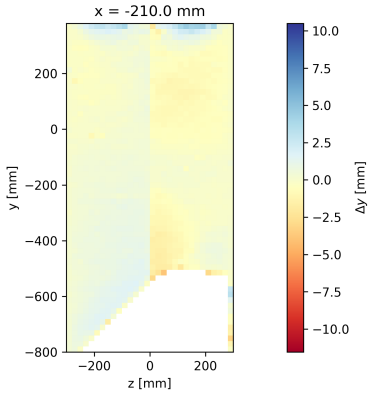
x = -210.0 mm
y [mm]
z [mm]
Δy [mm]

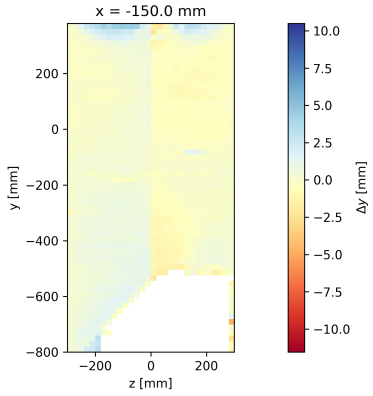
x = -150.0 mm
y [mm]
z [mm]
Δy [mm]

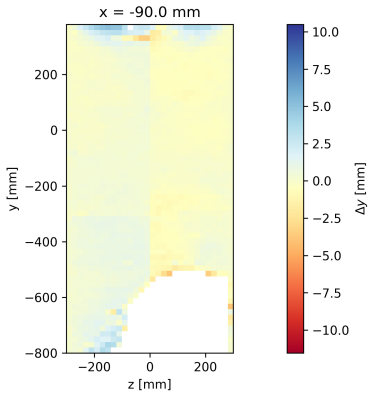
x = -90.0 mm
y [mm]
z [mm]
Δy [mm]

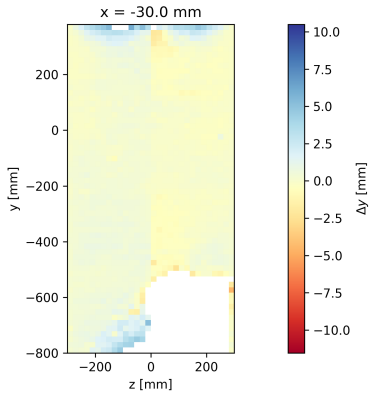
x = -30.0 mm
y [mm]
z [mm]
Δy [mm]

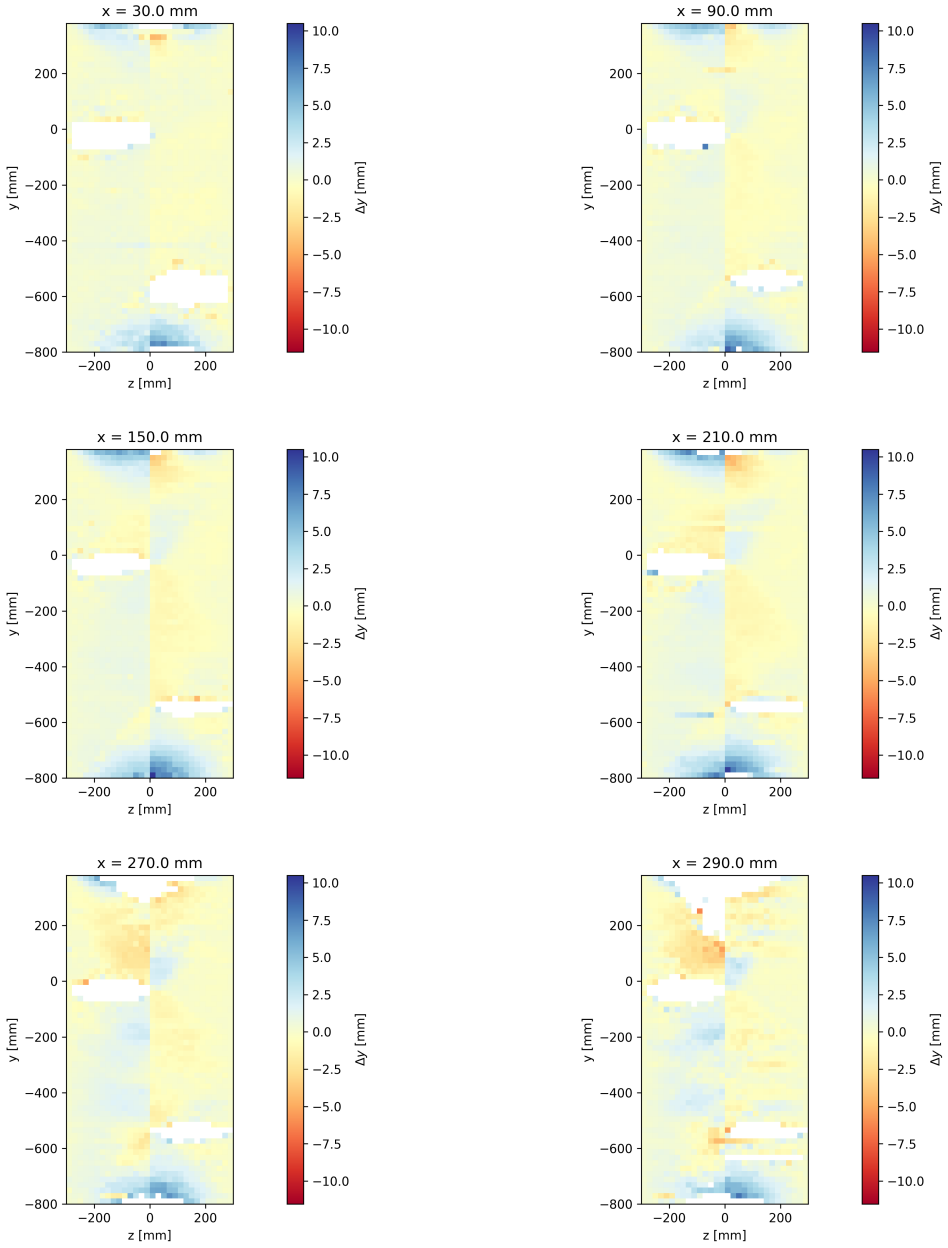
x = 30.0 mm
x = 90.0 mm
x = 150.0 mm
x = 210.0 mm
x = 270.0 mm
x = 290.0 mm
y [mm]
z [mm]
Δy [mm]
200
0
−200
−400
−600
−800
10.0
7.5
5.0
2.5
0.0
−2.5
−5.0
−7.5
−10.0

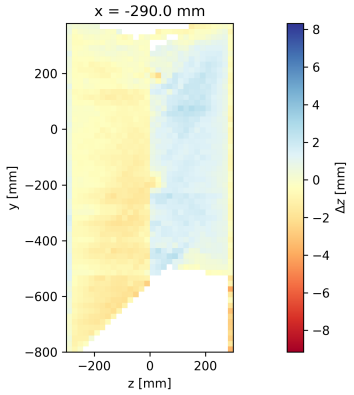
x = -290.0 mm
y [mm]
z [mm]
Δz [mm]

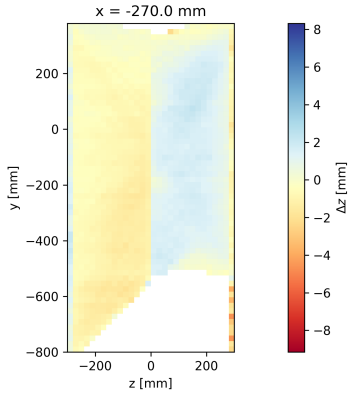
x = -270.0 mm
y [mm]
z [mm]
Δz [mm]

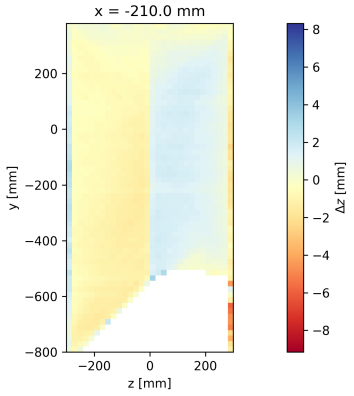
x = -210.0 mm
y [mm]
z [mm]
Δz [mm]

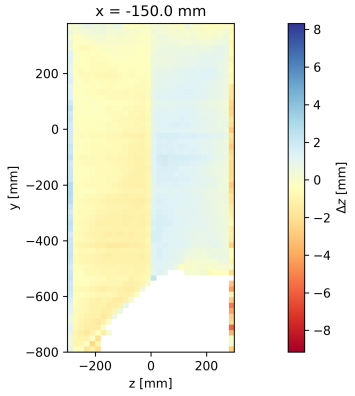
x = -150.0 mm
y [mm]
z [mm]
Δz [mm]

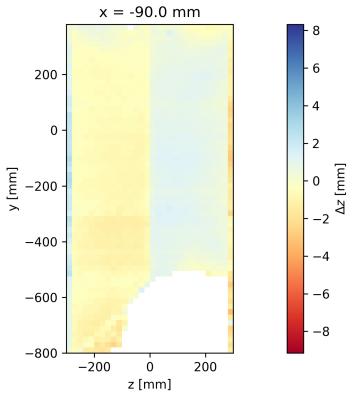
x = -90.0 mm
y [mm]
z [mm]
Δz [mm]

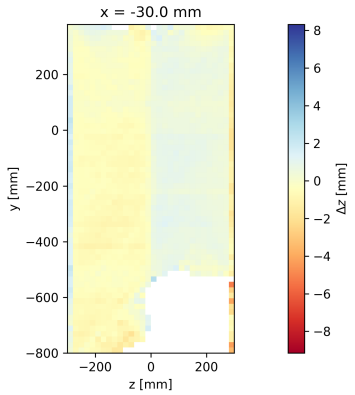
x = -30.0 mm
y [mm]
z [mm]
Δz [mm]

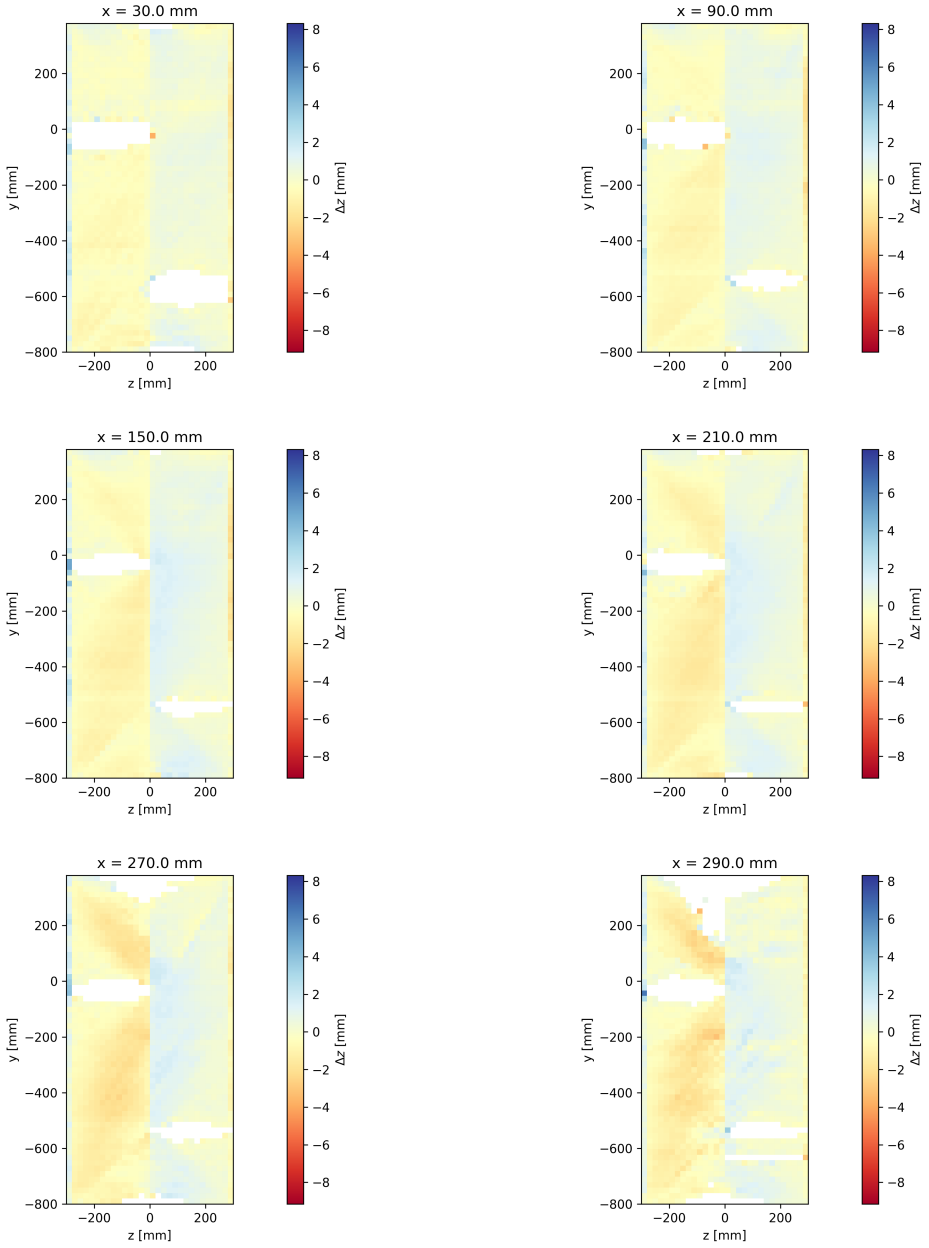
x = 30.0 mm
x = 90.0 mm
x = 150.0 mm
x = 210.0 mm
x = 270.0 mm
x = 290.0 mm
y [mm]
z [mm]
Δz [mm]
200
0
−200
−400
−600
−800
8
6
4
2
0
−2
−4
−6
−8

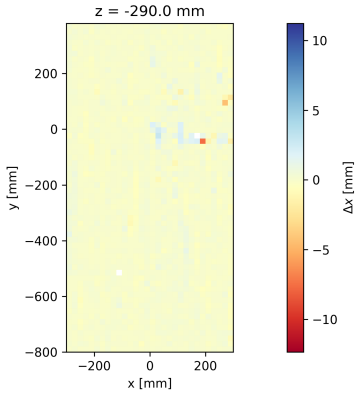
z = -290.0 mm
y [mm]
x [mm]
Δx [mm]

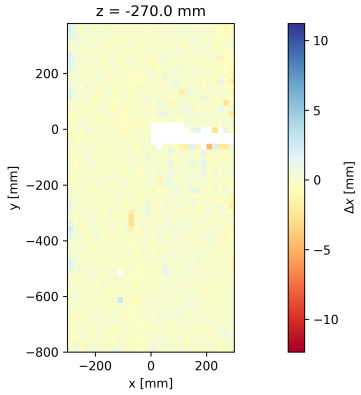
z = -270.0 mm
y [mm]
x [mm]
Δx [mm]

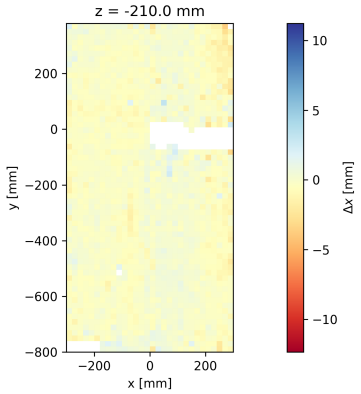
z = -210.0 mm
y [mm]
x [mm]
Δx [mm]

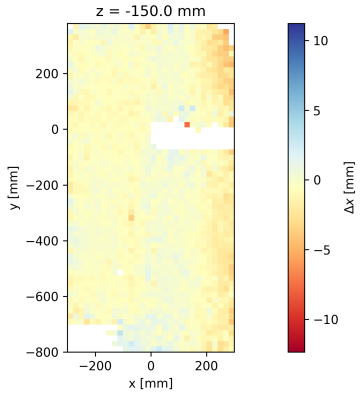
z = -150.0 mm
y [mm]
x [mm]
Δx [mm]

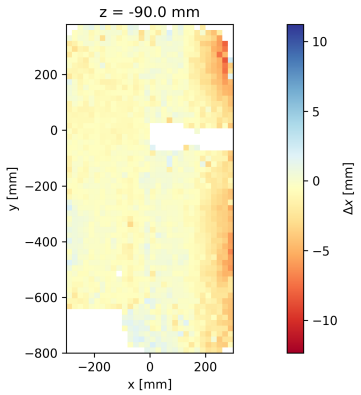
z = -90.0 mm
y [mm]
x [mm]
Δx [mm]

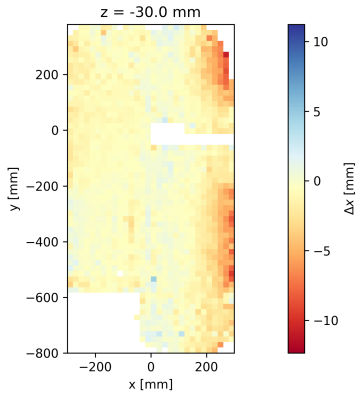
z = -30.0 mm
y [mm]
x [mm]
Δx [mm]

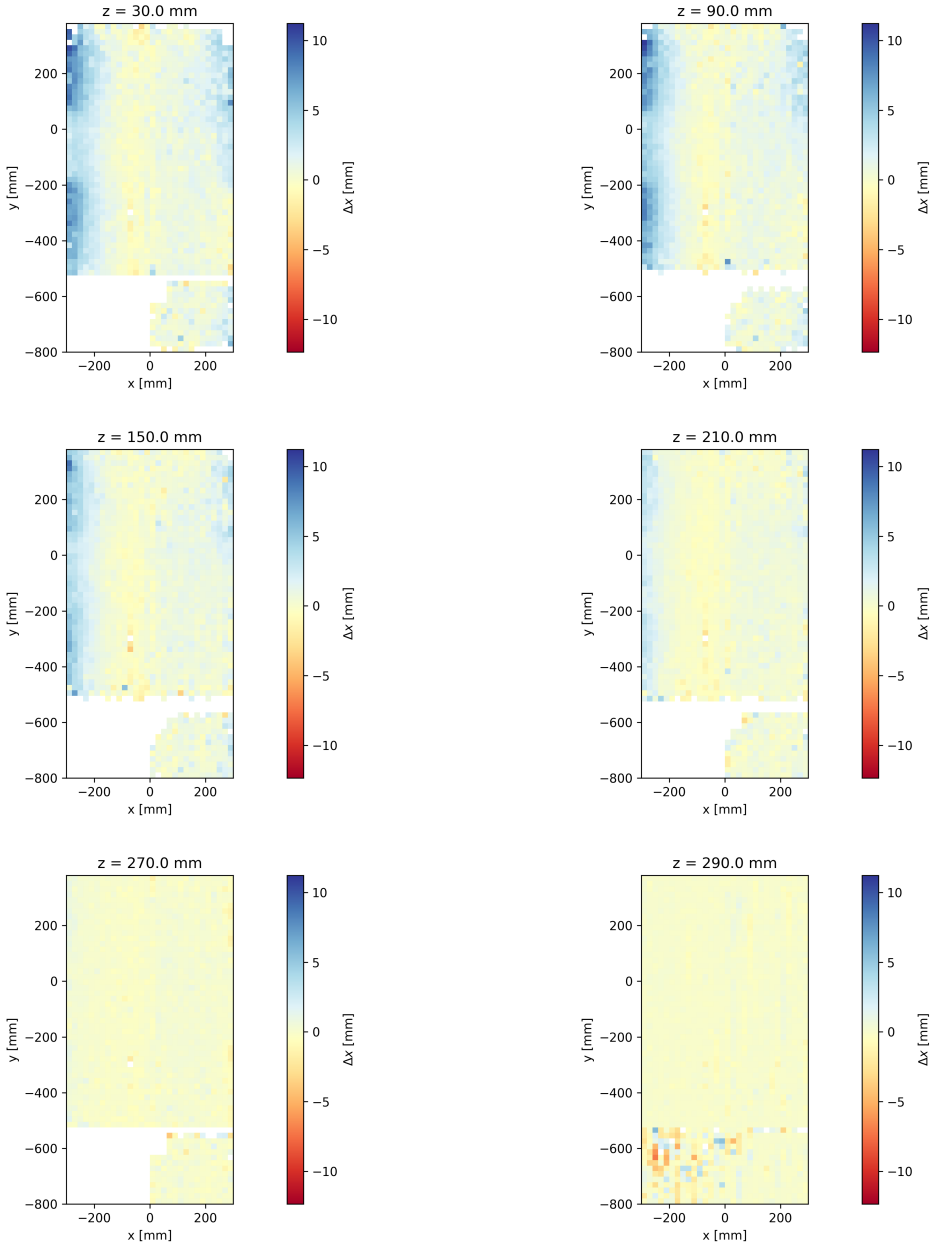
z = 30.0 mm
z = 90.0 mm
z = 150.0 mm
z = 210.0 mm
z = 270.0 mm
z = 290.0 mm
x [mm]
y [mm]
Δx [mm]
200
0
−200
−400
−600
−800
10
5
0
−5
−10

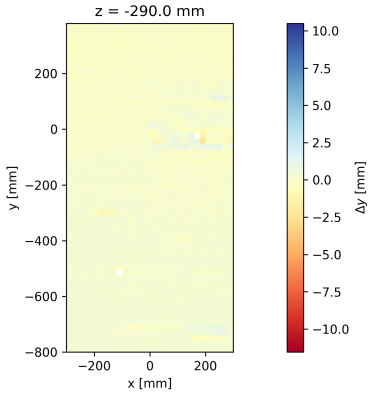
z = -290.0 mm
y [mm]
x [mm]
Δy [mm]

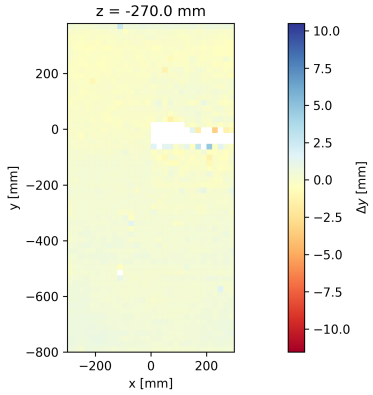
z = -270.0 mm
y [mm]
x [mm]
Δy [mm]

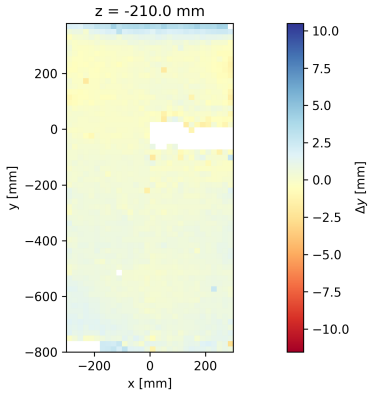
z = -210.0 mm
y [mm]
x [mm]
Δy [mm]

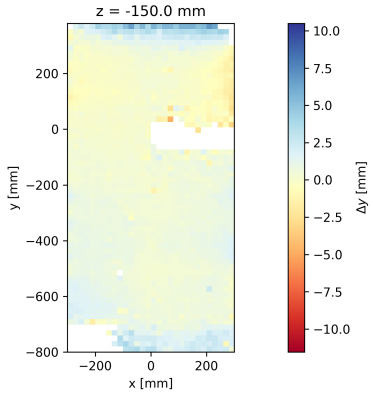
z = -150.0 mm
y [mm]
x [mm]
Δy [mm]

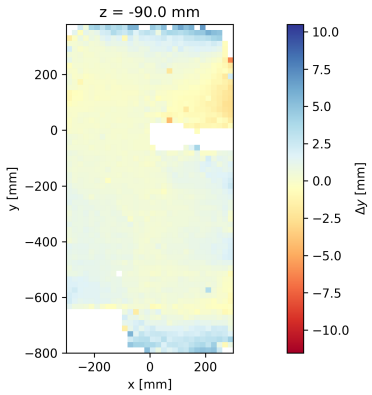
z = -90.0 mm
y [mm]
x [mm]
Δy [mm]

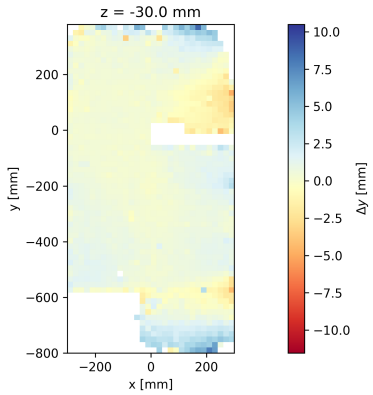
z = -30.0 mm
y [mm]
x [mm]
Δy [mm]

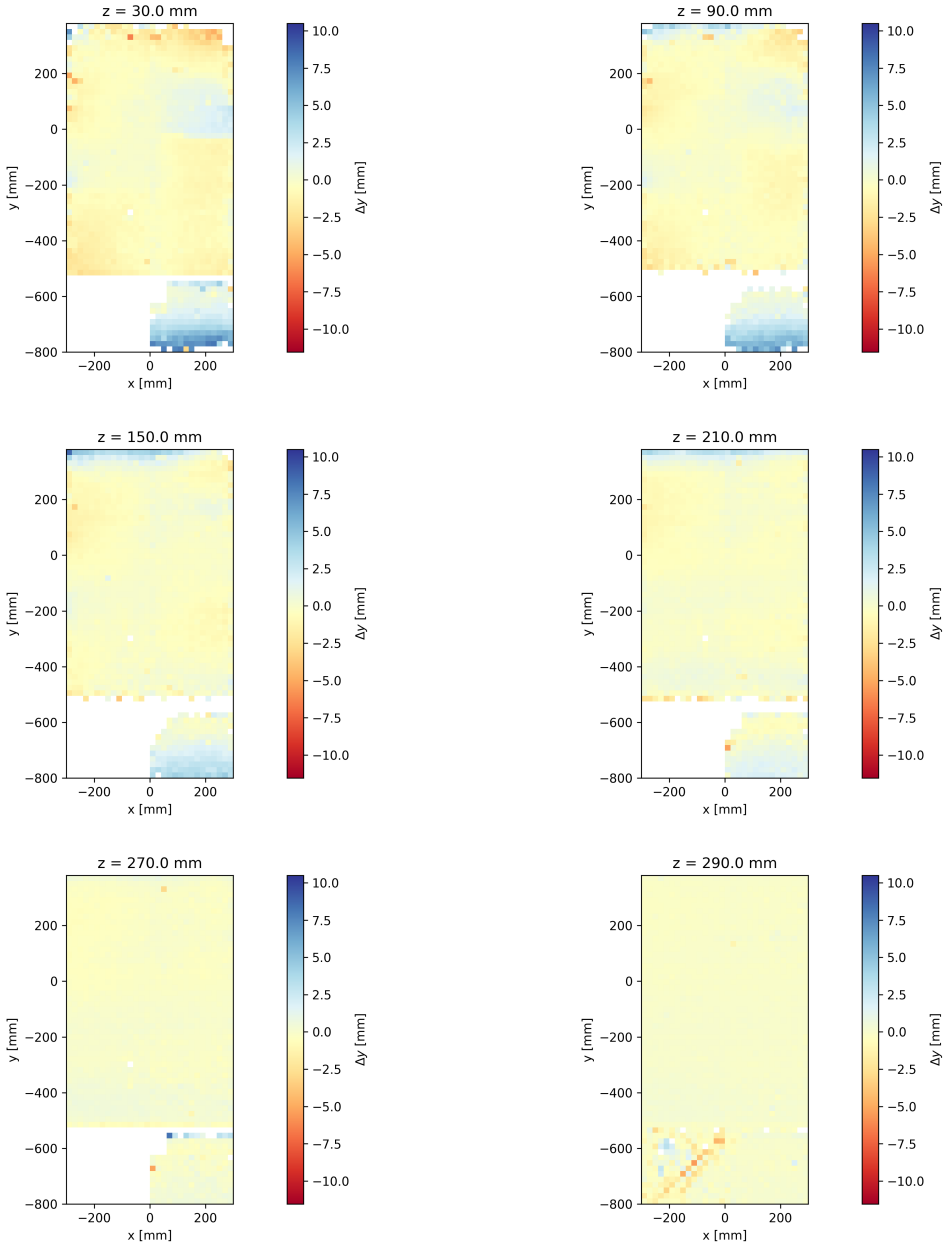
z = 30.0 mm
z = 90.0 mm
z = 150.0 mm
z = 210.0 mm
z = 270.0 mm
z = 290.0 mm
x [mm]
y [mm]
Δy [mm]
200
0
−200
−400
−600
−800
10.0
7.5
5.0
2.5
0.0
−2.5
−5.0
−7.5
−10.0

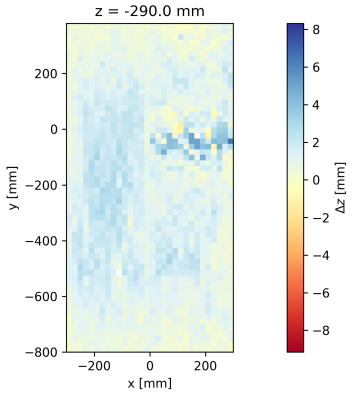
z = -290.0 mm
y [mm]
x [mm]
Δz [mm]

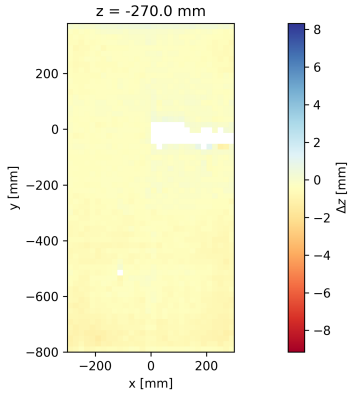
z = -270.0 mm
y [mm]
x [mm]
Δz [mm]

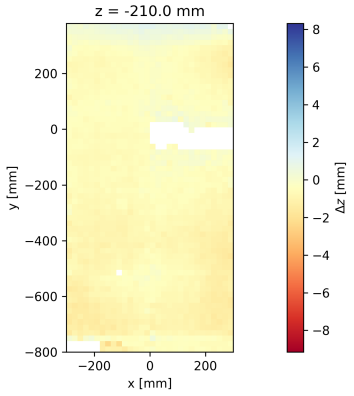
z = -210.0 mm
y [mm]
x [mm]
Δz [mm]

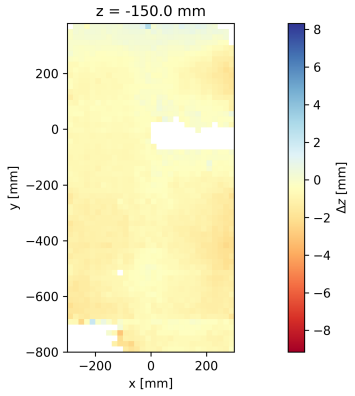
z = -150.0 mm
y [mm]
x [mm]
Δz [mm]

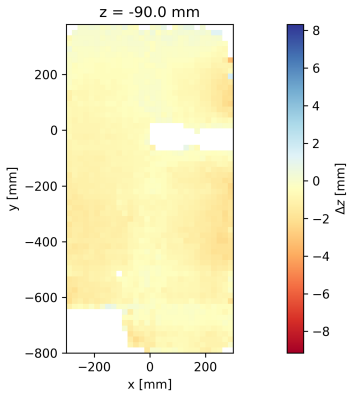
z = -90.0 mm
y [mm]
x [mm]
Δz [mm]

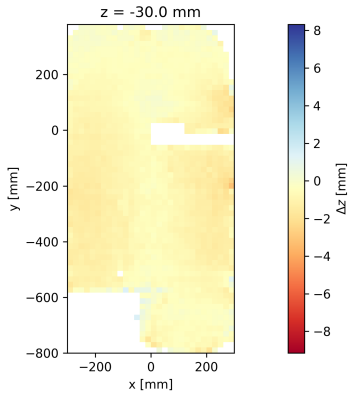
z = -30.0 mm
y [mm]
x [mm]
Δz [mm]

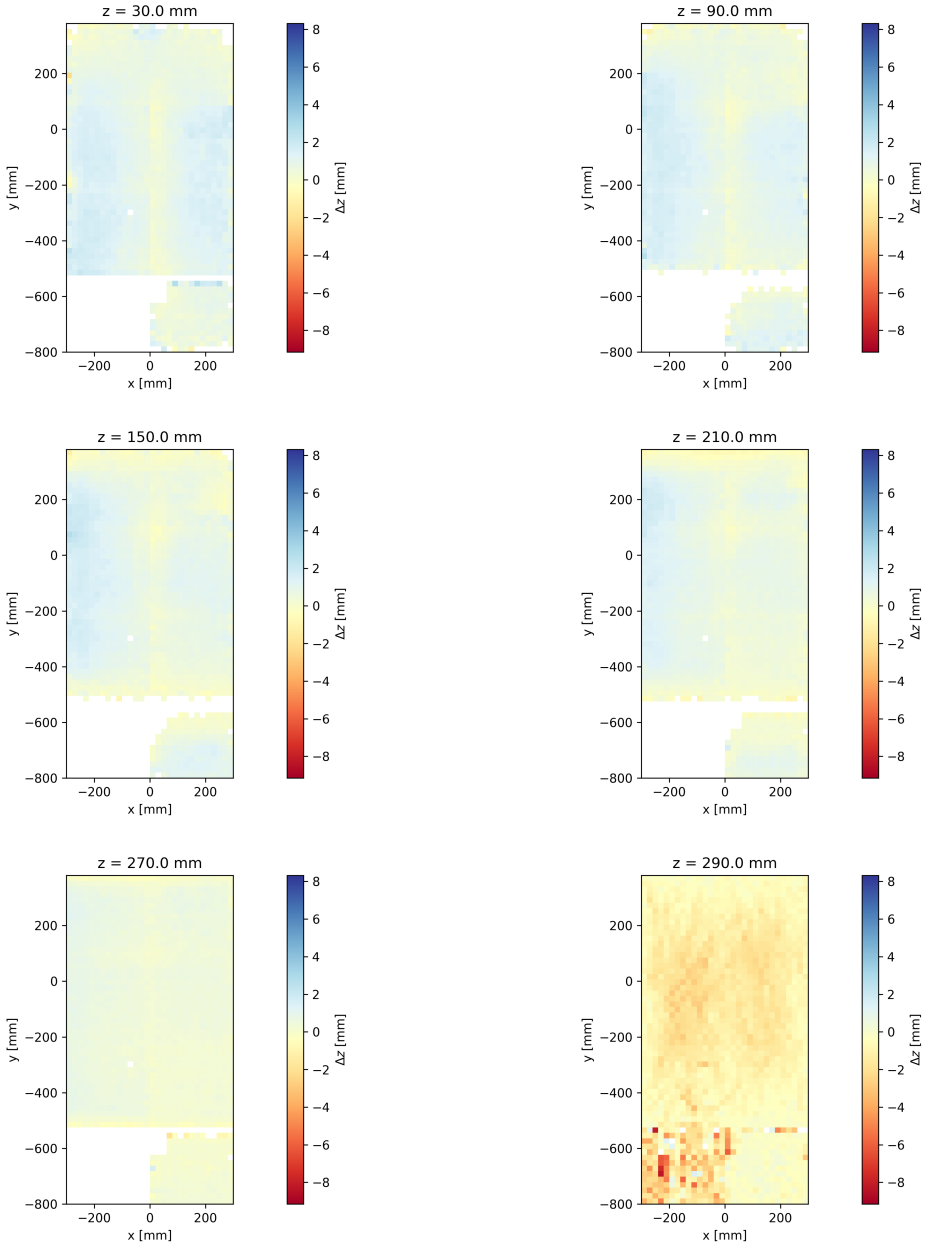
z = 30.0 mm
z = 90.0 mm
z = 150.0 mm
z = 210.0 mm
z = 270.0 mm
z = 290.0 mm
x [mm]
y [mm]
Δz [mm]

A.2 Module-1

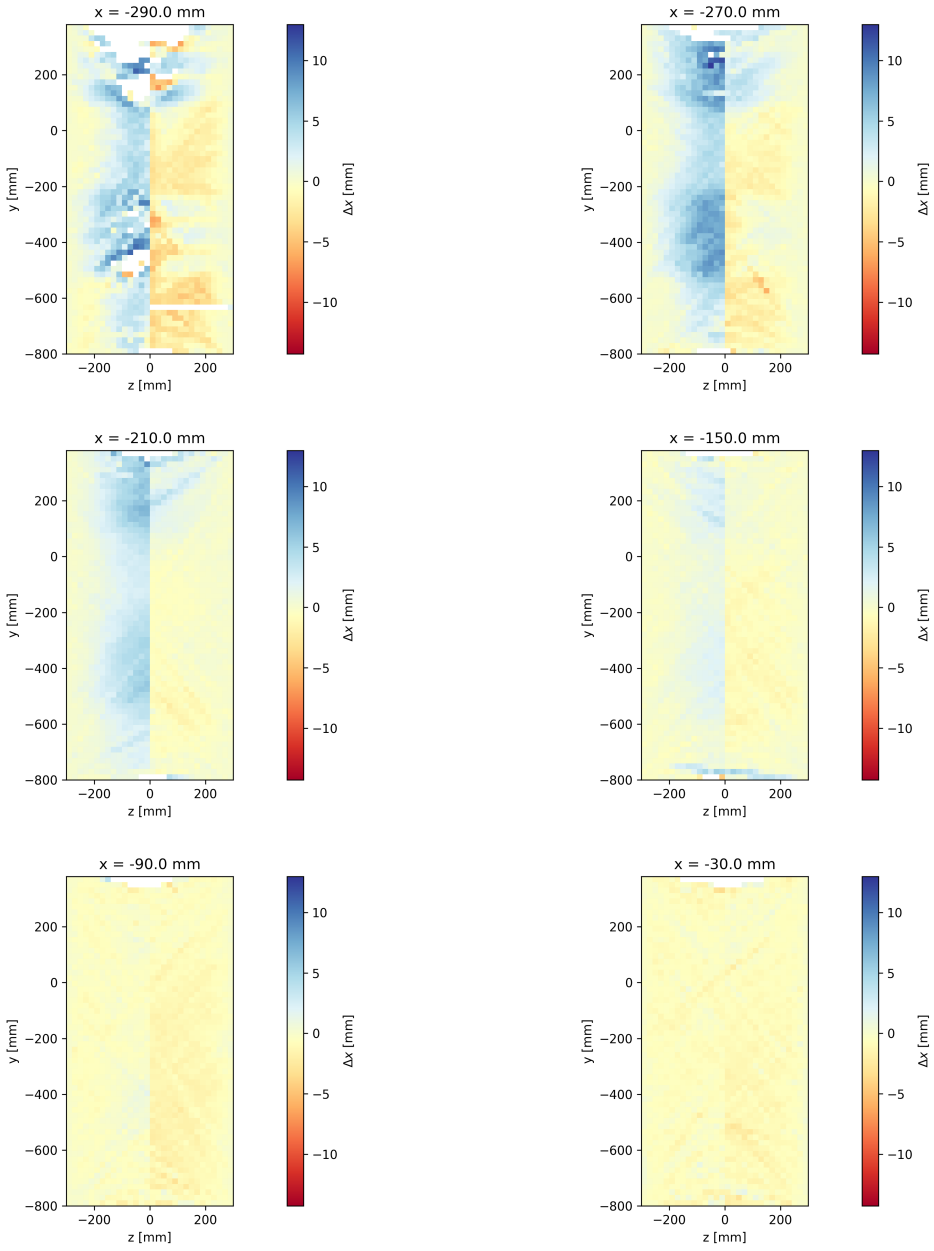
x = -290.0 mm
x = -270.0 mm
x = -210.0 mm
x = -150.0 mm
x = -90.0 mm
x = -30.0 mm
y [mm]
z [mm]
Δx [mm]

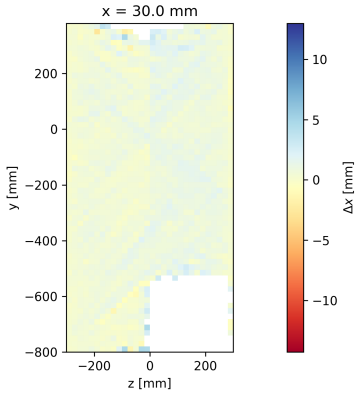
x = 30.0 mm
y [mm]
z [mm]
Δx [mm]

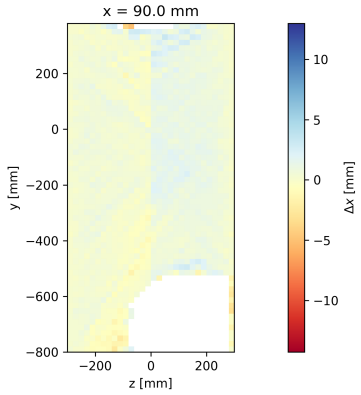
x = 90.0 mm
y [mm]
z [mm]
Δx [mm]

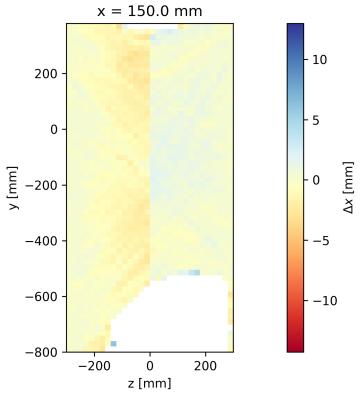
x = 150.0 mm
y [mm]
z [mm]
Δx [mm]

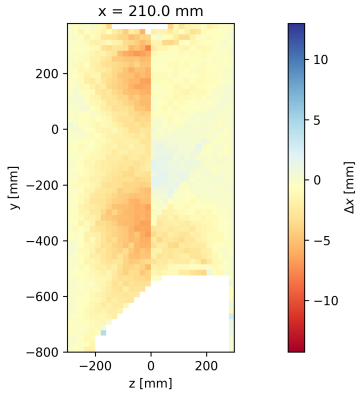
x = 210.0 mm
y [mm]
z [mm]
Δx [mm]

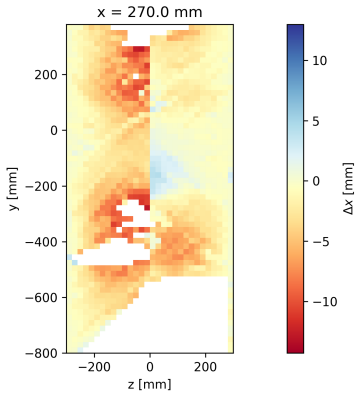
x = 270.0 mm
y [mm]
z [mm]
Δx [mm]

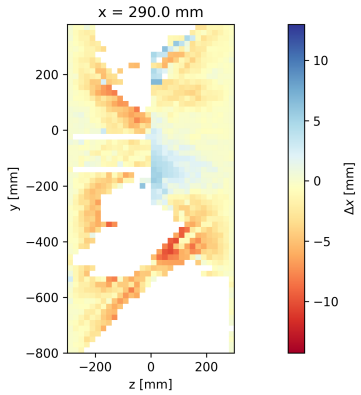
x = 290.0 mm
y [mm]
z [mm]
Δx [mm]

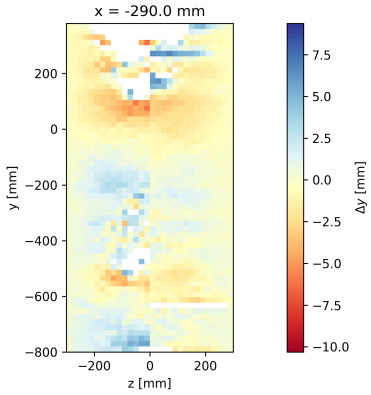
x = -290.0 mm
y [mm]
z [mm]
Δy [mm]

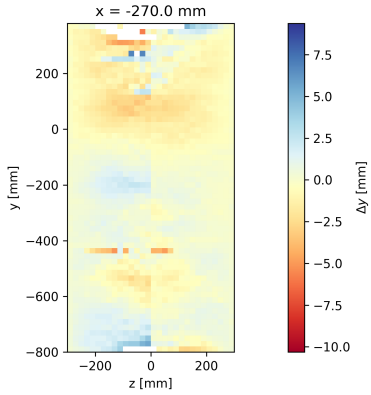
x = -270.0 mm
y [mm]
z [mm]
Δy [mm]

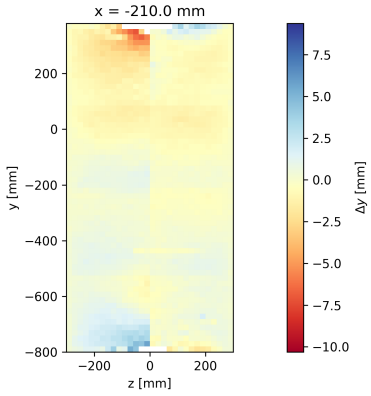
x = -210.0 mm
y [mm]
z [mm]
Δy [mm]

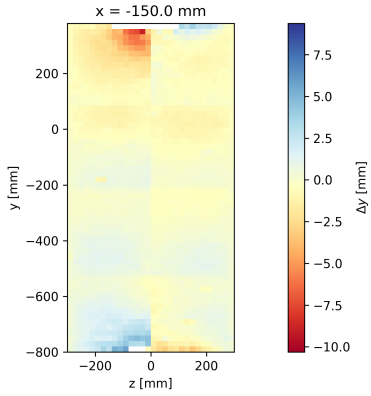
x = -150.0 mm
y [mm]
z [mm]
Δy [mm]

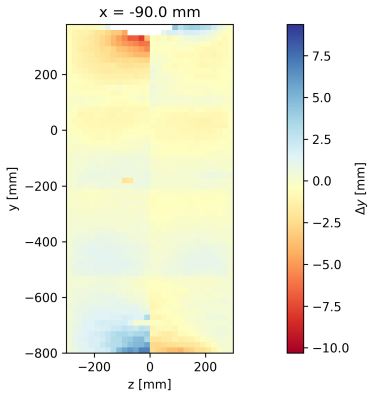
x = -90.0 mm
y [mm]
z [mm]
Δy [mm]

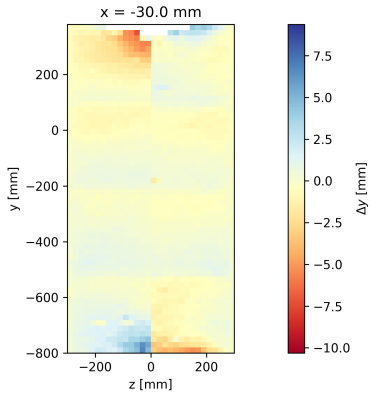
x = -30.0 mm
y [mm]
z [mm]
Δy [mm]

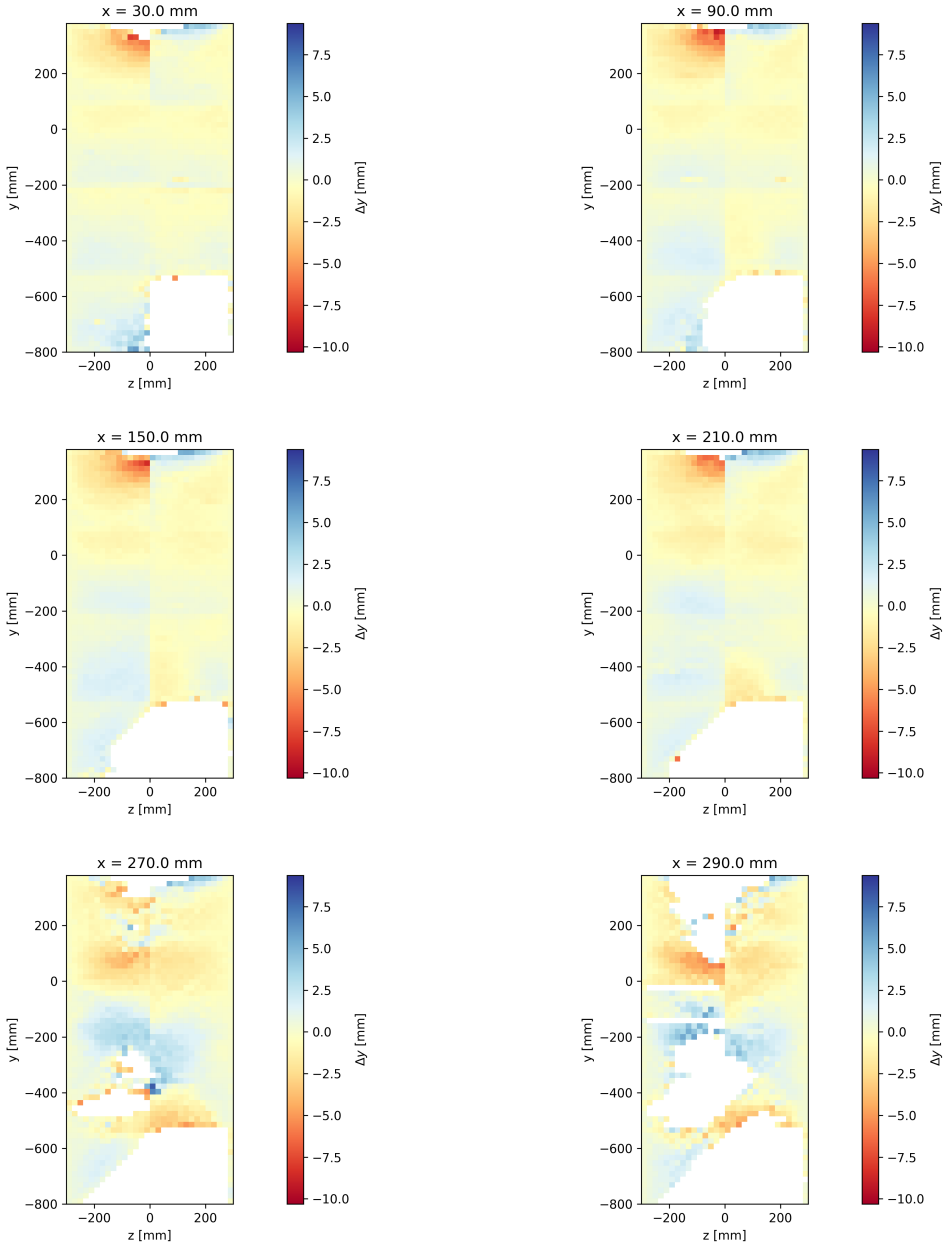
x = 30.0 mm
x = 90.0 mm
x = 150.0 mm
x = 210.0 mm
x = 270.0 mm
x = 290.0 mm
y [mm]
z [mm]
Δy [mm]
200
0
−200
−400
−600
−800
−200
0
200
7.5
5.0
2.5
0.0
−2.5
−5.0
−7.5
−10.0

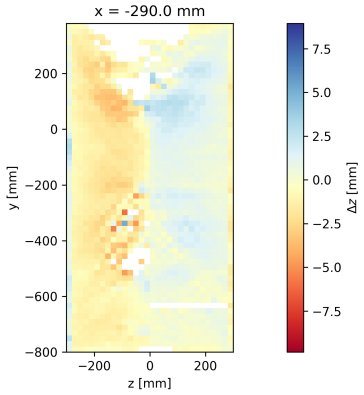
x = -290.0 mm
y [mm]
z [mm]
Δz [mm]

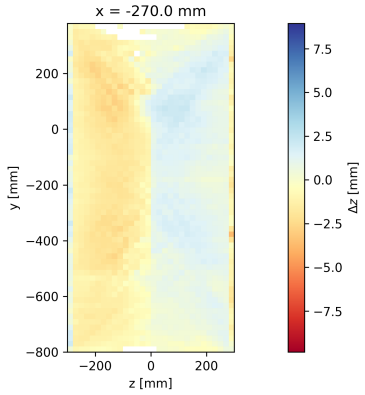
x = -270.0 mm
y [mm]
z [mm]
Δz [mm]

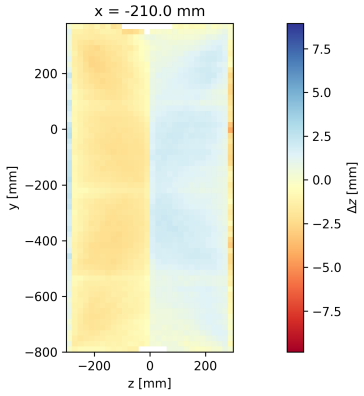
x = -210.0 mm
y [mm]
z [mm]
Δz [mm]

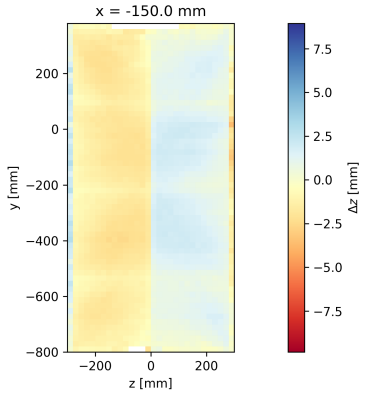
x = -150.0 mm
y [mm]
z [mm]
Δz [mm]

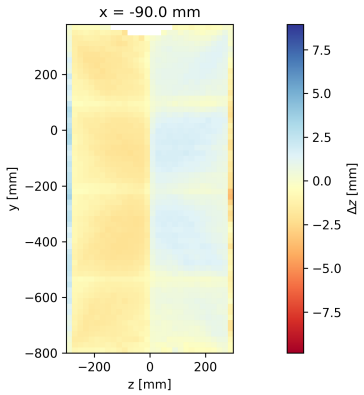
x = -90.0 mm
y [mm]
z [mm]
Δz [mm]

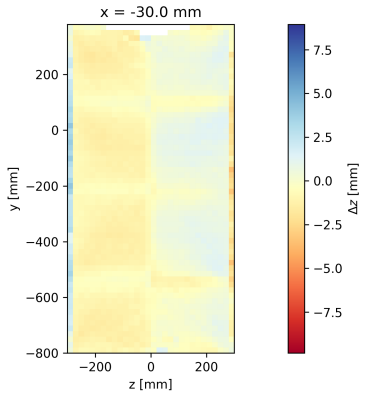
x = -30.0 mm
y [mm]
z [mm]
Δz [mm]

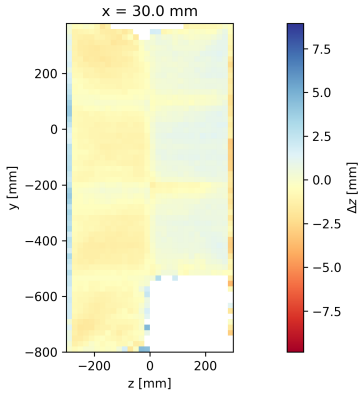
x = 30.0 mm
y [mm]
z [mm]
Δz [mm]

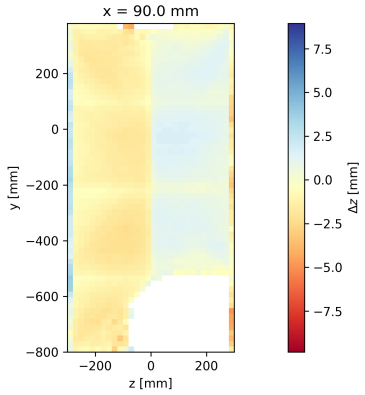
x = 90.0 mm
y [mm]
z [mm]
Δz [mm]

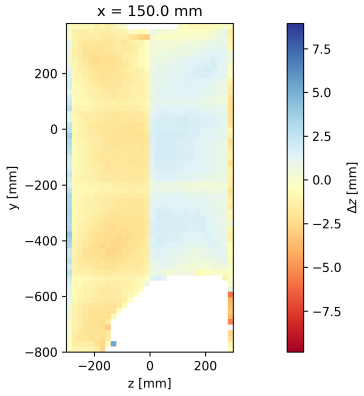
x = 150.0 mm
y [mm]
z [mm]
Δz [mm]

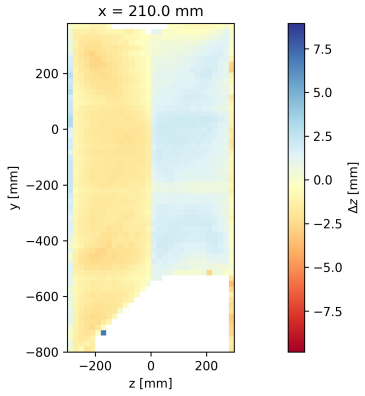
x = 210.0 mm
y [mm]
z [mm]
Δz [mm]

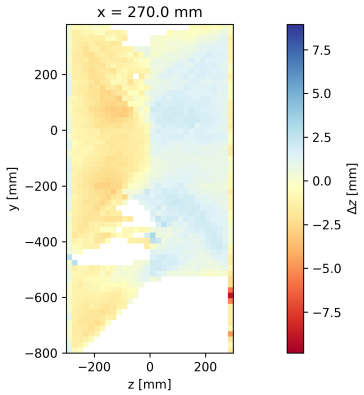
x = 270.0 mm
y [mm]
z [mm]
Δz [mm]

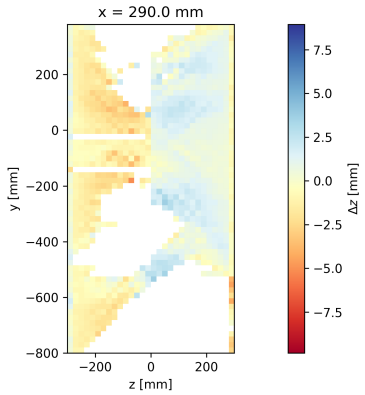
x = 290.0 mm
y [mm]
z [mm]
Δz [mm]

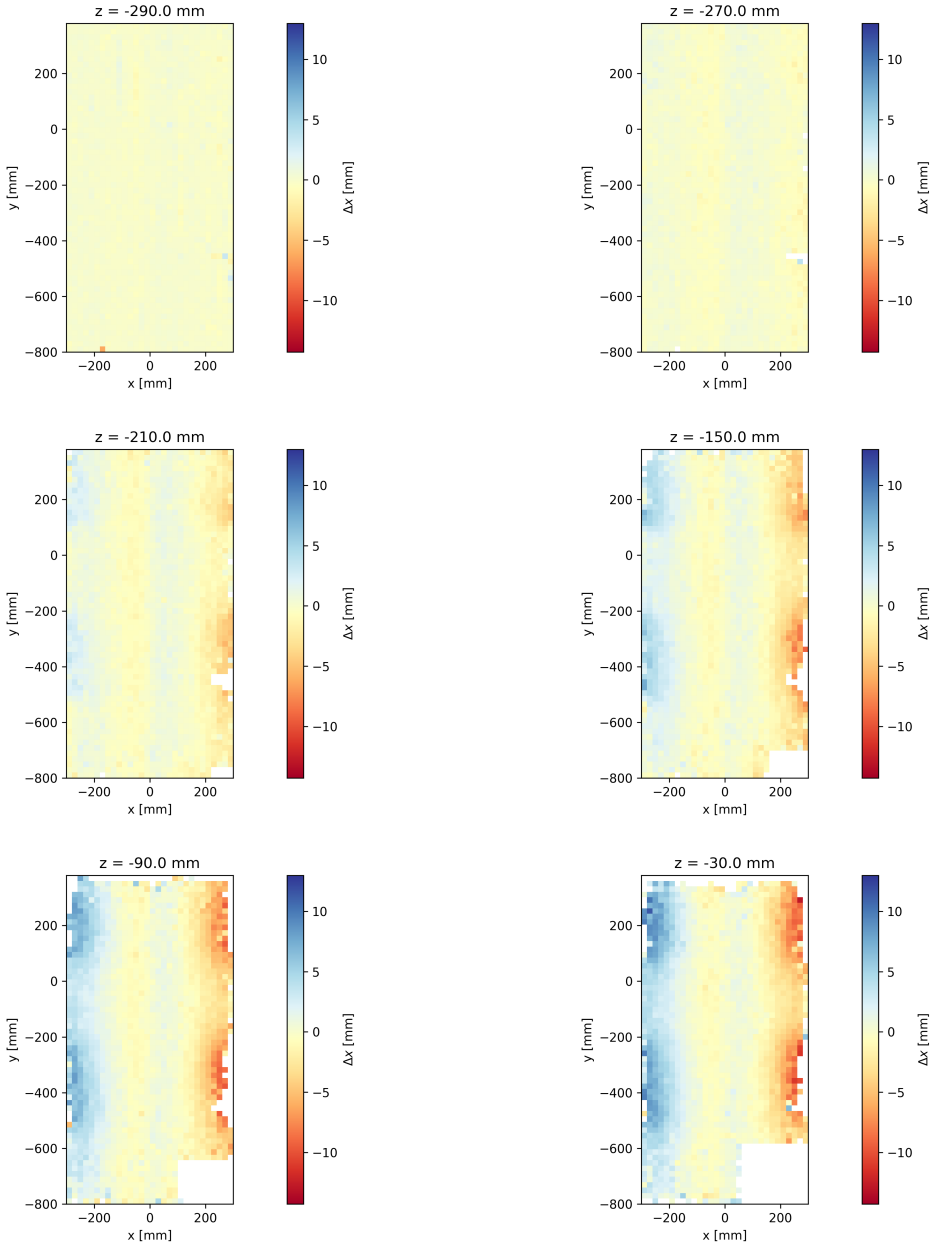
z = -290.0 mm
z = -270.0 mm
z = -210.0 mm
z = -150.0 mm
z = -90.0 mm
z = -30.0 mm
x [mm]
y [mm]
Δx [mm]
200
0
−200
−400
−600
−800
10
5
0
−5
−10

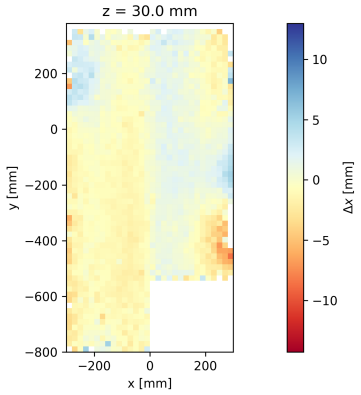
z = 30.0 mm
y [mm]
x [mm]
Δx [mm]

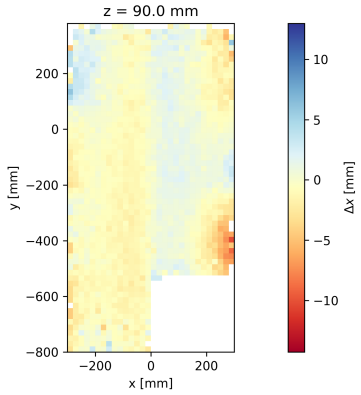
z = 90.0 mm
y [mm]
x [mm]
Δx [mm]

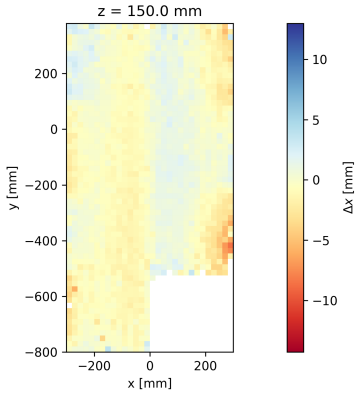
z = 150.0 mm
y [mm]
x [mm]
Δx [mm]

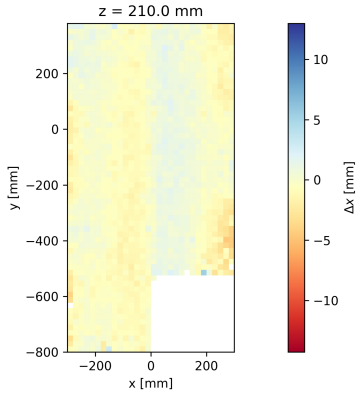
z = 210.0 mm
y [mm]
x [mm]
Δx [mm]

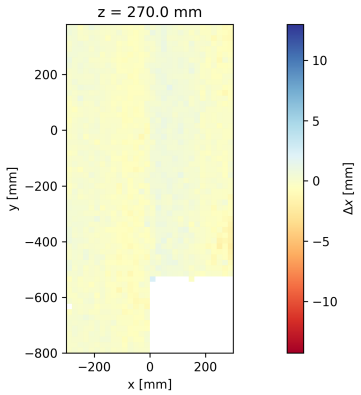
z = 270.0 mm
y [mm]
x [mm]
Δx [mm]

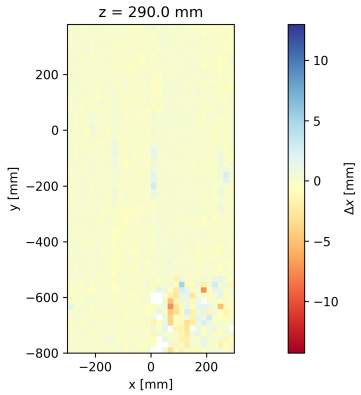
z = 290.0 mm
y [mm]
x [mm]
Δx [mm]

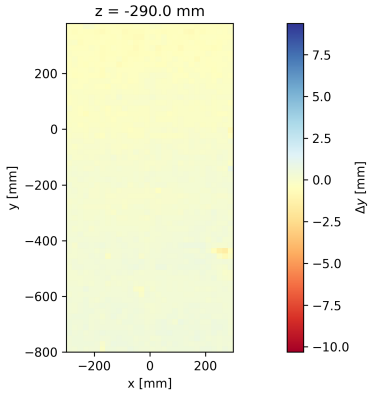
z = -290.0 mm
y [mm]
x [mm]
Δy [mm]

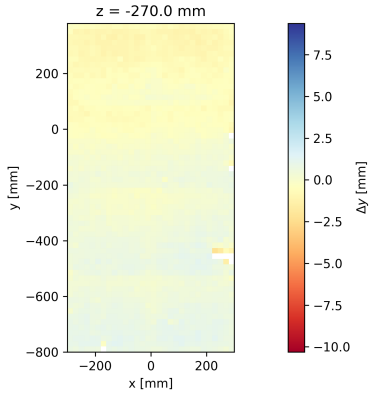
z = -270.0 mm
y [mm]
x [mm]
Δy [mm]

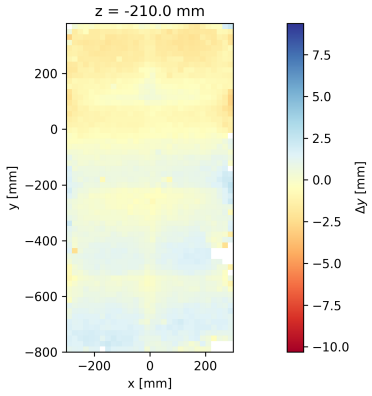
z = -210.0 mm
y [mm]
x [mm]
Δy [mm]

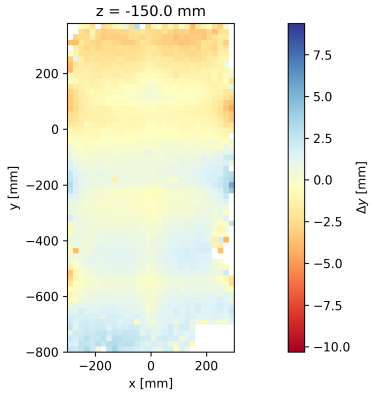
z = -150.0 mm
y [mm]
x [mm]
Δy [mm]

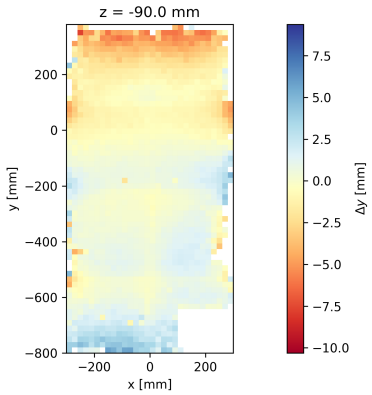
z = -90.0 mm
y [mm]
x [mm]
Δy [mm]

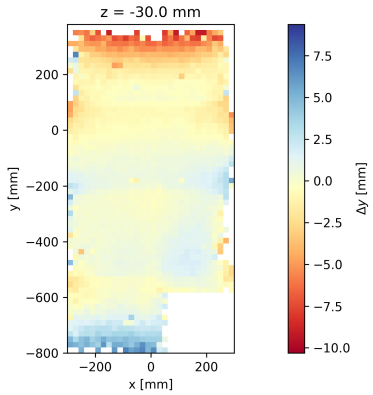
z = -30.0 mm
y [mm]
x [mm]
Δy [mm]

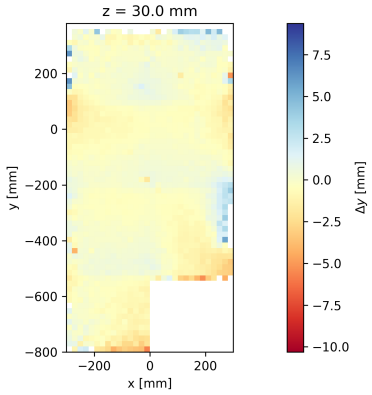
z = 30.0 mm
y [mm]
x [mm]
Δy [mm]

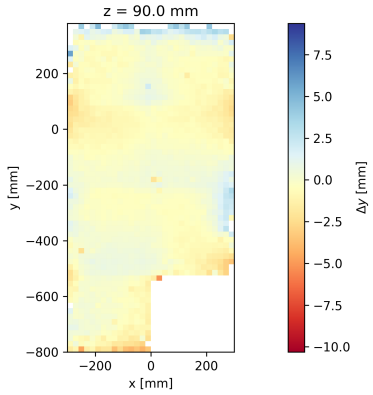
z = 90.0 mm
y [mm]
x [mm]
Δy [mm]

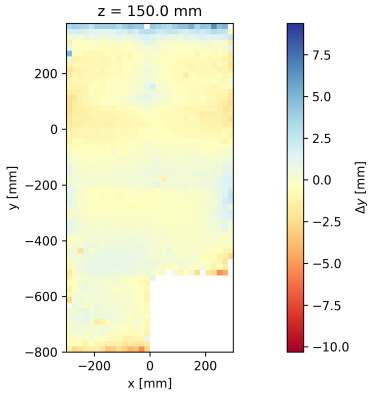
z = 150.0 mm
y [mm]
x [mm]
Δy [mm]

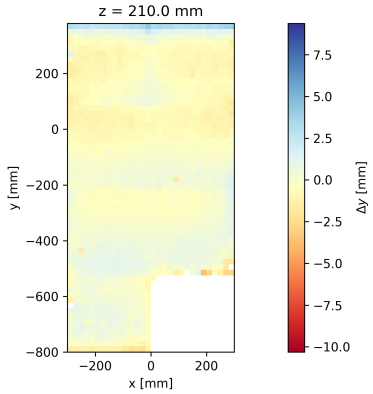
z = 210.0 mm
y [mm]
x [mm]
Δy [mm]

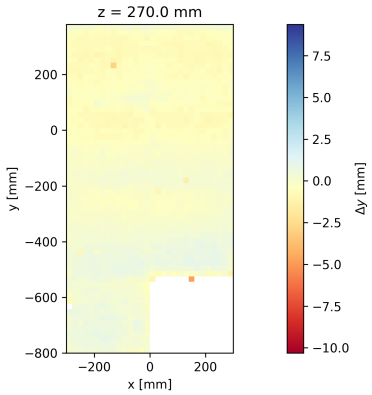
z = 270.0 mm
y [mm]
x [mm]
Δy [mm]

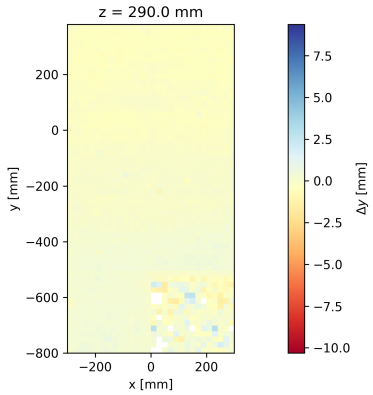
z = 290.0 mm
y [mm]
x [mm]
Δy [mm]

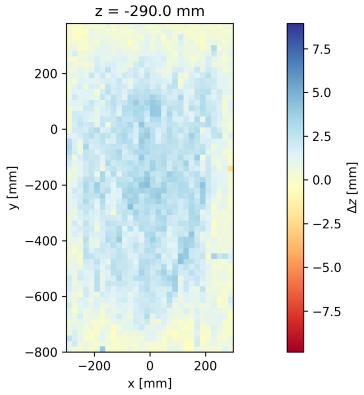
z = -290.0 mm
x [mm]
y [mm]
Δz [mm]

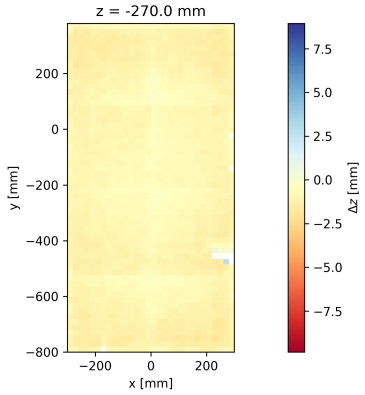
z = -270.0 mm
x [mm]
y [mm]
Δz [mm]

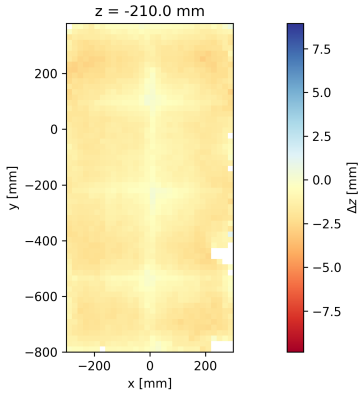
z = -210.0 mm
x [mm]
y [mm]
Δz [mm]

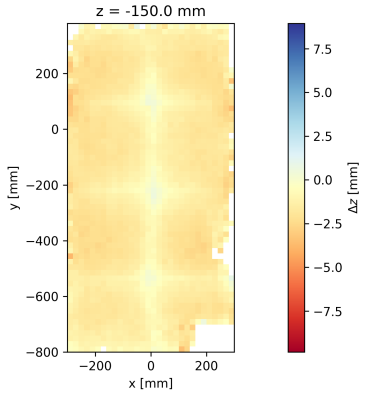
z = -150.0 mm
x [mm]
y [mm]
Δz [mm]

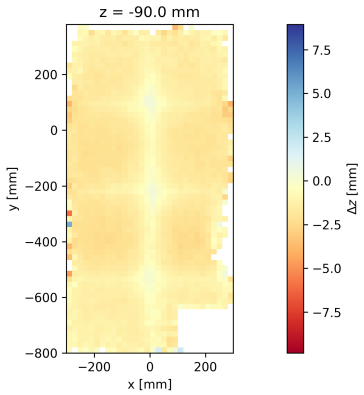
z = -90.0 mm
x [mm]
y [mm]
Δz [mm]

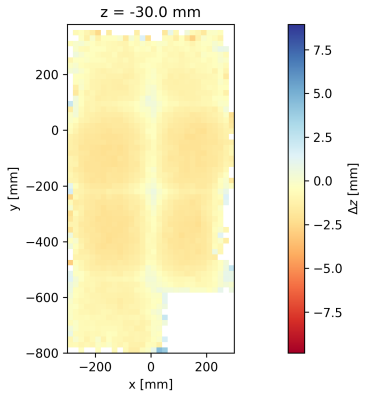
z = -30.0 mm
x [mm]
y [mm]
Δz [mm]

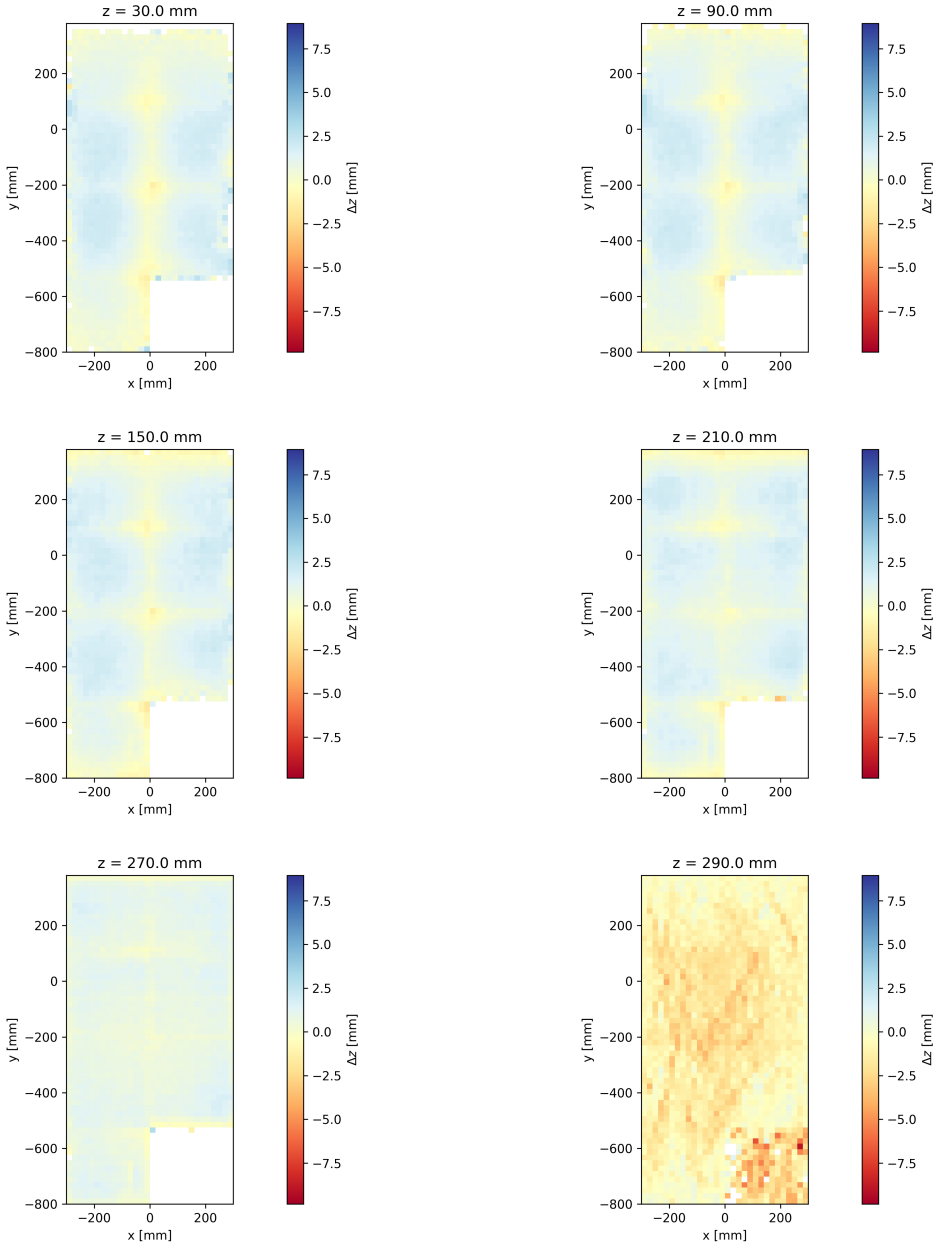
z = 30.0 mm
z = 90.0 mm
z = 150.0 mm
z = 210.0 mm
z = 270.0 mm
z = 290.0 mm
x [mm]
y [mm]
Δz [mm]
−200
0
200
200
0
−200
−400
−600
−800
7.5
5.0
2.5
0.0
−2.5
−5.0
−7.5

BIBLIOGRAPHY

BIBLIOGRAPHY

(), Hilman incorporated: Heavy load moving solutions.

Abi, B., et al. (2020a), Deep underground neutrino experiment (dune), far detector technical design report, volume i: Introduction to dune, doi: 10.48550/ARXIV.2002.02967.

Abi, B., et al. (2020b), Long-baseline neutrino oscillation physics potential of the DUNE experiment, *The European Physical Journal C*, *80*(10), doi: 10.1140/epjc/s10052-020-08456-z.

Abratenko, P., et al. (2020), Measurement of space charge effects in the MicroBooNE LArTPC using cosmic muons, *Journal of Instrumentation*, *15*(12), P12,037–P12,037, doi:10.1088/1748-0221/15/12/p12037.

Abud, A. A., et al. (2021), Deep underground neutrino experiment (dune) near detector conceptual design report, doi:10.48550/ARXIV.2103.13910.

Acciarri, R., et al. (2013), A study of electron recombination using highly ionizing particles in the ArgoNeuT liquid argon TPC, *Journal of Instrumentation*, *8*(08), P08,005–P08,005, doi:10.1088/1748-0221/8/08/p08005.

Agostinelli, S., et al. (2003), Geant4—a simulation toolkit, *Nuclear Instruments and Methods in Physics Research Section A: Accelerators, Spectrometers, Detectors and Associated Equipment*, *506*(3), 250–303, doi:https://doi.org/10.1016/S0168-9002(03)01368-8.

Aker, M., et al. (2022), Direct neutrino-mass measurement with sub-electronvolt sensitivity, *Nature Phys.*, *18*(2), 160–166, doi:10.1038/s41567-021-01463-1.

Amoruso, S., et al. (2004), Analysis of the liquid argon purity in the icarus t600 tpc, *Nuclear Instruments and Methods in Physics Research Section A: Accelerators, Spectrometers, Detectors and Associated Equipment*, *516*(1), 68–79, doi: https://doi.org/10.1016/j.nima.2003.07.043.

and D. Q. Adams, et al. (2022), Search for majorana neutrinos exploiting millikelvin cryogenics with CUORE, *Nature*, *604*(7904), 53–58, doi:10.1038/s41586-022-04497-4.

Anton, G., et al. (2019), Search for neutrinoless double-β decay with the complete EXO-200 dataset, *Physical Review Letters*, *123*(16), doi: 10.1103/physrevlett.123.161802.

Araujo, G. (2019), Wavelength shifting and photon detection of scintillation light from liquid argon, Ph.D. thesis, doi:10.13140/RG.2.2.22656.79360.

Bahcall, J. N., and R. Davis (1976), Solar neutrinos: A scientific puzzle, *Science*, *191*(4224), 264–267, doi:10.1126/science.191.4224.264.

Berner, R., et al. (2019), First operation of a resistive shell liquid argon time projection chamber: A new approach to electric-field shaping, *Instruments*, *3*(2), 28, doi:10.3390/instruments3020028.

Cabibbo, N. (1963), Unitary symmetry and leptonic decays, *Phys. Rev. Lett.*, *10*, 531–533, doi:10.1103/PhysRevLett.10.531.

Canetti, L., M. Drewes, T. Frossard, and M. Shaposhnikov (2013), Dark matter, baryogenesis and neutrino oscillations from right-handed neutrinos, *Physical Review D*, *87*(9), doi:10.1103/physrevd.87.093006.

Charles, J., A. Höcker, H. Lacker, S. Laplace, F. R. L. Diberder, J. Malclés, J. Ocariz, M. Pivk, and L. Roos (2005), CP violation and the CKM matrix: assessing the impact of the asymmetric b factories, *The European Physical Journal C*, *41*(1), 1–131, doi:10.1140/epjc/s2005-02169-1.

Chen, H. H., and J. F. Lathrop (1978), Observation of ionization electrons drifting large distances in liquid argon, *Nuclear Instruments and Methods*, *150*(3), 585–588, doi:10.1016/0029-554X(78)90132-5.

Christenson, J. H., J. W. Cronin, V. L. Fitch, and R. Turlay (1964), Evidence for the 2π decay of the k_2^0 meson, *Phys. Rev. Lett.*, *13*, 138–140, doi: 10.1103/PhysRevLett.13.138.

Collaboration, D., et al. (2021), Experiment simulation configurations approximating dune tdr.

Denton, P. B. (2022), Sterile neutrino search with MicroBooNE's electron neutrino disappearance data, *Physical Review Letters*, *129*(6), doi: 10.1103/physrevlett.129.061801.

Dirac, P. A. M., and R. H. Fowler (1928), The quantum theory of the electron, *Proceedings of the Royal Society of London. Series A, Containing Papers of a Mathematical and Physical Character*, *117*(778), 610–624, doi:10.1098/rspa.1928.0023.

Doke, T. (1993), A historical view on the r&d for liquid rare gas detectors, *Nuclear Instruments and Methods in Physics Research Section A: Accelerators, Spectrometers, Detectors and Associated Equipment*, *327*(1), 113–118, doi: https://doi.org/10.1016/0168-9002(93)91423-K.

Duffy, K. E. (2017), First measurements of neutrino and antineutrino oscillation at t2k, Ph.D. thesis, Oxford University.

Dwyer, D., et al. (2018), LArPix: demonstration of low-power 3d pixelated charge readout for liquid argon time projection chambers, *Journal of Instrumentation*, *13*(10), P10,007–P10,007, doi:10.1088/1748-0221/13/10/p10007.

Ereditato, A., et al. (2013), Design and operation of ARGONTUBE: a 5 m long drift liquid argon TPC, *Journal of Instrumentation*, *8*(07), P07,002–P07,002, doi:10.1088/1748-0221/8/07/p07002.

Esteban, I., M. Gonzalez-Garcia, M. Maltoni, T. Schwetz, and A. Zhou (2020), The fate of hints: updated global analysis of three-flavor neutrino oscillations, *Journal of High Energy Physics*, *2020*(9), doi:10.1007/jhep09(2020)178.

Gonzalez-Garcia, M. C., M. Maltoni, and T. Schwetz (2021), NuFIT: Three-flavour global analyses of neutrino oscillation experiments, *Universe*, *7*(12), 459, doi:10.3390/universe7120459.

Hamada, Y., R. Kitano, and W. Yin (2018), Leptogenesis via neutrino oscillation magic, *Journal of High Energy Physics*, *2018*, doi:10.1007/JHEP10(2018)178.

Heindl, T., T. Dandl, M. Hofmann, R. Krücken, L. Oberauer, W. Potzel, J. Wieser, and A. Ulrich (2010), The scintillation of liquid argon, *EPL (Europhysics Letters)*, *91*(6), 62,002, doi:10.1209/0295-5075/91/62002.

Hofmann, M., et al. (2013), Ion-beam excitation of liquid argon, *The European Physical Journal C*, *73*, doi:10.1140/epjc/s10052-013-2618-0.

Kobayashi, M., and T. Maskawa (1973), CP-Violation in the Renormalizable Theory of Weak Interaction, *Progress of Theoretical Physics*, *49*(2), 652–657, doi:10.1143/PTP.49.652.

Li, Y., et al. (2016), Measurement of longitudinal electron diffusion in liquid argon, *Nuclear Instruments and Methods in Physics Research Section A: Accelerators, Spectrometers, Detectors and Associated Equipment*, *816*, 160–170, doi:10.1016/j.nima.2016.01.094.

Maki, Z., M. Nakagawa, and S. Sakata (1962), Remarks on the Unified Model of Elementary Particles, *Progress of Theoretical Physics*, *28*(5), 870–880, doi:10.1143/PTP.28.870.

Mikheyev, S. P., and A. Y. Smirnov (1985), Resonance enhancement of oscillations in matter and solar neutrino spectroscopy, *Yadernaya Fizika*, *42*, 1441–1448.

Ni, K., et al. (2019), Searching for neutrino-less double beta decay of ^{136}xe with PandaX-II liquid xenon detector, *Chinese Physics C*, *43*(11), 113,001, doi:10.1088/1674-1137/43/11/113001.

Ramo, S. (1939), Currents induced by electron motion, *Proceedings of the IRE*, *27*(9), 584–585, doi:10.1109/JRPROC.1939.228757.

Shockley, W. (1938), Currents to conductors induced by a moving point charge, *Journal of Applied Physics*, *9*(10), 635–636, doi:10.1063/1.1710367.

Souza, H. V. (2021), Arapuca, light trapping device for the dune experiment, doi:10.48550/ARXIV.2112.02967.

Tariq, S., et al. (2016), Design of the lbnf beamline target station, doi:10.48550/ARXIV.1612.07293.

Taroni, A. (2015), Nobel prize 2015: Kajita and mcdonald, *Nature Physics*, *11*(11), 891–891, doi:10.1038/nphys3543.

Thomas, J., and D. A. Imel (1987), Recombination of electron-ion pairs in liquid argon and liquid xenon, *Phys. Rev. A*, *36*, 614–616, doi:10.1103/PhysRevA.36.614.

Walkowiak, W. (2000), Drift velocity of free electrons in liquid argon, *Nucl. Instrum. Meth. A*, *449*, 288–294, doi:10.1016/S0168-9002(99)01301-7.

Willis, W., and V. Radeka (1974), Liquid-argon ionization chambers as total-absorption detectors, *Nuclear Instruments and Methods*, *120*(2), 221–236, doi:https://doi.org/10.1016/0029-554X(74)90039-1.

Wright, A. (2013), Nobel prize 2013: Englert and higgs, *Nature Physics*, *9*(11), 692–692, doi:10.1038/nphys2800.

Wu, C. S., E. Ambler, R. W. Hayward, D. D. Hoppes, and R. P. Hudson (1957), Experimental test of parity conservation in beta decay, *Phys. Rev.*, *105*, 1413–1415, doi:10.1103/PhysRev.105.1413.